國立成功大學

太空與電漿科學研究所

碩士論文

Development of Top-Hat Electrostatic Analyzers for Cube Satellites

立方衛星用頂帽型電子探測儀之研發

學生:蔡宜良

指導教授: 張博宇博士

中華民國一百零六年七月十一號

國立成功大學

碩士論文

立方衛星用頂帽型電子探測儀之研發

Development of Top-Hat Electrostatic Analyzers for Cube Satellites

研究生：蔡宜良

本論文業經審查及口試合格特此證明

論文考試委員：陳秋孝 談永頤 張博宇

指導教授：張博宇

系(所)主管：陳炳志

中 華 民 國 106 年 7 月 11 日

摘要

本論文將設計一個可放在小型的衛星(3U 立方衛星 CubeSat)中的頂帽型帶電粒子探測儀 Top-Hat Electrostatic Analyzer (THEA)，來瞭解太空中帶電粒子的分布函數，其中每一個 U 是立方衛星的基本單元，大小為 10x10x10 立方公分。為了能夠更加了解外太空的科學現象，我們必須透過更多的衛星記錄在同一時間不同位置所發生的數據資料，才能夠對在外太空發生的科學現象有更完整、客觀的描述。因為立方衛星的成本較低，所以可以發射多顆搭載頂帽型電子探測儀的立方衛星至外太空，同時於不同地點量測太空當中的帶電粒子的分布函數。頂帽型帶電粒子探測儀是由兩個金屬球殼所構成，若在兩個球殼上施加不同的電壓，當帶電粒子進入時就會受到電場的影響，使其運動方向因受力而偏折，其偏折程度取決於帶電粒子的能量、荷質比、及兩球殼間電壓差，本論文將著重於量測電子的分布函數上。我們將開發模擬程式去計算探測儀內部電場分佈和電子軌跡。透過利用理想的頂帽型電子探測儀，即雙同心的金屬球殼，來估算能夠量測到的最大電子能量。當球殼內外半徑為 44mm、 45mm 且內外球殼的電壓分別為 1kV、 0V，可量測到的電子能量為 22.2 keV。其中，頂帽型帶電粒子探測儀裡的電場，是透過高斯-賽代爾法(Gauss-Seidel method)解拉普拉斯方程式而得，並且為了要節省模擬的時間我們在高斯-賽代爾法中引入了〝旗幟法〞，只針對被選定的區域進行計算；另外，使用 4 階的龍格-庫塔法(Runge-Kutta method)計算相對論效應下電子在頂帽型電子探測儀中的運動軌跡。透過模擬統計，一個內外球殼半徑為 44 mm 和 45 mm，電壓分別為 1kV 和 0V 的頂帽型電子探測儀的幾何因子為 $2.64 * 10^{-4}$(cm^2-sr-keV/keV)。

關鍵字:立方衛星、頂帽型帶電粒子探測儀

ABSTRACT

A top-hat electrostatic analyzer (THEA), well-developed charged particle analyzers for small satellites, will be adopted to cube satellites, which are made out of multiple 10x10x10 cm^3 cubic unit. Data from a single satellite can only be collected at single point at one time. However, to understand any events in the space thoroughly, it is essential to collect data at different locations in the space simultaneously to capture the whole picture. In other words, measurements from multiple satellites are required. Because of the much lower cost of building cube satellites, many cube satellites carrying THEAs can be launched and measure distribution functions of charged particles in different locations in space at the same time. It enables us to have a better understanding of distribution functions of charged particles in the whole space. An zeroth-order approximated using an ideal THEA consisting of two concentric spheres shows that a THEA for measuring electrons with energy up to 22.2 keV can be fit in a cube satellite. Different voltages will be given to two shells so that the trajectories of electrons entering the analyzer will be bent by the corresponding electric fields. Only electrons with the radii of their circular motions that match the average curvature of the shells reach the detector located at the bottom of the analyzer. In this thesis, the electric fields in THEA are calculated by solving the Laplace's equation using Gauss–Seidel method. The Gauss-Seidel method is sped up using 〝Flag technique〞 where only points in THEA are calculated. Trajectories of electrons with relativistic effect will be simulated using 4^{th} order Runge-Kutta method. Results of calculated electric fields and electron trajectories are shown. Simulations show that electron with energy of 21.7 keV can pass through the THEA. The key parameter g-factor which represents the selectivity of the THEA will also be simulated. The g-factor of a THEA where the radius and the potential of the inner and outer sphere are 44 mm, 45 mm, 1kV, and 0V, respectively, equals to 2.64 * 10^{-4}(cm^2-sr-keV/keV).

Key words: Cube satellite, Top-Hat Electrostatic Analyzers

誌謝

本論文是在張博宇教授的指導下完成的，教授淵博的專業知識，嚴謹求真求是的精神，長期在教授的薰陶下，使學生耳濡目染、淺移默化，使我不僅奠定了更扎實的專業技能、研究態度，並營造了一種良好的精神氛圍為；誨人不倦、寬以待人的人格風範對學生影響深遠。雖然我不是您最出色的學生，而您卻是我最尊敬的教授。再來感謝我的實驗室同學，給予我許多寶貴的建議與指導，使論文能順利的完成。

最後，感謝我的家人、朋友，謝謝你們這些年來給予我的支持鼓勵與悉心關懷，使得求學生涯充實、無後顧之憂，才得以順利完成學業。

CONTENTS

LIST OF FIGURES

LIST OF TABLES

CHAPTER 1 INTRODUCTION AND MOTIVATION

Energetic particles from the sun entering the Earth's magnetosphere have great influence on our lives in many ways. They are potentially hazards to space equipments such as communication satellites and global positioning system in consequence of their high energies. Besides, radiations from such charged particles also cause health hazards to aircraft personnel and passengers. Moreover, interactions of energetic electrons with the Earth's ionosphere lead to bright dancing lights in the sky, auroras. Aurora can be in many different colors. Variations in colors are due to the type of gaseous particles that are collided. When electrons strike atoms in Earth’s ionosphere, they excite atoms[1]. When atoms return to their ground state, they release photons in the form of light. The color of light depends on what kind of molecules and atoms are excited depending on the electron energy. For example, when the gaseous particles are composed of nitrogen, they produce blue or red aurora. The most common aurora color is green. It is produced by oxygen molecules. In the other hand, the aurora tells us the global implication of magnetosphere activity and geospace response to solar activity. The precipitating electron energy deposition varies with the electron energy as shown in Fig. 1[2][3].

To understand how plasma waves are excited in the inner magnetosphere, it is important to know the distribution functions of charged particles over the space. To date, there are only few satellites observing events in the radiation belts, such as ERG mission[4] from Japan, the Van Allen Probe and the Time History of Events and Macroscale Interactions during Substorms (THEMIS) mission[5] from United states, etc., to study geomagnetic storms. In several years ago, the prototype of Aurora Electron Spectrometer (AES) was built in Taiwan

to observe the aurora[2]. The AES was designed to detect electron and the energy resolution was from the 10 eV to 20 keV. The AES had 40 ms time resolution for full energy scan with 32 energy steps, and ability to describe where electrons are coming from[2]. However, the size of AES could not fit into the tiny satellite (10cm x 10cm x 10cm). But the AES gives us an inspiration for developing an analyzer. In order to measure the distribution functions for electrons and ions, we have to develop an analyzer for portable spacecraft/satellite. We are designing a Top Hat Electrostatic Analyzer (THEA) that can be fit in a tiny satellite so that more satellites that measure the distribution function at different locations simultaneously can be launched due to their low cost.

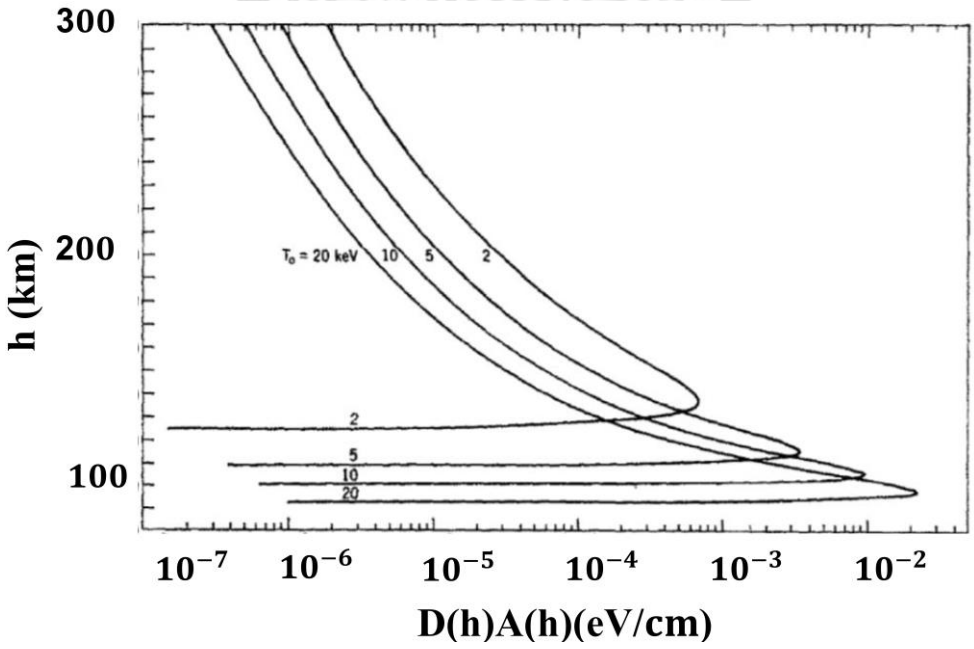

Figure. 1: The relation between of the precipitating and the electron energy[3].

Satellites are expensive to be built and launched. One of the main costs for a space mission is for launching. It costs ～ 256,000 NTD/kg to deliver to geosynchronous transfer

orbit (GTO) using Falcon 9 rocket from SpaceX[6]. By reducing the weight of satellites, i.e., building smaller satellites, the launching expenses can be reduced. Typically, artificial satellites are classified according to its mass as shown in Table. 1.

	Large satellite	Medium-sized satellite	Mini-satellite	Mini-satellite	Nano-satellite or cube satellite
The mass (kg)	≥ 1000	500-1000	100-500	10-100	1-10

Table. 1: The definition of different size of satellites.

Building satellites in a cheap way, i.e., an affordable way, is essential. In 1999, the design of smaller satellite was proposed by a research team in California Polytechnic State University. It was called Cube Satellite (Cubesat)[6][7]. Teams in California Polytechnic State University and Stanford University developed the CubeSat standards to help universities worldwide to study space science and exploration[8]. The concept of cube satellite is the evolution of the traditional satellite.

Data from a single satellite can only be collected at single point at one time. However, to understand physics better, it is essential to collect data at different locations in the space simultaneously to capture the whole picture. To understand space events more thoroughly, more satellites are necessary. The advantage of using cube satellite is that they can be designed and built faster and cheaper. Multiple cube satellites can be launched in the same mission due to its low cost. Therefore, cube satellites are very attractive platform for exploring space science by university-scale researches.

In this thesis, we will focus on measuring the distribution function of electrons. A THEA that can be fit in a cube satellite will be developed. My work is to develop codes to describe the electron motion in THEA. The codes include simulation of electric potentials, electric fields and electron trajectories. In Chapter 2, we will talk about the cube satellite and their subsystems. In Chapter 3, we will give a detailed introduction about THEA and geometric factor. In Chapter 4, we will introduce how to develop and make a careful check of the codes, including the simulation of electric potentials and electron trajectories. In Chapter 5, the simulation of electric potentials and electron trajectories will be performed for an actual THEA design. Geometric factor will be calculated using the simulation results. When electrons pass through the analyzer, each electron will be collected for calculating the geometric factor. In Chapter 6, we will give the conclusion for this thesis. In Chapter 7, we will discuss about the future works.

CHAPTER 2 INTRODUCTION OF CUBESAT

Cube satellites (cubesats) are built in a variety of sizes. The standard size of a cubesat is a 10 cm x 10 cm x 10 cm cube called one unit(1U). Each cube is less than 1.33 kg normally. The size is extendable to larger sizes such as 1.5U, 2U, 3U, 6U, and even 12U. The cost for launching becomes less than couple millions NTD for each satellite, which is less than 0.1 % of the budgets for FORMOSAT-1/2/3/5/7 which all costed more than billions of NTD. Exploring space science using cubesats enables university-scale researches and is a very attractive platform.

Cubesat is a tiny satellite that contains all the essential subsystems like other big satellites. It includes six subsystems: structure system, power supply system, solar panel system, attitude determination and control system, command and data handing system and science payload[9]. The structure system of cubesat is to keep cubesat electronic components together and prevent any potential hazard, also to fortify side panels which hold the solar panels. In common, the structure of cubesat which it is made out of aluminum have to resist the high vibration and temperature. On orbit the power supply system of cubesat will be powered by solar panels that placed on the side of the cubesat. The power supply system harvests, stores and distributes energy. The power supply system has to accommodate a variety of power needs. For the success of the mission, energy collection must be as efficient and as reliable as possible. The solar panels are used to collect energy from the sun. Solar panels cover each side of cubesat and send energy through the main circuit board to be delivered to various components on the satellite. The attitude determination and control system includes sun sensors, magnetometers and gyroscopes in cubesat. The altitude of

cubesat in respect to Earth, Earth's magnetic field and the rotational speed of the cubesat can be obtained. That informations can be used to control the cubesat using the magneto-torquers. The command and data handing system is basically an on-board computer that controls the operation of the cubesat during normal conditions. The data from all subsystems are stored and prepared for transmission by using command and data handling system[10].

Solar panels in the power system providing $\sim$ 2.5 W per cubesat unit [6] are the only energy source. Any other subsystems use energy, occupy space in the satellite and contribute to the total weight. Physical constrains of the science payload including the power consumption, the size and the weight can be estimated. To estimate the availability of space, mass and power consumption for the science payload in a cubesat, informations for each subsystem are listed in Table. 2. The power consumption of the science payload needs to be less than the number of subtracting the total power consumption of all subsystems besides the science payload from the total power provided by solar panels. The volume and the weight of the science payload also need to be less than the number of subtracting the total volume and the total weight of all subsystems besides the science payload from the total size and the acceptable weight of the whole cubesat, respectively. As shown in Table. 2, in order to get feasible space, mass, we will use a 3U cubesat in which available power consumption, the weight, and the size for science payload is ~ 4 W, ~ 1.5 kg, and ~ 10^3 cm^3, respectively. In other words, it occupies and weights a full cubesat unit and used half of the power from the solar panels and all other systems occupy the rest of the volume (2U) and use the other half of the power. Cubesat is a complex system and cooperations between many groups are necessary even it can be built in the university-scale laboratories.

	CubeSat structure	Power supply	Solar panel	Attitude Determination and Control system	Communication system	Command & Data handing	Science payload
1U (Mass<1.33 kg)							
Mass(g)	135.8	204.9	60	233	72.5	71.3	777.5(g)
Power (mW)		68.3	2500	610	4200	337.5	-2715.8 (mW)
Volume(cm^3)	10^3	$1.46*10^2$		$3.80*10^2$	$1.29*10^2$	$9.67*10^1$	248.3
2U (Mass<2.66 kg)							
Mass(g)	279.3	204.9	60	233	72.5	71.3	920.7(g)
Power (mW)		68.3	4800	610	4200	337.5	-415.8 (mW)
Volume(cm^3)	$2*10^3$	$1.46*10^2$		$3.80*10^2$	$1.29*10^2$	$9.67*10^1$	$1.24*10^3$ (cm^3)
3U (Mass<4.0 kg)							
Mass(g)	408.3	204.9	60	233	72.5	71.3	**$1.04*10^3$(g)**
Power (mW)		68.3	9200	610	4200	337.5	**$3.98*10^3$ (mW)**
Volume(cm^3)	$3*10^3$	$1.46*10^2$		$3.80*10^2$	$1.29*10^2$	$9.67*10^1$	**$2.25*10^3$ (cm^3)**

Table. 2: The limited conditions correspond to the 1U, 2U, 3U cubesat[11][12].

CHAPTER 3 INTRODUCTION OF TOP HAT ELECTROSTATIC ANALYZERS

(THEA)

A THEA consists of two shells and two parallel plates as the collimator on the top as shown in Fig. 2[13]. The opening at the top of the shells allows charged particles to enter the analyzer. Different voltages are given to two shells so that trajectories of charged particles entering the analyzer are bent by the corresponding electric fields. Only particles with the particular energies corresponding to the given voltages can go through the shells. Therefore, the distribution functions of electrons can be measured by counting the number of charged particles arriving the detector as a function of the supplied voltages.

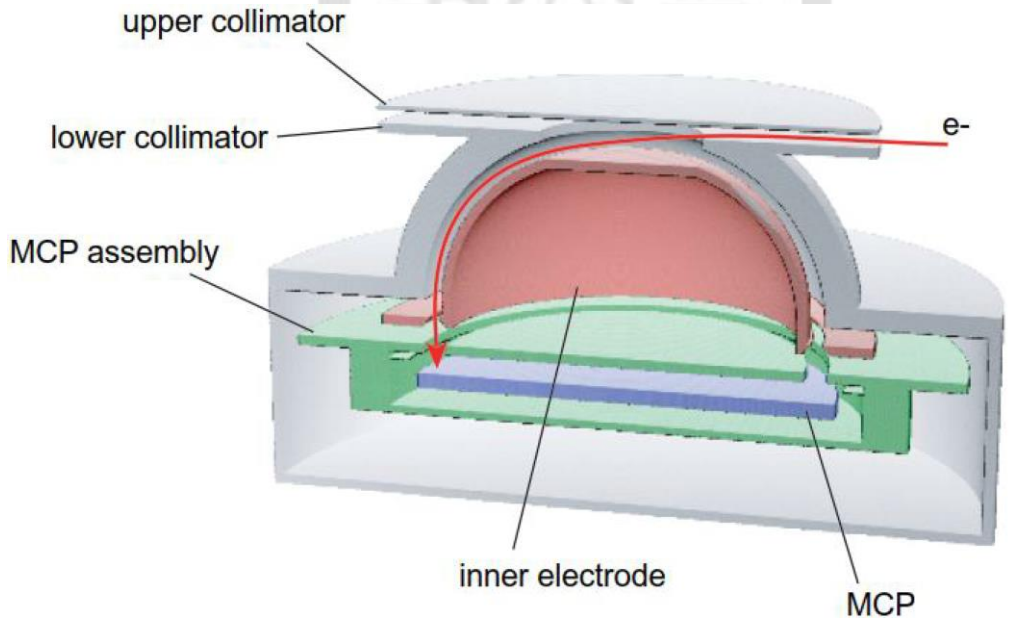

Figure. 2: Cross section of a THEA. The red line represents the trajectory of an electrons in the shells, while the blue and green regions represent the micro-channel plates (MCPs) and the MCP assembly[13].

3.1 Zeroth order estimation

Our goal is to fit a THEA into a cubesat. In other words, the THEA needs to be smaller than 10^3 cm^3. To estimate the feasibility, we would like to use zeroth order estimation. An ideal THEA consisting of two concentric metal spheres shown in Fig. 3 were used.

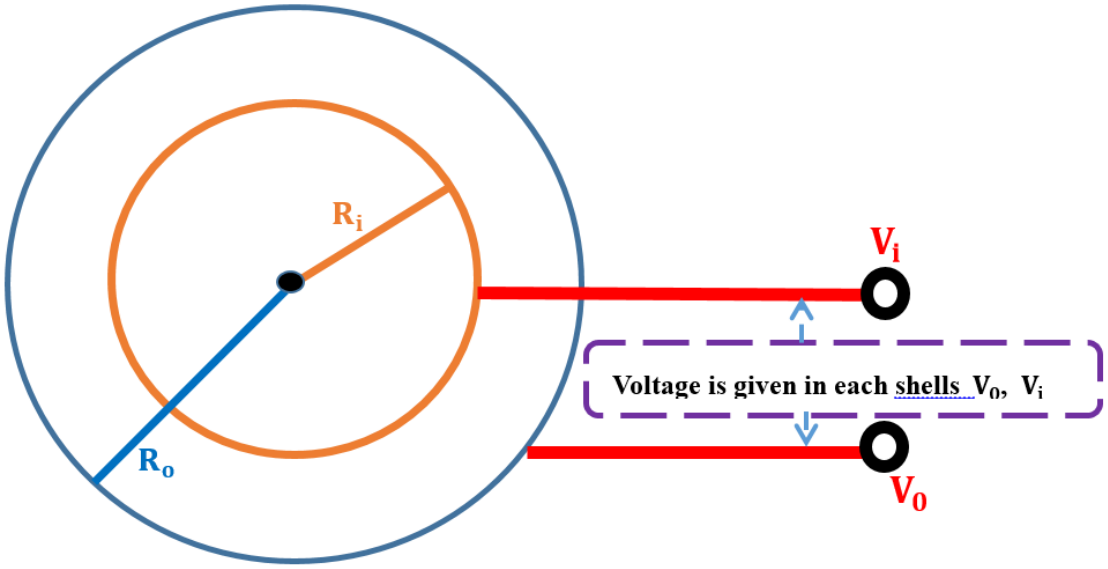

Figure. 3: Two concentric metallic spherical shells where R_i, R_0, V_i, V_o are the radii and electric potentials of the inner and the outer sphere of concentric metal spheres, respectively.

According to Gauss' law, the electric field between two concentric metal spheres in the ideal spherical THEA is shown below.

$$\oint_s \vec{E} \cdot d\vec{S} = \frac{Q}{\epsilon_0}. \quad (1)$$

Therefore, the electric field is

$$\vec{E} = \frac{Q}{4\pi\epsilon_0 r^2}\hat{r} \tag{2}$$

where Q is the total charge in the spherical gauss surface and r is the distance to the center of the sphere. The charge distribution is uniform on each conducting sphere in the ideal THEA due to the symmetry. Therefore, the electric field and thus the electric potential only depend on r. The potential is set to zero at $r = \infty$. Thus,

(1) For $r > R_0$, the electric potential

$$V(r) = -\int_{\infty}^{r} \vec{E}\cdot d\vec{r} = -\int_{\infty}^{r} \frac{Q_{r>R_0}}{4\pi\epsilon_0 r^2}\hat{r}\cdot(-\hat{r})dr = \int_{\infty}^{r} \frac{Q}{4\pi\epsilon_0 r^2}dr = \frac{Q_{r>R_0}}{4\pi\epsilon_0 r}\ . \tag{3}$$

(2) For $R_0 > r > R_i$, the electric potential

$$\begin{aligned} V(r) &= -\int_{R_0}^{r} \vec{E}\cdot(-\hat{r})dr + V(R_0) \\ &= \frac{Q_{R_0>r>R_i}}{4\pi\epsilon_0}\int_{R_0}^{r}\frac{1}{r^2}dr + V(R_0) \\ &= \frac{Q_{R_0>r>R_i}}{4\pi\epsilon_0}\left(\frac{1}{R_0}-\frac{1}{r}\right) + \frac{Q_{r>R_0}}{4\pi\epsilon_0 R_0}. \end{aligned} \tag{4}$$

With the boundary conditions $V(R_0) = V_0$ and $V(R_i) = V_i$, the potential between R_0 and R_i is

$$V(r) = \frac{R_0R_i}{R_0-R_i}\cdot(V_i - V_0)\cdot\left(\frac{1}{r}-\frac{1}{R_0}\right) + V_0 \quad \text{for} \quad R_0 > r > R_i. \tag{5}$$

Taking the negative of the gradient of Eq. 5 yields

$$\vec{E}(r) = -\nabla V = \frac{R_0R_i}{R_0-R_i}\cdot(V_i - V_0)\cdot\frac{1}{r^2}\hat{r}. \tag{6}$$

Let's consider an electron passing through the center of the gap between two concentric metal spheres, i.e., the radius of circular motions of electrons equals to $(R_i + R_o)/2$, and reaching the detector located at the bottom of the upper hemisphere as shown in Fig. 4. The centripetal force must equal to the electric force:

$$m_e \frac{v^2}{r} = |q\vec{E}| = q\frac{R_0 R_i (V_i - V_0)}{(R_0 - R_i)(R_0 + R_i) r^2}. \quad (7)$$

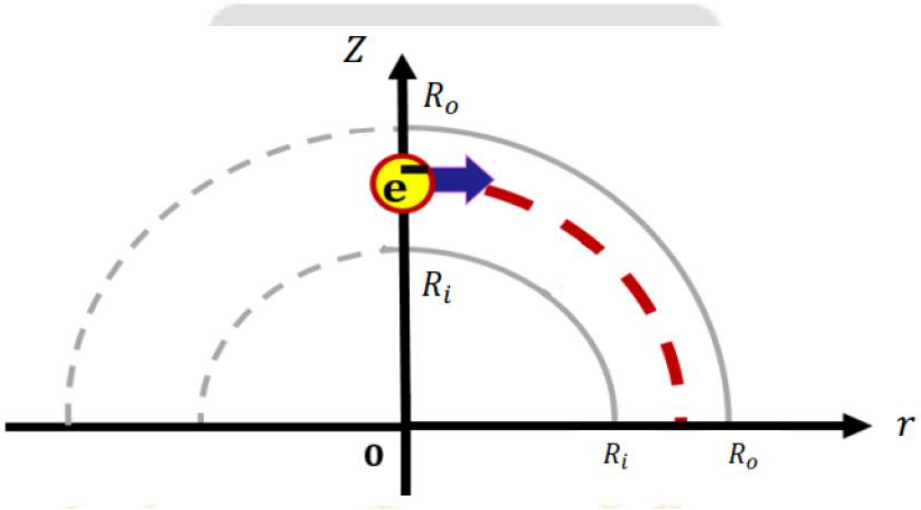

Figure. 4: Two concentric metallic spherical shell where R_0 and R_i are the outer radius and inner radius.

The relation between kinetic energy of electrons E_K to the voltage between two spheres and the radii of two spheres is

$$\frac{E_K}{q} = \frac{\frac{1}{2}mv^2}{q} = -\frac{(V_i - V_o)R_0 R_i}{{R_o}^2 - {R_i}^2}, \quad (8)$$

which can be treated as a selection rule of the analyzer under zeroth order approximation. Equation 8 shows that a THEA for cubesat with $R_i = 44\ \text{mm}, R_0 = 45\ \text{mm}, V_i = 1\ \text{kV}$ and $V_0 = 0\ \text{V}$ measuring the electron distribution function up to 22.2 keV is possible. Notice that Eq. 8 is just an estimation. More sophisticated simulations given in chapter 4 for a real THEA are needed for designing a THEA. Nevertheless, the model of zeroth order approximation can be used to benchmark the simulations code that we developed.

3.2 Geometric factor

Geometric factor (g-factor) is the selectivity of an analyzer. G-factor represents the ratio of the number of electrons which enter THEA to the number of electrons which are detected at the bottom of THEA. G-factor is determined via simulations. For those electrons passing through the bottom of the detector, the initial positions, initial energies and incidence of angles are recorded. As shown in Fig. 5[13], particle counts on the detector in a period of time can be expressed as

$$C = -\int T(K, \Omega, \vec{x}) \left(\vec{J}(K, \Omega, \vec{x}) \cdot d\vec{S}\right) dS d\Omega dt \tag{9}$$

where K, Ω, $\vec{x}$, $\vec{S}$ are kinetic energy, the effective view in solid angle, locations of particle entering the analyzer, and the aperture, respectively. $\vec{J}$ is the differential flux of particles that enter the analyzer. The function

$$T(K, \Omega, \vec{x}) = \begin{cases} 1 & \text{if detected} \\ 0 & \text{if not detected} \end{cases} \tag{10}$$

represents the selection rule of the particle reaching the detector. An "energy geometric factor" $G_E(cm^2\text{-sr-keV})$ defined as

$$G_E \equiv \int T(K, \Omega, \vec{x})(\hat{j} \cdot \hat{n}) dS \, d\Omega dK \tag{11}$$

depends on the analyzer's geometric and the energy of the particle entering the analyzer. In order to get a characteristic selectivity independent of energy, a mean energy $\langle k \rangle$ defines as

$$\langle k \rangle \equiv \frac{\int KT(K, \Omega, \vec{x})(\hat{j} \cdot \hat{n}) dS \, d\Omega dK}{\int T(K, \Omega, \vec{x})(\hat{j} \cdot \hat{n}) dS \, d\Omega dK} \tag{12}$$

is introduced. As a result, an energy-independent sensitivity, g-factor, is defined as

$$G \equiv \frac{G_E}{\langle k \rangle}. \tag{13}$$

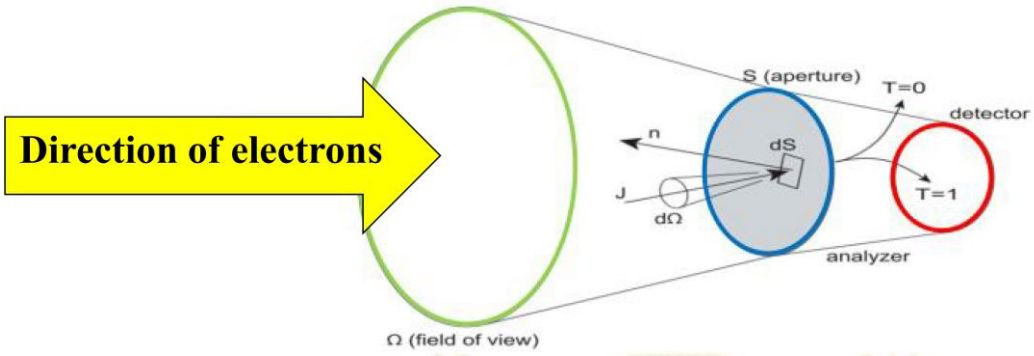

Figure. 5: Illustration of g-factor integration. A g-factor is determined by the number of particles that can pass through on the bottom of detector[13].

Electrons with different energy can enter the analyzer from different locations with different angles in simulations. The Eq. 11, Eq. 12 and Eq. 13 are determined by the number and the energy of electrons that can pass through the analyzer. The g-factor will be calculated in section 5.3.

CHAPTER 4 DEVELOPMENT OF THE SIMULATION CODE

The simulation code is divided into three parts: (1) calculating electric field via solving Laplace's equation in cylindrical coordinate using Gauss Seidel method[14]; (2) calculating trajectories of electrons using 4^{th}- order Runge-Kutta method; (3) calculating the selectivity of the analyzer, i.e., geometric factor. Details of the code is given in this chapter. The numerical methods that are used will be introduced first in 4.1. In section 4.2, the Laplace's equation solver for calculating electric potential in the THEA is given. In section 4.3, the electron trajectories in the THEA calculated using 4^{th} order Runge-Kutta method is describes. All the developed codes were benchmarked by comparing the results from the simulation to the analytical solution of an ideal THEA introduced in chapter 3.

4.1 Introduction of numerical methods

In this part, Finite Difference method, Gauss Seidel method, bilinear interpolation method and Runge-Kutta method will be introduced[14][15][16][17].

4.1.1 Finite Difference method

Finite Difference method is to write a derivative equation into differential form. A set of grid points in the region of interest (ROI) are first defined. Take two-dimensional space in Cartesian coordinate system (x,y) shown in Fig. 6 as an example, step sizes $\Delta x \equiv \frac{x_{max}-x_{min}}{N_x}$ and $\Delta y \equiv \frac{y_{max}-y_{min}}{N_y}$ where $x_{min} \leq x \leq x_{max}$ and $y_{min} \leq y \leq y_{max}$ are the ROI. N_x and N_y are the number of grids in x and y direction, respectively. If $(x_{min}, y_{min}) \equiv (0,0)$, x_i and y_j are $x_i = i * \Delta x$, i =0,…,N_x, and $y_j = j * \Delta y$, j =0,…, N_y. x_{-1}, y_{-1}, $x_{N_{x+1}}$ and $y_{N_{y+1}}$ are used for applying boundary conditions.

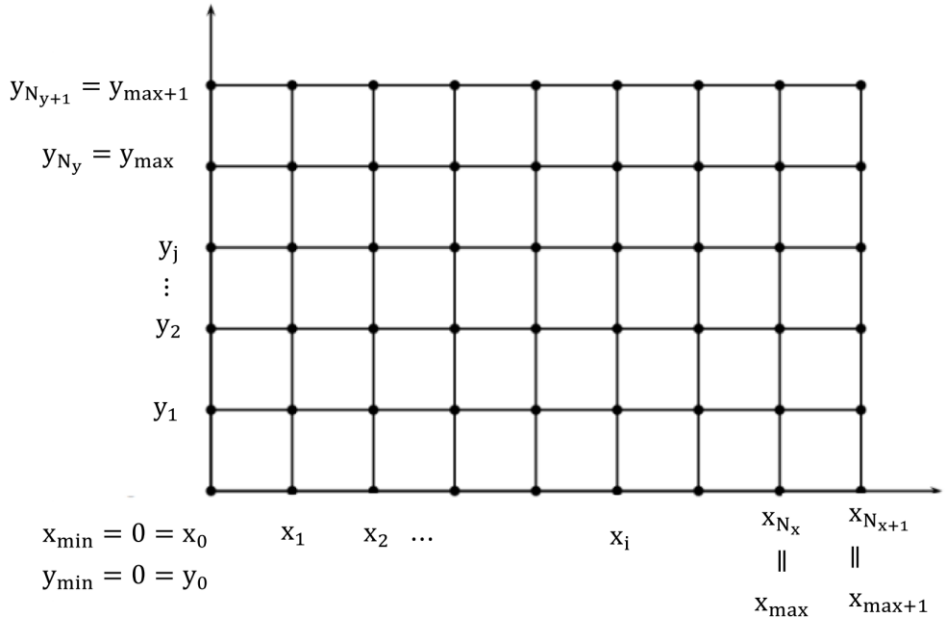

Figure. 6: The diagram of gird points in Cartesian coordinate.

A differential equation can be obtained by using the Taylor expansions of the function

in the derivative form. For example, Laplace's equation in 2D Cartesian coordinate is

$$\frac{\partial^2 V(x,y)}{\partial x^2} + \frac{\partial^2 V(x,y)}{\partial y^2} = 0 \,. \tag{14}$$

The Taylor expansion of V(x,y) at point (x,y) in x direction is

$$V(x+\Delta x, y) = V(x,y) + \frac{\frac{\partial V(x,y)}{\partial x}}{1!}\Delta x + \frac{\frac{\partial^2 V(x,y)}{\partial x^2}}{2!}\Delta x^2 + \cdots + \frac{\frac{\partial^n V(x,y)}{\partial x^n}}{n!}\Delta x^n + \cdots \quad , \tag{15a}$$

$$V(x-\Delta x, y) = V(x,y) - \frac{\frac{\partial V(x,y)}{\partial x}}{1!}\Delta x + \frac{\frac{\partial^2 V(x,y)}{\partial x^2}}{2!}\Delta x^2 - \cdots - \frac{\frac{\partial^n V(x,y)}{\partial x^n}}{n!}\Delta x^n + \cdots \quad . \tag{15b}$$

Three methods of differential equations using Eq. 15 are commonly considered: forward, backward, and central differences for 1^{st} order derivative. They are:

Forward differential equation: $\frac{\partial V(x,y)}{\partial x} \equiv \frac{V(x+\Delta x,y)-V(x,y)}{\Delta x} + O(\Delta x)$ (from Eq. 15a) ,

Backward differential equation: $\frac{\partial V(x,y)}{\partial x} \equiv \frac{V(x,y)-V(x-\Delta x,y)}{\Delta x} + O(\Delta x)$ (from Eq. 15b) ,

Central differential equation: $\frac{\partial V(x,y)}{\partial x} \equiv \frac{V(x+\Delta x,y)-V(x-\Delta x,y)}{2*\Delta x} + O(\Delta x^2)$ (From Eq. 15a & 15b).

With smaller Δx, the differential equation becomes closer to derivative equation. The physical meaning of forward, backward, and central differences are shown in Fig. 7 [18]. The distance is divided into several parts and the distance of each part is Δr. Δr is called a step size. In Fig. 7, the derivative at the red point will be estimated by using forward or backward or central differences. The forward difference uses the value at (r+Δr,z) and (r,z) and their step size. The backward difference uses the value at (r-Δr,z) and (r,z) and their step size. The central difference uses the value at (r+Δr,z) and (r-Δr,z) and their step size.

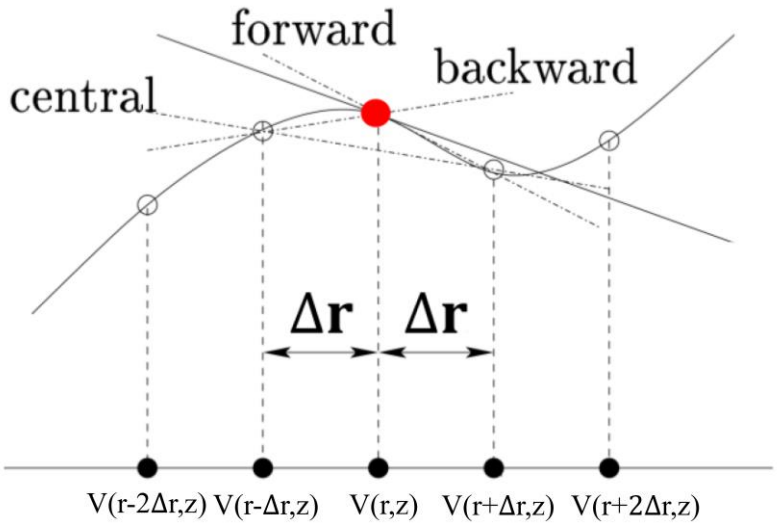

Figure. 7: The physical meaning of forward, backward, and central differences[18].

In Laplace's equation, central differential will be used for discretizing 2^{nd} order derivative in the equation. Equation 16 and Eq. 17 represent the discretization of $\frac{\partial^2 V(x,y)}{\partial x^2}$ and $\frac{\partial^2 V(x,y)}{\partial y^2}$, respectively.

$$\frac{\partial^2 V(x,y)}{\partial x^2} = \frac{V(x+\Delta x,y) + V(x-\Delta x,y) - 2V(x,y)}{(\Delta x)^2}, \tag{16}$$

$$\frac{\partial^2 V(x,y)}{\partial y^2} = \frac{V(x,y+\Delta y) + V(x,y-\Delta y) - 2V(x,y)}{(\Delta y)^2}. \tag{17}$$

The derivation using the central difference is given as following.

$$V(x+\Delta x,y) \approx V(x,y) + \frac{\frac{\partial V(x,y)}{\partial x}}{1!}\Delta x + \frac{\frac{\partial^2 V(x,y)}{\partial x^2}}{2!}\Delta x^2$$

$$\approx V(x,y) + \frac{\frac{V(x+\Delta x,y)-V(x-\Delta x,y)}{2*\Delta x}}{1!}\Delta x + \frac{\frac{\partial^2 V(x,y)}{\partial x^2}}{2!}\Delta x^2$$

$$\Longrightarrow V(x+\Delta x,y)-V(x,y)\approx\frac{V(x+\Delta x,y)-V(x-\Delta x,y)}{2}+\frac{\frac{\partial^2V(x,y)}{\partial x^2}}{2!}\Delta x^2$$

$$\Longrightarrow 2V(x+\Delta x,y)-2V(x,y)-V(x+\Delta x,y)+V(x-\Delta x,y)\approx\frac{\partial^2V(x,y)}{\partial x^2}\Delta x^2$$

$$\Longrightarrow V(x+\Delta x,y)-2V(x,y)+V(x-\Delta x,y)\approx\frac{\partial^2V(x,y)}{\partial x^2}\Delta x^2$$

$$\Longrightarrow\frac{\partial^2V(x,y)}{\partial x^2}\equiv\frac{V(x+\Delta x,y)-2V(x,y)+V(x-\Delta x,y)}{\Delta x^2}.$$

The derivation process of $\frac{\partial^2V(x,y)}{\partial y^2}$ in Eq. 17 is similar to the derivation process for $\frac{\partial^2V(x,y)}{\partial x^2}$.

Therefore, the Laplace's equation in the differential form is

$$\frac{V(x+\Delta x,y)+V(x-\Delta x,y)-2V(x,y)}{(\Delta x)^2}+\frac{V(x,y+\Delta y)+V(x,y-\Delta y)-2V(x,y)}{(\Delta y)^2}=0. \quad (18)$$

If Δx equals Δy in Eq. 18, Laplace's equation in the differential form becomes

$$V(x+\Delta x,y)+V(x-\Delta x,y)+V(x,y+\Delta y)+V(x,y-\Delta y)-4V(x,y)=0. \quad (19)$$

In this thesis, Laplace's equation is solved in cylindrical coordinate. Since the geometry of THEA and thus the potential in the analyzer is azimuthal symmetric, i.e., $\frac{\partial^2V}{\partial\varphi^2}=0$,

$$\frac{\partial^2V}{\partial r^2}+\frac{1}{r}\frac{\partial V}{\partial r}+\frac{\partial^2V}{\partial z^2}=\mathbf{0}. \quad (20)$$

In Eq. 20, the mesh in the cylindrical coordinate is similar to the one in Fig. 6, but with different variables. Variables "x" and "y" are replaced by "r" and "z" for $\hat{r}$ direction and $\hat{z}$ direction, respectively. The grid points in cylindrical coordinate system (r,z) are shown in Fig. 8, where step sizes $dr\equiv\frac{r_{max}-r_{min}}{N_r}$, $dz\equiv\frac{z_{max}-z_{min}}{N_z}$. $r_{min}\le r\le r_{max}$ and $z_{min}\le z\le z_{max}$ are the ROI. N_r and N_z are the number of grids in r and z directions, respectively. $r_i=i*dr$, i =0,…,N_r , and $z_j=j*dz$, j =0,…, N_z. dr and dz are the grid

sizes in r and z direction and they are constants. The differential form of Eq. 20 is

$$V_{i,j} = \frac{h}{8r_i}\left(V_{i+1,j} - V_{i-1,j}\right) + \frac{1}{4}\left[V_{i-1,j} + V_{i+1,j} + V_{i,j-1} + V_{i,j+1}\right] \tag{21a}$$

where i and j are indexes of grids in r and z directions, respectively.

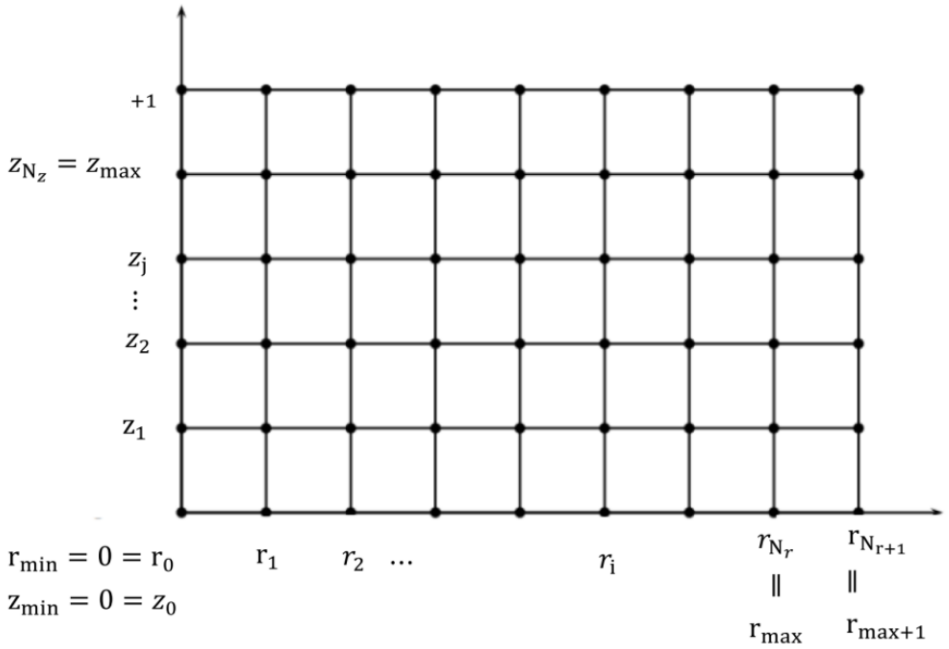

Figure. 8: The diagram of gird points in cylindrical coordinate.

In Eq. 21a, the boundary condition is reflective boundary condition if i does not equal to zero. If i equals to zero, the boundary condition will be considered differently. The finite difference form in Laplace's equation on the z axis is defined as:

$$V_{i,j} = \frac{\frac{dr^2}{4}\left[V_{0,j+1} + V_{0,j-1}\right] + dz^2 \cdot V_{1,j}}{\frac{dr^2}{2} + dz^2}, \qquad i = 0 \tag{21b}$$

The derivation of Eq. 21a and Eq. 21b are shown in appendix A and appendix B. The discretized Laplace's equation is solved using Gauss Seidel method introduced in section

4.1.2.

4.1.1.1 Boundary conditions

In our simulation, when i equals zero, the boundary conditions of that region are divided into three parts representing the Gauss's law in Eq. 1 . The top region, the bottom region and the side region are given Fig. B-1 in appendix B. On the top of the cylinder, the electric field is a constant with $\frac{\partial V}{\partial r} = 0$. At the bottom of the cylinder, the electric field is also a constant. On the side of the cylinder, the electric field is a constant. Following the derivation given in appendix B, the boundary condition at i=0, i.e., is

$$V(0,j) = \frac{(dr_2)^2[dz_1 V(0,j+1) + dz_2 V(0,j-1)] + 2dz_1 dz_2 (dz_1 + dz_2)V(1,j)}{dz_1 (dr_2)^2 + dz_2 (dr_2)^2 + 2dz_1 dz_2 (dz_1 + dz_2)}.$$

At the region of $r = r_{max}$ and $z = z_{max}$, the reflective boundary condition is used. When z = 0, we also use the reflective boundary.

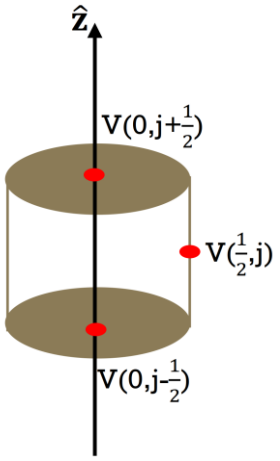

Figure. B-1: The boundary conditions are divided into three parts representing the Gauss's law.

4.1.2 Gauss Seidel method

Gauss Seidel method is used to solve a system of equations, i.e., a matrix solver. Let the system of equations be[14]

$$a_{11}x_1 + a_{12}x_2 + a_{12}x_3 + \cdots + a_{1n}x_n = c_1$$

$$a_{21}x_1 + a_{22}x_2 + a_{32}x_3 + \cdots + a_{2n}x_n = c_2$$

$$\vdots$$

$$a_{n1}x_1 + a_{n2}x_2 + a_{n2}x_3 + \cdots + a_{nn}x_n = c_n\,.$$

If the diagonal elements of the system of equations written in a matrix form are not zero, i.e., $a_{ii} \neq 0$, the Gauss Seidel method can be used to solve the system of equations. The procedure is shown in Fig. 9.

With an initial gauss ($x_1{}^0$, $x_2{}^0$, $\cdots$, $x_n{}^0$), the first $x_1{}^1$, $x_2{}^1$, $\cdots$, $x_n{}^1$ can be updated sequentially using the following equations where the super script represent the numbers of iterations.

$$x_1{}^{\mathbf{1}} = (c_1 - a_{12}x_2{}^0 - a_{13}x_3{}^0 \ldots . - a_{1n}x_n{}^0) \,/\, a_{11}$$

$$x_2{}^1 = (c_2 - a_{21}x_1{}^{\mathbf{1}} - a_{23}x_3{}^0 \ldots . - a_{2n}x_n{}^0) \,/\, a_{22},$$

$$\vdots$$

$$x_n{}^{\mathbf{1}} = (c_n - a_{n1}x_1{}^{\mathbf{1}} - a_{n2}x_2{}^{\mathbf{1}} \ldots . - a_{n,n-1}x_{n-1}{}^{\mathbf{1}}) \,/\, a_{nn}\,. \qquad (22)$$

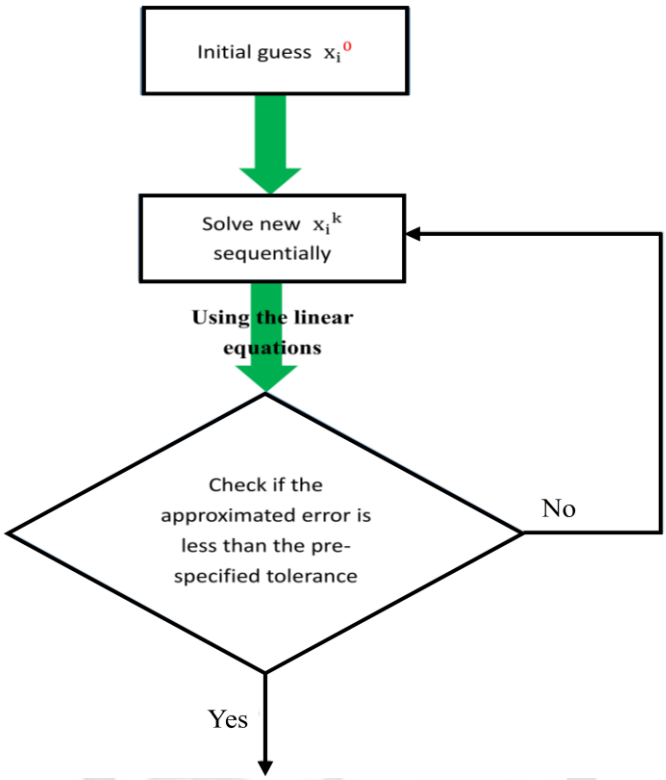

Figure. 9: The procedure of the Gauss Seidel method.

Eq. 22 can be rewritten in a summation form:

$$x_i^{k+1} = \frac{1}{a_{ii}}\left(c_i - \sum_{j=1}^{j=i-1} a_{ij}x_j^{k+1} - \sum_{j=i+1}^{n} a_{ij}x_j^{k}\right), i = 1,2,\dots,n \tag{23}$$

where k represents the k^{th} time of iterations. Once you have determined x_1 from the first equation, its value is then used in the second equation to obtain the new x_2. Similarly, the new $x_1, x_2, \dots, x_{i-1}$ are used to obtain the new x_i. From an initial guess of $x_i^{(0)}$, new sets of x_i are calculated iteratively using Eq. 22. At the end of each iteration, there are two ways to stop the iteration.

(i) the approximated error for each x_i is

$$|\text{approximation error}| = \text{Max}\left[\left|\frac{\text{the recently obtained value of } x_i - \text{the previous value of } x_i}{\text{the recently obtained value of } x_i + 10^{-10}}\right| * 100\%\right].$$

Notice that 10^{-10} is added to the denominator to prevent it for being zero. In general, when the absolute value of relative approximated error for each x_i is less than the pre-specified tolerance, the iterations stops[13].

(ii) Alternative way is terminate the simulation, is to insert the solution into the left hand side of Eq. 20 .

We used the second way to terminate the iteration. The iterations will be stopped if the number is smaller than 10^{-7}.

4.1.3 Gauss Seidel method accelerated by using Flag method

Flag method is to identify which points in ROI are important and we only calculate the solutions of those points to improve the efficiency of simulation for calculating electric potentials. Shown in Fig. 10 , if r is smaller than R_i or bigger than R_o, electric potentials are constant and do not change during iterations. We only care about the electric potential between R_i and R_o. Therefore, we mark and calculate only those points in that area. If the area between R_i and R_o is much less than the whole area, the program will be speeded up

and save a lot of time for calculating electric potential.

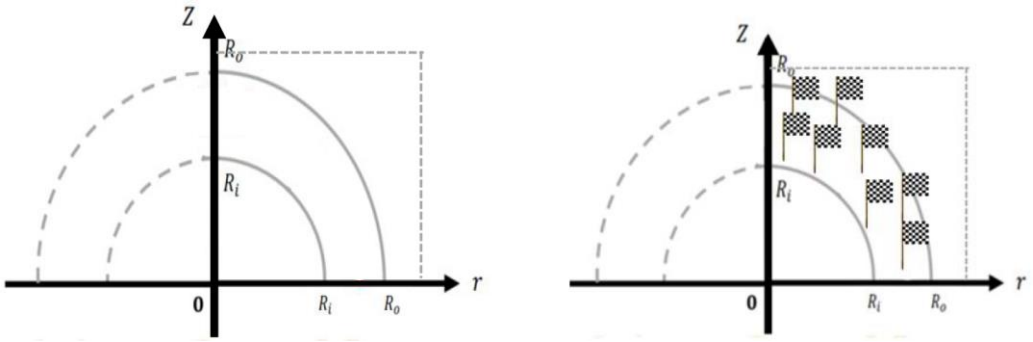

Figure. 10: Flag method is used to identify the region to be calculated.

One of the main improvements is that instead of loop over all i and j, we use another array that stores only the "flagged" grid, and loop over that array in each iteration. So in each iteration, the number of loop reduces from imax*jmax to only number of points between the outer and the inner spheres.

4.1.4 Bilinear interpolation method

Bilinear interpolation method is to estimate a number not on the mesh or grid from the known numbers on mesh points. For example, electric potential is calculated using Gauss Seidel method at each grid point. Electric field is then calculated by taking the negative of gradient of the electric potential. Therefore, the electric fields are known on grid points. If we want to know the electric field not on grid points, the bilinear interpolation can be used to determine the electric field.

Bilinear interpolation method is thrice of linear interpolation method. As shown in Fig. 11, it is to estimate the value $f(x_0, y_0)$, which is not on a grid point, from the given values f(x, y), f(x+Δx, y), f(x, y+Δy) and f(x+Δx, y+Δy) located on the grids. In the initial phase, the f(x, y), f(x+Δx, y), f(x, y+Δy) and f(x+Δx, y+Δy) are used to estimate the unknown values $f(x_1, y_1)$ and $f(x_2, y_2)$ or $f(x_3, y_3)$ and $f(x_4, y_4)$ via linear interpolation. Next, $f(x_1, y_1)$ and $f(x_2, y_2)$ or $f(x_3, y_3)$ and $f(x_4, y_4)$ are used to estimate the value of $f(x_0, y_0)$. The process for bilinear interpolation method is shown in the following.

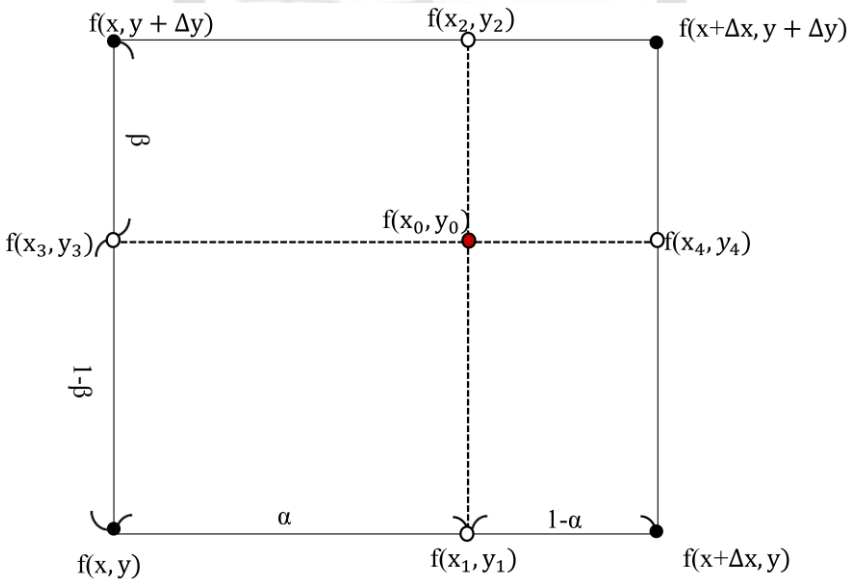

Figure. 11: The example of linear (bilinear) interpolation method. The distance of each side is one. The α is the portion between x and x_1 and the β is the portion between x_3 and x.

The unknown values $f(x_1, y_1)$, $f(x_2, y_2)$, $f(x_3, y_3)$ and $f(x_4, y_4)$ are obtained using linear interpolation method in the initial phase:

$$f(x_1, y_1) = \alpha * f(x+\Delta x, y) + (1-\alpha) * f(x, y) \ ,$$

$$f(x_2, y_2) = \alpha * f(x+\Delta x, y+\Delta y) + (1-\alpha) * f(x, y+\Delta y) \ ;$$

$$f(x_3, y_3) = \beta * f(x, y) + (1-\beta) * f(x, y+\Delta y) \ ,$$

$$f(x_4, y_4) = \beta * f(x+\Delta x, y) + (1-\beta) * f(x+\Delta x, y+\Delta y) \ ,$$

where $\alpha \equiv x_1 - x = x_2 - x$ and $\beta \equiv (y+\Delta y) - y_3 = (y+\Delta y) - y_4$.

Finally,

$$f(x_0, y_0) = \beta * f(x_1, y_1) + (1-\beta) * f(x_2, y_2)$$

$$f(x_0, y_0) = \beta * [f(x+\Delta x, y) + (1-\alpha) * f(x, y)] + (1-\beta) * [\alpha * f(x+\Delta x, y+\Delta y) + (1-\alpha) * f(x, y+\Delta y)]$$

or $f(x_0, y_0) = (1- \alpha) * f(x_3, y_3) + \alpha * f(x_4, y_4) f(x_0, y_0$

$$= \beta * [\beta * f(x, y) + (1-\beta) * f(x, y+\Delta y)] + (1-\beta) * [\beta * f(x+\Delta x, y) + (1-\beta) * f(x+\Delta x, y+\Delta y)].$$

The bilinear interpolation method is used to determine the electric field if we want to know the electric field not on grid points.

4.1.5 Runge-Kutta method

Runge-Kutta method is a numerical technique for solving 1^{st}-order ordinary differential equation (ODE), e.g., the equations of motion of charged particles in electric fields. The 1^{st}-order and 4^{th}-order Runge-Kutta method will be introduced.

The 1^{st}-order Runge-Kutta method was originally proposed by Euler and was called Euler's method. It is used to solve a 1^{st}-order ODE within a given interval of the independent variable x with a given initial condition. The general form of 1^{st}-order ODE is

$$\frac{dy}{dx} = f(x, y) \tag{24}$$

where function f is known. The interval is chopped into small subdivisions of length h. Therefore, the independent variable x can discretized as x_n where the index n range from 0 to nmax.

The Euler's method is to obtain the unknown point (x_{n+1},y_{n+1}) from the known point (x_n,y_n). As shown in Fig. 12 , (x_{n+1},y_{n+1}) can be calculated using (x_n,y_n) and the tangential line through this known point[13]. From Eq. 24, the slope of the tangential line is $f(x_n,y_n)$. Therefore,

$$x_{n+1} = x_n + h \,, \tag{25}$$

$$y_{n+1} = y_n + \Delta y + O(h^2) \text{ where } \Delta y = h * f(x_n,y_n) \,.$$

The last term $O(h^2)$ represents the truncation error of the Euler method, which is a secondary order accuracy in h. For a given initial condition, i.e. (x_0,y_0) is known, (x_1,y_1), (x_2,y_2), ⋯, (x_n,y_n), ⋯, (x_{nmax},y_{nmax}) can be calculated sequentially using Eq. 25 .

In Fig. 12, there is an error between the real solution (orange line) and numerical solution (red line) depending on h and the order of the Runge-Kutta method. If higher order

Runge-Kutta method is used, the error will be smaller and the calculated solution will be closer to the real solution.

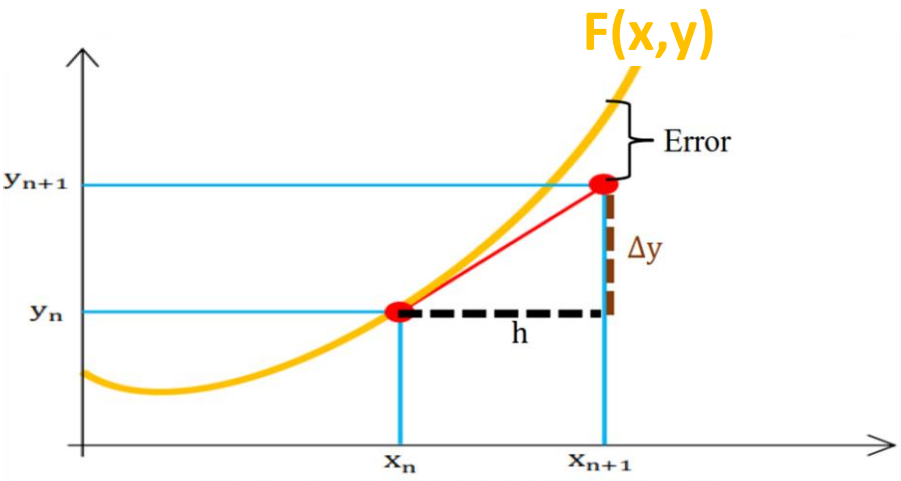

Figure. 12: The orange line is represented differential equation of F(x,y)=0 and the red line is represented the numerical method (Euler's method).

Similar to the 1^{st}-order Runge-Kutta method, 4^{th}-order Runge-Kutta method uses the derivative of y from the known point (x_n,y_n) to calculate the solution of the following unknown point (x_{n+1},y_{n+1})[13]. The difference is how to estimate the derivative of y. For the 4^{th}-order Runge-Kutta method,

$$y_{n+1} = y_n + \frac{(k_1 + 2k_2 + 2k_3 + k_4)}{6}h + O(h^5) \qquad (26)$$

where $O(h^5)$ is the local truncation error of 4^{th}-order Runge-Kutta method[15]. The derivative of y is estimated using k_1, k_2, k_3, k_4 written as following and shown in Fig. 13 .

$$k_1 = f(x_i, y_i)$$

$$k_2 = f\left(x_i + \frac{1}{2}h, y_i + \frac{1}{2}k_1 h\right)$$

$$k_3 = f\left(x_i + \frac{1}{2}h, y_i + \frac{1}{2}k_2 h\right)$$

$$k_4 = f(x_i + h, y_i + k_3 h)\ .$$

For brief speaking, k_1, k_2, k_3, and k_4 are different slopes in the interval[15]. k_1 is the slope at the beginning of the time step. k_2 is an estimation of the slope at the midpoint which is estimated using the slope k_1 to step halfway forward. k_3 is another estimation of the slope at the midpoint using the slope k_2 to step halfway forward. At last, k_4 is the estimation of the slope at the endpoint using slope k_3 to step all the way across h[16]. The derivation of Runge-Kutta method is given on the appendix C.

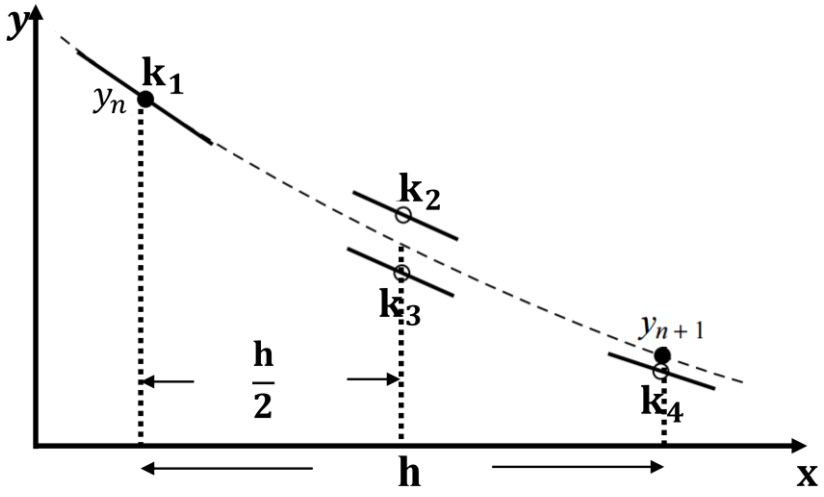

Figure. 13: The 4^{th}-order Runge Kutta method. In each step, the derivative is evaluated four times: once at the initial point, twice at midpoint, and once at the endpoint[15].

Similar to the 1^{st}-order Runge-Kutta method, (x_n, y_n) can be calculated sequentially from a

given initial condition. Trajectories of electrons will be solved using the 4^{th}-order Runge-Kutta method.

4.2 Laplace's equation solver for an ideal THEA

To get a precise electric field, solving Laplace's equation

$$\nabla^2 V = 0 \tag{27}$$

with given geometry and applied voltage are necessary. Since the THEA and thus the potential in the analyzer is azimuthal symmetric, Laplace's equation is solved in cylindrical coordinates, i.e,

$$\frac{\partial^2 V}{\partial r^2} + \frac{1}{r}\frac{\partial V}{\partial r} + \frac{\partial^2 V}{\partial z^2} = 0\,. \tag{28}$$

The original equation from Eq. 28 written in the finite differential form is

$$V_{i,j} = \begin{cases} \frac{h}{8r}\left(V_{i+1,j} - V_{i-1,j}\right) + \frac{1}{4}\left[V_{i-1,j} + V_{i+1,j} + V_{i,j-1} + V_{i,j+1}\right], & i \neq 0 \\ \dfrac{\frac{dr^2}{4}\left[V_{0,j+1} + V_{0,j-1}\right] + dz^2 \cdot V_{1,j}}{\frac{dr^2}{2} + dz^2}, & i = 0 \end{cases} \tag{29}$$

where i and j are indexes of grids in r and z directions, respectively, and $V_{0,j}$ are numbers on z axes. $r_i = i * dr$, i =0,…,N_r , and $z_j = j * dz$, j =0,…, N_z. dr and dz are the grid sizes in r and z direction and they are constants. Notice that $\frac{\partial V}{\partial r} \equiv 0$ so that there is no singularity on z axis. The boundary conditions are described in section 4.1.1 and in appendix A.

In Fig. 14 and Fig. 15, if the distance between the grid points and outer radius or between the grid points and inner radius is less than the distance of the grid size, Eq. 29 should be modified. This can be considered in two different points of view: (i) in numerical point of view and (ii) in physical point of view. In numerical point of view, we want to estimate the unknown point by using finite difference method. The finite difference method was introduced in section 4.1.1. The 5 closest mesh points were used to calculate the unknown point. If the distance between special point and unknown point is smaller than the distance between the 5 closest mesh points and unknown point, the numerical result is not accurate to describe the electric potentials in the THEA. In physical point of view, the concentric spheres are made of metal. Charges will be accumulated on the surface of the sphere. The charge can effect upon the distribution of electric potential on the surface of the sphere. Therefore, we must consider the special points near the sphere. It is divided into two parts for discussion shown in Fig. 14 and Fig. 15 and they are called special points: (1) the distance between the grid point and inner radius is less than the distance of the grid size; (2) the distance between the grid point and outer radius is less than the distance of the grid size. The green points (r_e, z_e) in Fig. 14 and Fig. 15 represent the intersections of the grids and the inner sphere or the grids and the outer sphere. In Fig. 14, this is an example of the distance between the grid to the inner sphere being less than the grid size. In this example, we have

to replace dr with dr_2. Similarly, a new gap dz_2 is used as shown in Fig. 14. dr_2 and dz_2 are defined as

$$dr_2 \equiv r_i - \left(\sqrt{((R_i)^2 - (z_i)^2}\right) \text{ and}$$

$$dz_2 \equiv z_i - \left(\sqrt{((R_i)^2 - (r_i)^2}\right) . \quad (30)$$

(a)

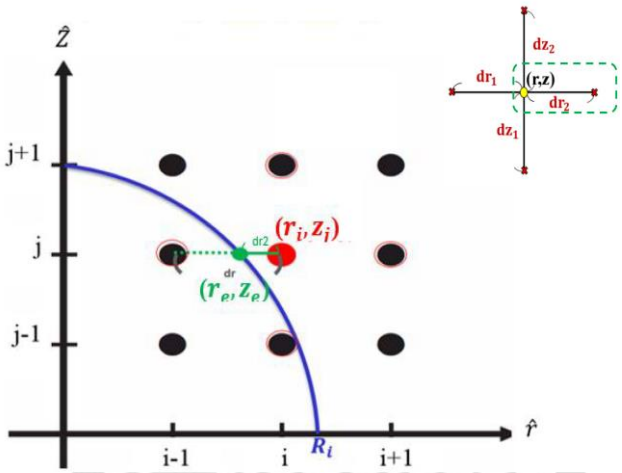

(b)

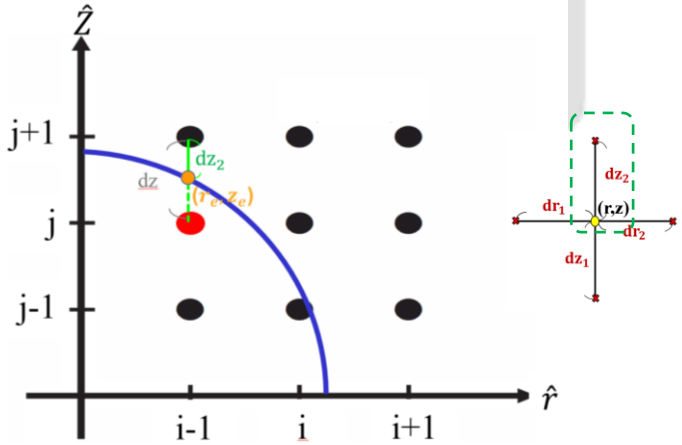

Figure. 14: Definition of the special points near the inner radius. Blue curve represent the inner radius.

Similarly, dr_1 and dz_1 for grids next to the outer sphere are

$$dr_1 \equiv \left(\sqrt{(R_o)^2 - (z_i)^2}\right) - r_i \text{ and}$$

$$dz_1 \equiv \left(\sqrt{(R_o)^2 - (r_i)^2}\right) - z_i \ . \tag{31}$$

(a)

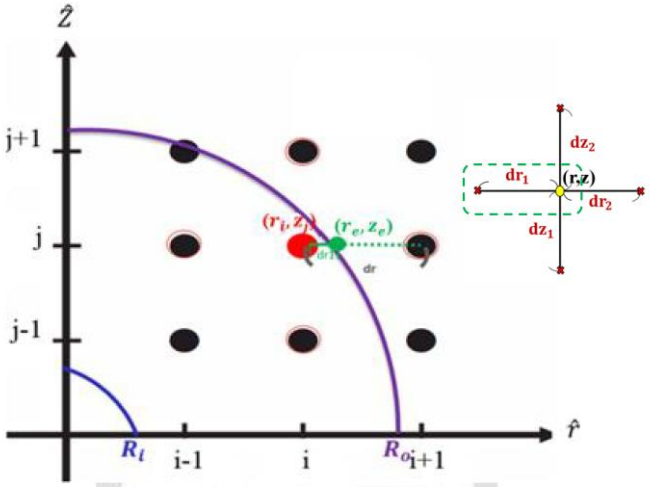

(b)

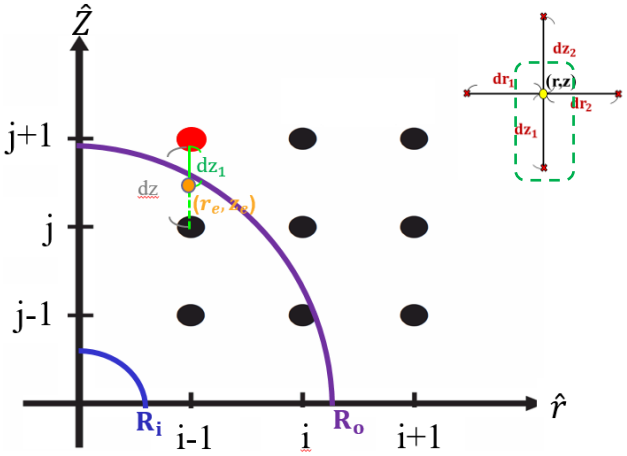

Figure. 15: Definition of the special points near the outer radius. Blue curve and purple curve represent the inner radius and outer radius.

To simplify our code, we don't assume that dr and dz are constants. As shown in Fig. 16, the

grid sizes around each grid point are defined as dr_1, dr_2, dz_1, dz_2.

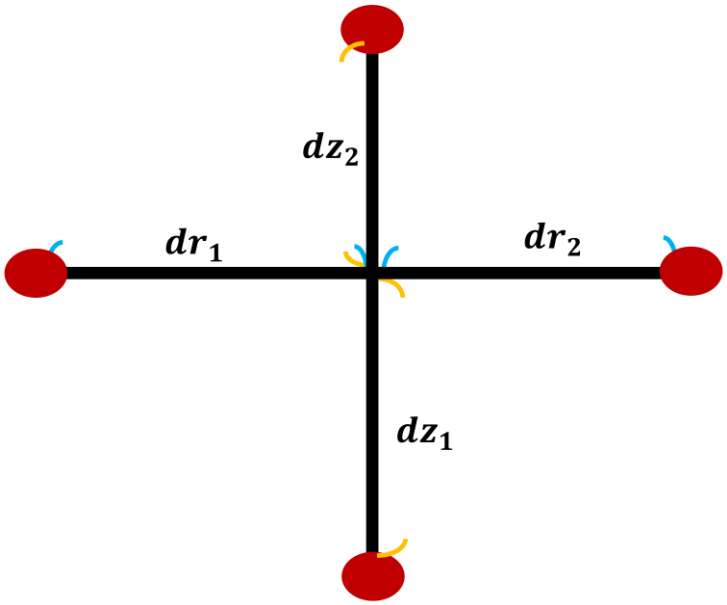

Figure. 16: dr_1, dr_2, dz_1 and dz_2 are defined around each grid point.

Therefore, Laplace's equation in cylindrical coordinate is modified to Eq. 32 and solved using Gauss-Seidel method. The derivation of Eq. 32 is shown in appendix A. For those points away from the sphere, not special points, dr_1 and dr_2 equal to dr while dz_1 and dz_2 equal to dz and Eq. 32 become identical to Eq. 29. Otherwise, Eq. 30 or Eq. 31 are used.

$$V(i,j)=\begin{cases}\left[\dfrac{4}{dr_1^{\,2}+dr_2^{\,2}}+\dfrac{4}{dz_1^{\,2}+dz_2^{\,2}}\right]^{-1} \\ *\left\{\begin{array}{l}\dfrac{2}{dr_1^{\,2}+dr_2^{\,2}}\left[V_{i+1,j}+V_{i-1,j}-(dr_2-dr_1)\dfrac{V_{i+1,j}-V_{i-1,j}}{dr_2+dr_1}\right] \\ +\dfrac{2}{dz_1^{\,2}+dz_2^{\,2}}\left[V_{i,j+1}+V_{i,j-1}-(dz_2-dz_1)\dfrac{V_{i,j+1}-V_{i,j-1}}{dz_2+dz_1}\right] \\ +\dfrac{V_{i+1,j}-V_{i-1,j}}{r(dr_2+dr_1)}\end{array}\right\}, \quad i\neq 0 \\ \left[(dr_2)^3(dz_1+dz_2)+2dr_2(dz_1+dz_2)dz_1dz_2\right]^{-1} \\ \left[(dr_2)^3(dz_1V_{0,j+1}+dz_2V_{0,j-1})+2dr_2(dz_1+dz_2)dz_1dz_2V_{1,j}\right], \quad i=0.\end{cases} \tag{32}$$

4.2.1 Benchmarking the Laplace's equation solver

In order to check if the code calculates the electric potential correctly, we first use it to calculate the ideal THEA introduced in chapter 3. By comparing the result from our simulation to the result from Eq. 5, we can benchmark our code. The case we calculated was an ideal THEA consisting two concentric metal sphere with R_i=2 cm, R_o=9 cm. V_i=6 V, and V_o=2 V. In Fig. 17, it is the calculated electric potential in the ideal THEA. The left panel of Fig. 17 is the distribution of electric potential in the ideal THEA calculated using analytical solution. The right panel of Fig. 17 is the distribution of electric potential in the ideal THEA from the numerical result. In Fig. 18, the direct comparison between the simulation result and the analytic calculation is shown. The red dashed line represents the

analytic result, and the green solid line represents the simulation result of all the points between R_i and R_o. Two lines on top of each other shows that our Laplace's equation solver is correct.

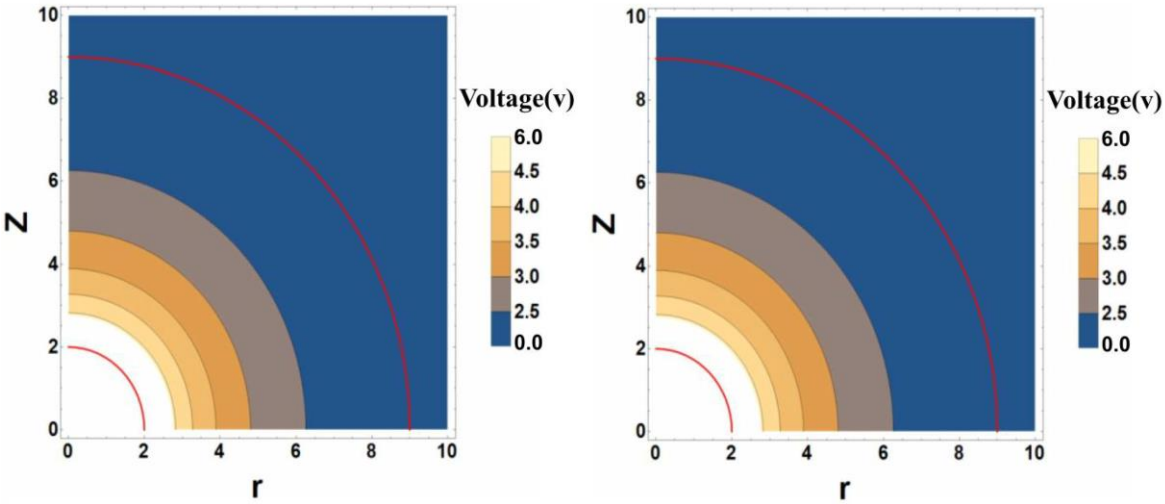

Figure. 17: The distribution of electric potential in ideal THEA with the radii and potentials of the inner and the outer of 2 cm, 9 cm, 6 V, 2 V, respectively. The smaller quarter circle represents inner radius. The larger quarter circle in red represents outer radius. The right hand side is from simulation result. The left hand side is from the analytic solution.

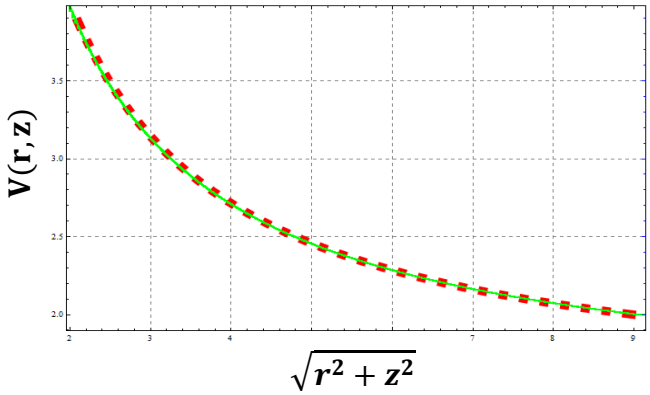

Figure. 18: The simulation result of electric potentials is compared with the analytic result in two concentric metal spheres where the radii and potentials of the inner and the outer are 2 cm, 9 cm, 6 V, 2 V, respectively.

4.3 Trajectories of electrons in ideal THEA

Trajectories of electrons in THEA are calculated using the 4^{th}-order Runge-Kutta method. Both the cases with and without Relativistic are considered. The electric field are calculated using either the analytical solution or the simulation result from Laplace's equation solver. By comparing the results, the code for calculating the trajectories and the bilinear interpolation of electric fields are benchmarked.

4.3.1 The electron trajectories without Relativistic

The equations of motion for electrons in the THEA without considering Relativistic are:

$$\frac{d}{dt}\vec{x} = \vec{v} \equiv \vec{f}(t, \vec{x}, \vec{v}), \qquad (33)$$

$$m_e \frac{d}{dt}\vec{v} = q\vec{E}(\vec{x}) \equiv \vec{g}(t, \vec{x}, \vec{v}),$$

where $\vec{x}$, $\vec{v}$, q = 1.6x10^{-19} coulomb and m_e = 9.1x10^{-31} kg are the position, velocity, charge and mass of electrons, respectively, and $\vec{E}$ is the electric field. Electrons trajectories are calculated from Eq. 33 using 4^{th}-order Runge-Kutta method. The simulation result of electron trajectories in two concentric metal spheres are shown in Fig. 19 to benchmark the simulation code. In each time step, the 4^{th}-order Runge-Kutta method is calculated using the equation given in Table. 3.

$\overrightarrow{k_1} = \Delta t\vec{f}(t_0, \overrightarrow{x_0}) = \Delta t\overrightarrow{V_0}$	$\overrightarrow{L_1} = \Delta t\vec{g}(t_0, \overrightarrow{x_0}) = \Delta tq\vec{E}(\overrightarrow{x_0})$
$\overrightarrow{k_2} = \Delta t\vec{f}\left(t_0 + \frac{\Delta t}{2}, \overrightarrow{x_0} + \frac{\overrightarrow{k_1}}{2}, \overrightarrow{V_0} + \frac{\overrightarrow{L_1}}{2}\right)$ $= \Delta t\overrightarrow{V^{(1)}};$ $\overrightarrow{V^{(1)}} = \overrightarrow{V_0} + \frac{q\vec{E}(\overrightarrow{x_0})\Delta t}{2} = \overrightarrow{V_0} + \overrightarrow{L_1}/2$	$\overrightarrow{L_2} = \Delta t\vec{g}\left(t_0 + \frac{\Delta t}{2}, \overrightarrow{x_0} + \frac{\overrightarrow{k_1}}{2}, \overrightarrow{V_0} + \frac{\overrightarrow{L_1}}{2}\right)$ $= \Delta tq\vec{E}(\overrightarrow{x^{(1)}});$ $\overrightarrow{x^{(1)}} = \overrightarrow{x_0} + \overrightarrow{V_0}\frac{\Delta t}{2}$ $= \overrightarrow{x_0} + \overrightarrow{k_2}/2$
$\overrightarrow{k_3} = \Delta t\vec{f}\left(t_0 + \frac{\Delta t}{2}, \overrightarrow{x_0} + \frac{\overrightarrow{k_2}}{2}, \overrightarrow{V_0} + \frac{\overrightarrow{L_2}}{2}\right)$ $= \Delta t\overrightarrow{V^{(2)}};$ $\overrightarrow{V^{(2)}} = \overrightarrow{V_0} + \frac{q\vec{E}(\overrightarrow{x^{(1)}})\Delta t}{2} = \overrightarrow{V_0} + \overrightarrow{L_2}/2$	$\overrightarrow{L_3} = \Delta t\vec{g}\left(t_0 + \frac{\Delta t}{2}, \overrightarrow{x_0} + \frac{\overrightarrow{k_2}}{2}, \overrightarrow{V_0} + \frac{\overrightarrow{L_2}}{2}\right)$ $= \Delta tq\vec{E}(\overrightarrow{x^{(2)}});$ $\overrightarrow{x^{(2)}} = \overrightarrow{x_0} + \overrightarrow{V^{(1)}}\frac{\Delta t}{2}$ $= \overrightarrow{x_0} + \overrightarrow{k_2}/2$
$\overrightarrow{k_4} = \Delta t\vec{f}\left(t_0 + \frac{\Delta t}{2}, \overrightarrow{x_0} + \overrightarrow{k_3}, \overrightarrow{V_0} + \overrightarrow{L_3}\right)$ $= \Delta t\overrightarrow{V^{(3)}};$ $\overrightarrow{V^{(3)}} = \overrightarrow{V_0} + q\vec{E}(\overrightarrow{x^{(2)}})\Delta t = \overrightarrow{V_0} + \overrightarrow{L_3}$	$\overrightarrow{L_4} = \Delta t\vec{g}\left(t_0 + \frac{\Delta t}{2}, \overrightarrow{x_0} + \overrightarrow{k_3}, \overrightarrow{V_0} + \overrightarrow{L_3}\right)$ $= \Delta tq\vec{E}(\overrightarrow{x^{(3)}});$ $\overrightarrow{x^{(3)}} = \overrightarrow{x_0} + \overrightarrow{V^{(2)}}\Delta t$ $= \overrightarrow{x_0} + \overrightarrow{k_3}$

Table. 3: The 4^{th} order Runge-Kutta for solving Eq. 33.

The electric field in the Table. 3 is calculated using Eq. 6, the analytic solution. The initial position of the electron is (r,z)=(0 cm , 5 , 5 cm). In section 3.1, the maximum energy of electron is ~ 21 keV by using the zeroth order estimation. We assumption that the electron

motion is only in $\hat{r}$ direction. The initial velocity in $\hat{r}$ direction is 573423 (m/s) and the initial velocity in $\hat{z}$ direction is 0 (m/s). We use these initial conditions to benchmark the codes. The step size has great effect upon simulation of the electron trajectories. The trajectory of electron must be less than the step size in a time step if the simulation of the electron trajectories will get the precise result. In our simulation, r_{Max} and z_{Max} represent the boundary of interest, and the time step is 10^{-10} sec. In this chapter, the distance of r_{Max} is 10 cm in $\hat{r}$ direction and z_{Max} is 10 cm in $\hat{z}$ direction. The boundary of interest is divided into 1000 in each direction and the grid size is $10 * 10^{-2}/1000$ m. In each time step, the electron moves ~ $5.7 * 10^{-5}$ m which is much smaller than the grid size, i.e., 10^{-4} m. The simulation result of electron trajectories are shown in Fig. 19. The dashed line in Fig. 19 represents the numerical calculation using Mathematica. The green solid line in Fig. 19 represents the simulation result. Those two lines are on top of each other shows that the code for simulating electron trajectories is correct.

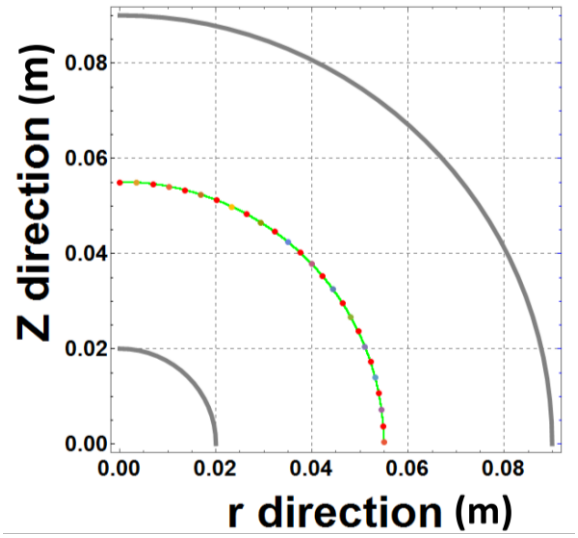

Figure. 19: The simulation result of electron trajectories in two concentric metal spheres where the radii and potentials of the inner and the outer are 2 cm, 9 cm, 6 V, 2 V, respectively. Solid green line is from simulation result which the electric field is from Eq.6. Colorful Points are from numerical calculation using Mathematica.

4.3.1.1 Benchmarking the bilinear interpolation of simulated electron fields

In previous section, the electric fields were calculated using the analytical model. However, there will be no analytical model in a real THEA and it needs to be calculated from the Laplace's equation solver. The electric field on each grid can be calculated by taking negative of the gradient of the electric potential. The differential form of electric field is in Eq. 34.

$$E_r(i,j) = -\frac{V(i+1,j)-V(i-1,j)}{2dr}, \qquad (34)$$

$$E_z(i,j) = -\frac{V(i,j+1)-V(i,j-1)}{2dz}.$$

If the point is not on the grid, we will use bilinear method to calculate the electric field. The simulation result of electron trajectories in two concentric metal spheres are shown in Fig. 20 . In Fig. 20, the initial position of the electron is (r,z)=(0 cm , 5 , 5 cm). The initial velocity in $\hat{r}$ direction is 573423 (m/s) and the initial velocity in $\hat{z}$ direction is 0 (m/s). In Fig. 20 , the red dashed line represents the numerical calculation using Mathematica. In Fig. 20, the purple solid line represents the simulation result. The only differences between Fig. 19 and Fig. 20 is how the electric fields were calculated. Those two lines on top of each others indicates that the bilinear interpolations of the simulated electric fields are correct.

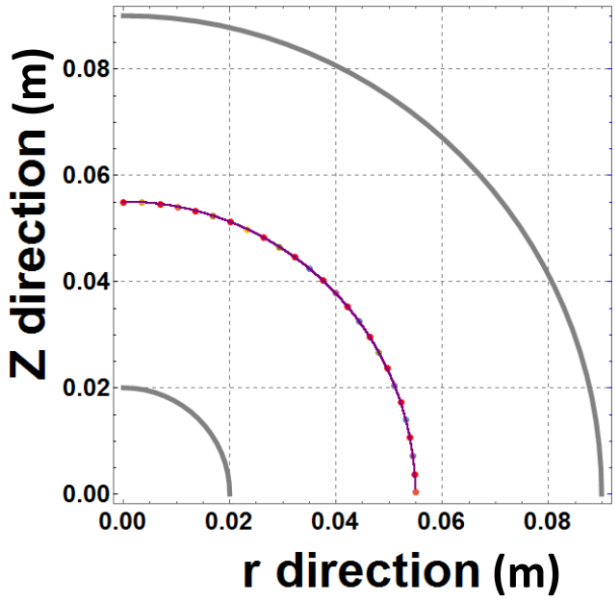

Figure. 20 The simulation result of electron trajectories is compared with the analytic result in two concentric metal spheres where the radii and potentials of the inner and the outer are 2cm, 9cm, 6V, 2V, respectively. Solid purple line is from simulation result which the electric field is from bilinear interpolation method. Colorful Points are from analytic result.

4.3.2 The electron trajectories with relativistic effect

When the kinetic energy of electrons is high enough, the relativistic effect needs to be considered. The velocity of electrons calculated using a given kinetic energy with and without relativistic effect are:

$$V = \sqrt{\frac{2E}{m}} \text{ with non} - \text{relativistic}$$

$$V = \frac{c\sqrt{E(E + 2mc^2)}}{E + mc^2} \text{with relativistic}$$

where E, m and c are represent the electron kinetic energy(J), rest mass and speed of light. The difference between the velocity with and without relativistic are shown in Fig. 21. According to Fig. 21, relativistic effect causes at least 3% difference in velocity when the kinetic energy is above 20 keV. In other words, relativistic effect have to be considered. If the electron kinetic energy is even higher and higher, the difference between non-relativistic and relativistic effect will be obvious. In Fig. 22, the brown dashed line represents the non-relativistic effect. In Fig. 22, the blue solid line represents the relativistic effect.

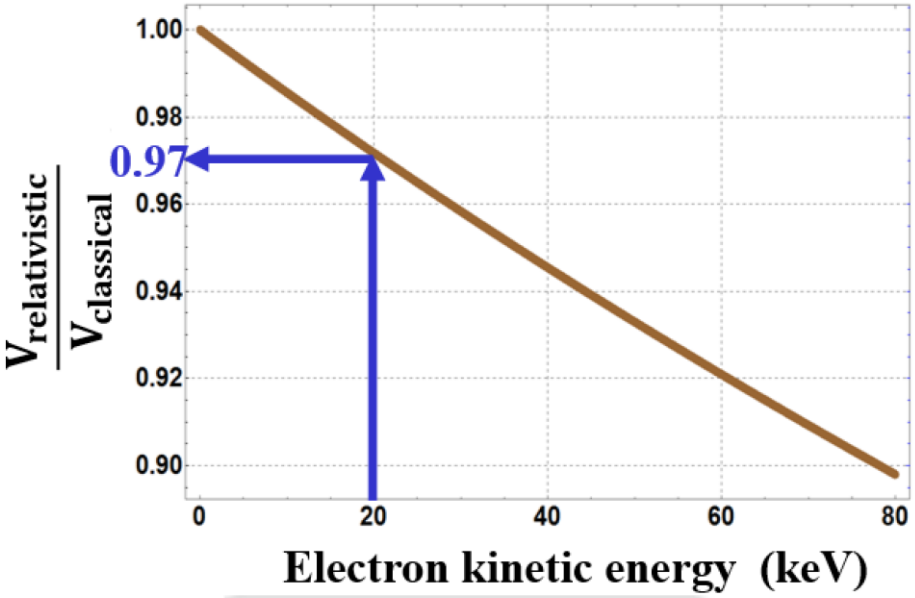

Figure. 21: The relationship for the speed of electron between relativistic effect and classical.

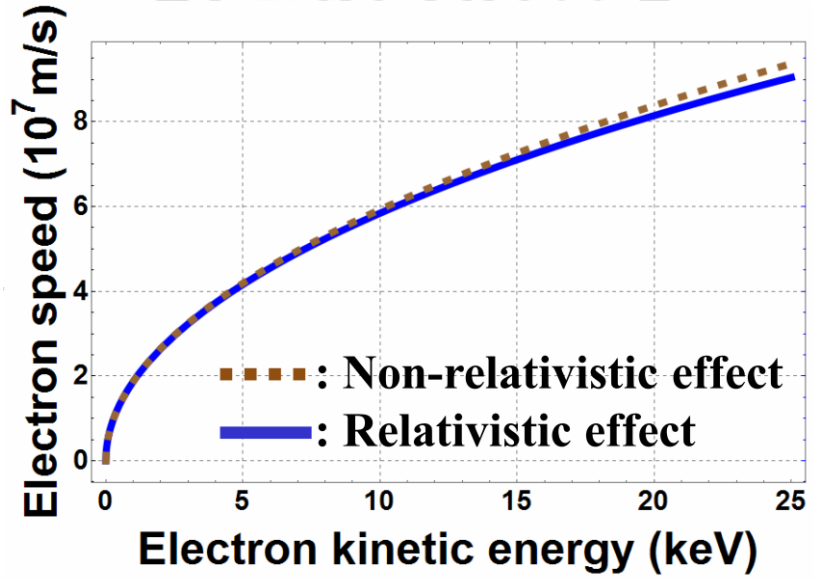

Figure. 22: If the electron kinetic energy is higher and higher, the difference of electron motion with relativistic and without relativistic will be obvious.

The equations of motion with relativistic effect for electrons in the analyzer is:

$$\frac{d\vec{X}(t)}{dt} = \frac{c \cdot \vec{P}(t)}{\sqrt{{m_0}^2 \cdot c^2 + P(t)^2}}$$
$$\frac{d\vec{P}(t)}{dt} = q \cdot \vec{E}(\vec{X}(t)) \quad (35)$$

where $\vec{X}$, $\vec{P}$, q = $1.6\text{x}10^{-19}$ coulomb and m_e = $9.1\text{x}10^{-31}$ kg are the position, velocity, charge and mass of electrons, respectively, and $\vec{E}$ is the electric field. The velocity is calculated from the relativistic momentum shown as following:

$$\vec{P} = \frac{m\vec{v}}{\sqrt{1 - \frac{v^2}{c^2}}} = \sqrt{{P_r}^2 + {P_z}^2},$$
$$\Longrightarrow P^2 = {P_r}^2 + {P_z}^2 = \frac{m^2({v_r}^2 + {v_z}^2)}{1 - \frac{v^2}{c^2}} = \frac{m^2 v^2}{1 - \frac{v^2}{c^2}}$$
$$\Longrightarrow P^2 - \frac{P^2 v^2}{c^2} = m^2 v^2$$
$$\Longrightarrow P^2 = (m^2 c^2 + P^2)\frac{v^2}{c^2}$$
$$\Longrightarrow \vec{v} = \frac{c\vec{P}}{\sqrt{m^2 c^2 + P^2}} = \frac{d\vec{X}(t)}{dt}$$

where m, c, v_r, v_z, P_r and P_z are the rest electron mass, speed of light, speed of electron in $\hat{r}$ direction, speed of electron in $\hat{z}$ direction, the momentum in $\hat{r}$ direction and the momentum in $\hat{z}$ direction, respectively.

Also, the time step is considered in our simulation. We have to consider two situations: (1) the speed of electron is much less than light speed; (2) the speed of electron is closed to

light speed, e,g., $1.5 * 10^8$ m/s. The time step is 10^{-10} when the speed of electron is much less than light speed. If the speed of electron is $1.5 * 10^8$ m/s, the time step is 10^{-13}. The region of interest r_{Max} is 10 cm in $\hat{r}$ direction and z_{Max} is 10 cm in $\hat{z}$ direction. The region of interest is divided into 1000 in each direction and the grid size is $10*10^{-2}/1000$ m. In each time step, the electron moves ~ $5.7 * 10^{-5}$ m which is much smaller than grid size when the speed of electron is much less than light speed. On the other hand, when the speed of electron is $1.5 * 10^8$ m/s, the electron moves ~ $1.5 * 10^{-5}$ m which it is much smaller than the grid size in each time step. The time step is carefully considered. Thus, the Runge-Kutta method is use to solve the electron trajectories for our simulation in the following.

4.3.2.1 Runge-Kutta method with relativistic effect

Equation 35 is rewritten as following and the 4^{th}-order Runge-Kutta method is used.

$$\frac{d\vec{X}(t)}{dt} = v = \frac{c\vec{P}}{\sqrt{m^2c^2 + P^2}} \equiv \vec{f}(t, \vec{x}, \vec{v}), \qquad \frac{d\vec{P}(t)}{dt} = q\vec{E}\left(\vec{X}(t)\right) \equiv \vec{g}(t, \vec{x}, \vec{v})$$

Each terms in Eq. 26 are given in Table. 4.

$\overrightarrow{k_1} = \Delta t\vec{f}(t_0, \overrightarrow{x_0}) = \Delta t \frac{\overrightarrow{P_0}c}{\sqrt{m^2c^2 + {P_0}^2}}$	$\overrightarrow{L_1} = \Delta t\vec{g}(t_0, \overrightarrow{x_0}) = \Delta tq\vec{E}(\overrightarrow{x_0})$
$\overrightarrow{k_2} = \Delta t\vec{f}\left(t_0 + \frac{\Delta t}{2}, \overrightarrow{x_0} + \frac{\overrightarrow{k_1}}{2}, \overrightarrow{v_0} + \frac{\overrightarrow{L_1}}{2}\right)$ $= \Delta t \frac{\overrightarrow{P^{(1)}}c}{\sqrt{m^2c^2 + {P^{(1)}}^2}};$ $\overrightarrow{P^{(1)}} = \overrightarrow{P_0} + \frac{q\vec{E}(\overrightarrow{x_0})\Delta t}{2} = \overrightarrow{P_0} + \overrightarrow{L_1}/2$	$\overrightarrow{L_2} = \Delta t\vec{g}\left(t_0 + \frac{\Delta t}{2}, \overrightarrow{x_0} + \frac{\overrightarrow{k_1}}{2}, \overrightarrow{v_0} + \frac{\overrightarrow{L_1}}{2}\right)$ $= \Delta tq\vec{E}(\overrightarrow{x^{(1)}});$ $\overrightarrow{x^{(1)}} = \overrightarrow{x_0} + \frac{\overrightarrow{P_0}c}{\sqrt{m^2c^2 + {P_0}^2}}\frac{\Delta t}{2}$ $= \overrightarrow{x_0} + \overrightarrow{k_1}/2$
$\overrightarrow{k_3} = \Delta t\vec{f}\left(t_0 + \frac{\Delta t}{2}, \overrightarrow{x_0} + \frac{\overrightarrow{k_2}}{2}, \overrightarrow{v_0} + \frac{\overrightarrow{L_2}}{2}\right)$ $= \Delta t \frac{\overrightarrow{P^{(2)}}c}{\sqrt{m^2c^2 + {P^{(2)}}^2}};$ $\overrightarrow{P^{(2)}} = \overrightarrow{P_0} + \frac{q\vec{E}\left(\overrightarrow{x^{(1)}}\right)\Delta t}{2} = \overrightarrow{P_0} + \overrightarrow{L_2}/2$	$\overrightarrow{L_3} = \Delta t\vec{g}\left(t_0 + \frac{\Delta t}{2}, \overrightarrow{x_0} + \frac{\overrightarrow{k_2}}{2}, \overrightarrow{v_0} + \frac{\overrightarrow{L_2}}{2}\right)$ $= \Delta tq\vec{E}\left(\overrightarrow{x^{(2)}}\right);$ $\overrightarrow{x^{(2)}} = \overrightarrow{x_0} + \frac{\overrightarrow{P^{(1)}}c}{\sqrt{m^2c^2 + {P^{(1)}}^2}}\frac{\Delta t}{2}$ $= \overrightarrow{x_0} + \overrightarrow{k_2}/2$
$\overrightarrow{k_4} = \Delta t\vec{f}\left(t_0 + \frac{\Delta t}{2}, \overrightarrow{x_0} + \overrightarrow{k_3}, \overrightarrow{v_0} + \overrightarrow{L_3}\right)$ $= \Delta t \frac{\overrightarrow{P^{(3)}}c}{\sqrt{m^2c^2 + {P^{(2)}}^2}};$ $\overrightarrow{P^{(3)}} = \overrightarrow{P_0} + q\vec{E}\left(\overrightarrow{x^{(2)}}\right)\Delta t$ $= \overrightarrow{P_0} + \overrightarrow{L_3}$	$\overrightarrow{L_4} = \Delta t\vec{g}\left(t_0 + \frac{\Delta t}{2}, \overrightarrow{x_0} + \overrightarrow{k_3}, \overrightarrow{v_0} + \overrightarrow{L_3}\right)$ $= \Delta tq\vec{E}\left(\overrightarrow{x^{(3)}}\right);$ $\overrightarrow{x^{(3)}} = \overrightarrow{x_0} + \frac{P^{(2)}c}{\sqrt{m^2c^2 + {P^{(2)}}^2}}\Delta t$ $= \overrightarrow{x_0} + \overrightarrow{k_3}$

Table. 4: Equation 35 is rewritten for electron motion when the electron speed is close to the light speed.

The codes are tested in two conditions: (1) the speed of electrons much less than speed of

light. The result should coincide to the classical result; and (2) the speed of electrons is closed to the speed of light. Both results are compared to the results calculated using Mathematica for benchmarking.

4.3.2.2 The speed of electron is much less than speed of light

The electron trajectories calculated using Eq. 35 should be the same as Eq. 33 when the velocity of electron is much less than speed of light. Therefore, trajectories of an electron with $573423\,(\mathrm{m/s})$ initial velocity in $\hat{r}$ direction and 0 (m/s) in $\hat{z}$ direction passing through the ideal THEA with $R_i = 2\ \mathrm{cm},\ R_o = 9\ \mathrm{cm},\ V_i = 6\ \mathrm{V},\ V_o = 2\ \mathrm{V}$ was calculated. Both Eq. 33 and Eq. 35 were used and the results are plotted in blue and green lines, respectively, in Fig. 23. The equations of motion with and without relativistic were also solved using Mathematica and the results are plotted in yellow points and brown line, respectively, in Fig. 23. In Fig. 23, simulation results of electron trajectories calculated using our code to calculate Eq. 33 and Eq. 35 are compared with the results calculated by using Mathematica. They coincide to each others. It shows that our code is correct in the case of electrons with speed much less than the speed of light.

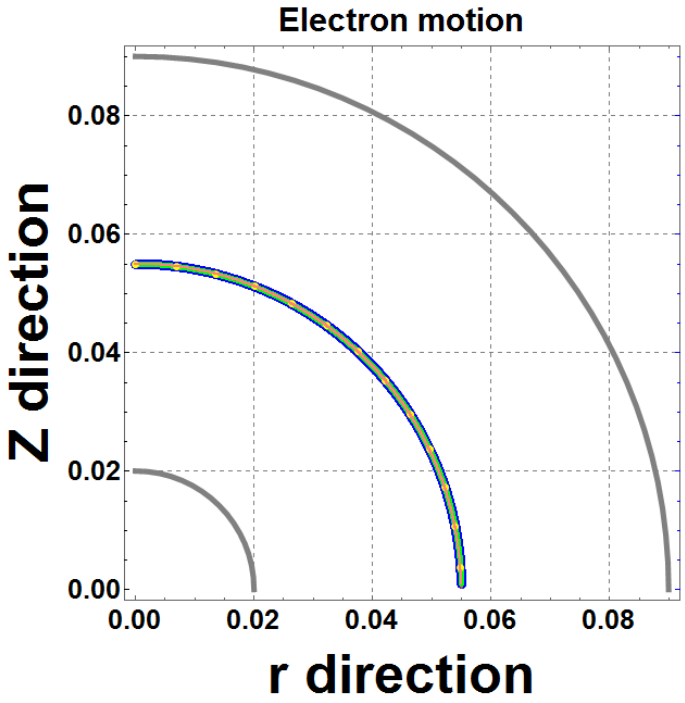

Figure. 23: The simulation result of electron trajectories is compared with the result calculated using Mathematica in two concentric metal spheres where the radii and potentials of the inner and the outer are 2 cm, 9 cm, 6 V, 2 V, respectively. Blue and green lines represent the numerical calculation. Yellow points and brown line represent the simulation results.

4.3.2.3 The speed of electron is closed to the speed of light

To check if the trajectories are calculated correctly, we simulate the case where the speed of electron is half of the speed of light. The initial position of the electron is (r,z)=(0 cm , 5.5 cm). The initial velocity of the electron is $1.5 * 10^8$ m/s in $\hat{r}$ direction and 0 m/s in $\hat{z}$ direction. The radius of the inner and outer sphere are 2 cm and 9 cm, respectively, while the inner and outer voltage are now $3.05 * 10^5$ V and 2 V, respectively. The equation

of motion with and without relativistic were also solved using Mathematica and the results are plotted in green solid line and black dashed line, respectively, in Fig. 24. In Fig. 24, simulation results of electron trajectories calculated using our code to calculate Eq. 33 and Eq. 35 are compared with the results calculated by using Mathematica. In Fig. 24, the colorful dashed line is from simulation result with non-relativistic. The blue solid line represents the simulation result with relativistic effect. In ideal THEA, the simulation result of electron trajectories with Eq. 33 and Eq. 35 is identical with analytic result. According to Fig. 24, the simulation result for electron trajectories is correct in ideal THEA.

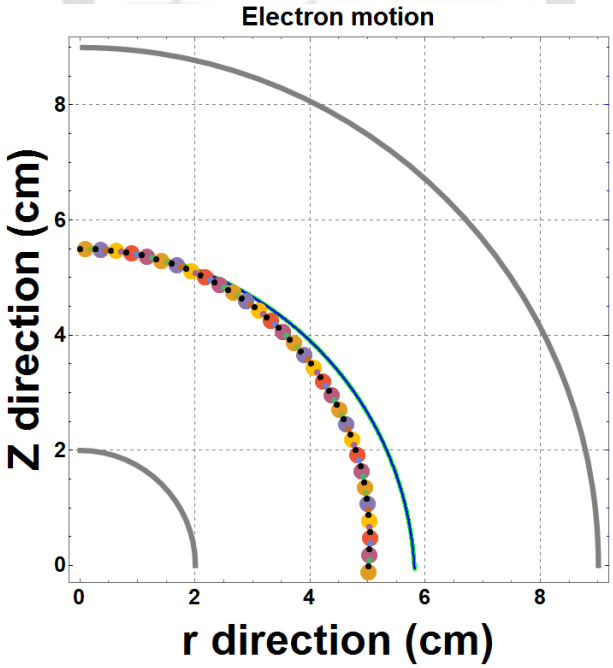

Figure. 24: The simulation result of electron trajectories is compared with the analytic result in two concentric metal spheres where the radii and potentials of the inner and the outer are 2 cm, 9 cm, $3.05*10^5$ V, 2 V, respectively.

4.3.3 Summary

The code have already been compared with relativistic effect and non-relativistic effect. As a result, the simulation result of electron trajectories with relativistic effect in FORTRAN is consistence with calculation by using Mathematica.

Previous results shown in section 4.2 and 4.3 used two concentric metal spheres as an ideal spherical THEA. However, an actual THEA is consisting of two shells and two parallel plates as the collimator on the top of the outer sphere and shown in Fig. 2. Also, the actual THEA is only hemisphere. The actual THEA of electric potentials and electron trajectories are given and introduced in the next section. The previous result of electric potentials are calculated in the ideal THEA in the first quadrant. Additionally, electric potentials in the first quadrant are mapping to the second quadrant. Then, electric fields can be calculated by taking negative of the gradient of the calculated electric potential. So, the electric fields in the hemisphere of actual THEA is obtained.

In this chapter, we confirmed our code is correct. In section 4.1, we introduced all the numerical method we used. In section 4.2, we benchmarked the Laplace's equation solver for an ideal THEA. In section 4.3, the simulation result of trajectories of electrons were compared with analytical solution. Also, the relativistic and non-relativistic were considered.

CHAPTER 5 SIMULATION RESULTS OF THEA

In the previous chapter, we have shown that our codes calculate electric potentials, electron trajectories in an ideal THEA correctly. From zeroth order approximation in chapter 3, we have shown that a THEA with $R_i = 44\ \text{mm}, R_0 = 45\ \text{mm}, V_i = 1\ \text{kV}, V_0 = 0\ \text{V}$ (capable to be fit in a cubesat) can capture the electron up to 20 keV. In this chapter, we will further verify the approximation and calculate the selectivity of the THEA, i.e., the g-factor. In section 5.1, the dimensions and the calculated electric potential of an actual THEA are given. In section 5.2, electron trajectories are shown. Finally in section 5.3, a bunch of electrons with different initial energies, incident angles, and incident positions are used to calculate the g-factor of the THEA.

5.1 The electric potential of an actual THEA

For the actual THEA, a collimator is installed on the top of outer sphere. Therefore, the electric potential is a little different from that calculated in the section 4.2. Collimators are added through adding more special points described in section 4.2 in the ROI. Notice that "Flag technique" is used to shorten the calculation time since the gap between two spheres is only 1 mm. The area is only a small fraction of the total ROI. Figure 25 shows the cross

section of a real THEA which is divided into several small regions, as designated as A, B, C and the others. In Fig. 25, it represents the shape of a THEA in the simulation code.

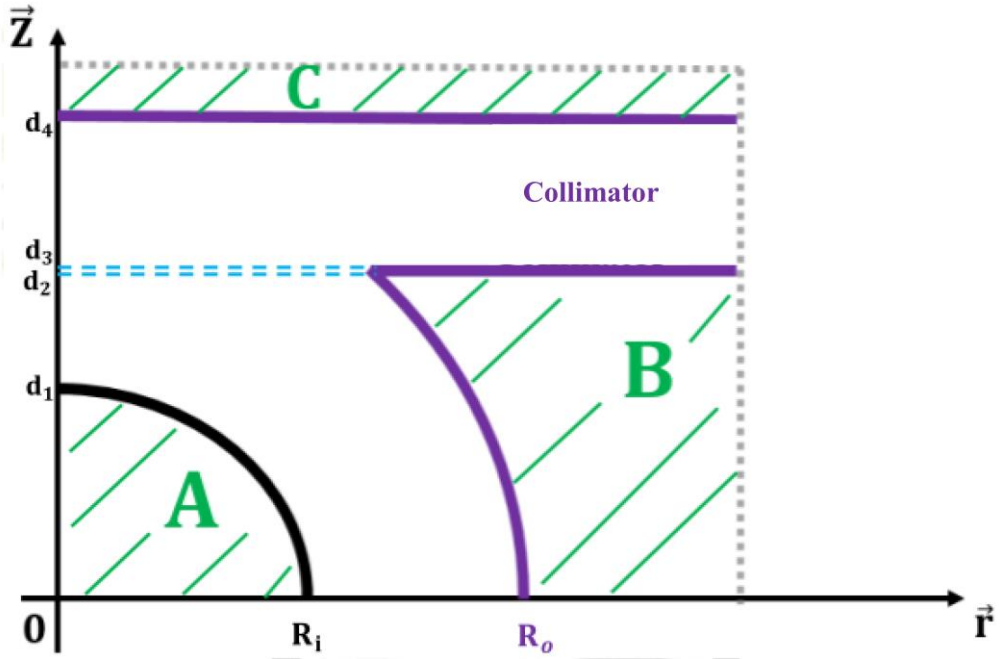

Figure. 25: Two parallel plates as the collimator are installed on top of analyzer. d_1, d_2, d_3 and d_4 represent the inner radius, the height of lower collimator, the height plus the thickness of the lower collimator and the height of the upper collimator, respectively.

The region of A, B and C are given as following.

(1) A : $\sqrt{r^2 + z^2} \leq R_i$.

(2) B : $z < d_2$ and $\sqrt{r^2 + z^2} \leq R_o$.

(3) C : $z > d_4$.

For the special points, it will cause big difference in our simulation. When the point is closed to the shell of THEA, we have to consider the effect on our simulation. We compare the

distance between points and the sphere with the grid size when the point is closed to the shell of THEA. Therefore, Fig. 25 will be divided into several regions. The first region is at $z < d_2$ in Fig. 26.

(1) The first region for points is shown in Fig. 26.

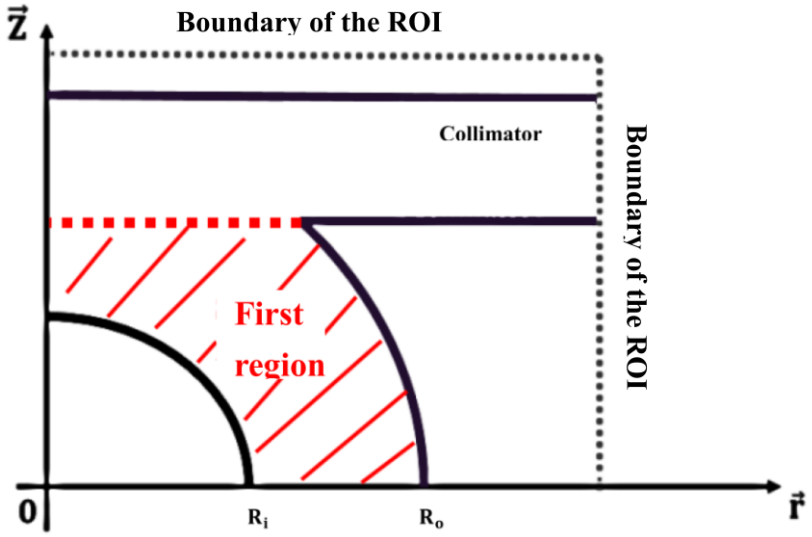

Figure. 26: The special points in the first region are considered when the $z < d_2$.

(2) The second region is shown in Fig. 27 and Fig. 28. The special points near the lower collimator at $d_2 \leq z \leq d_3$ are considered.

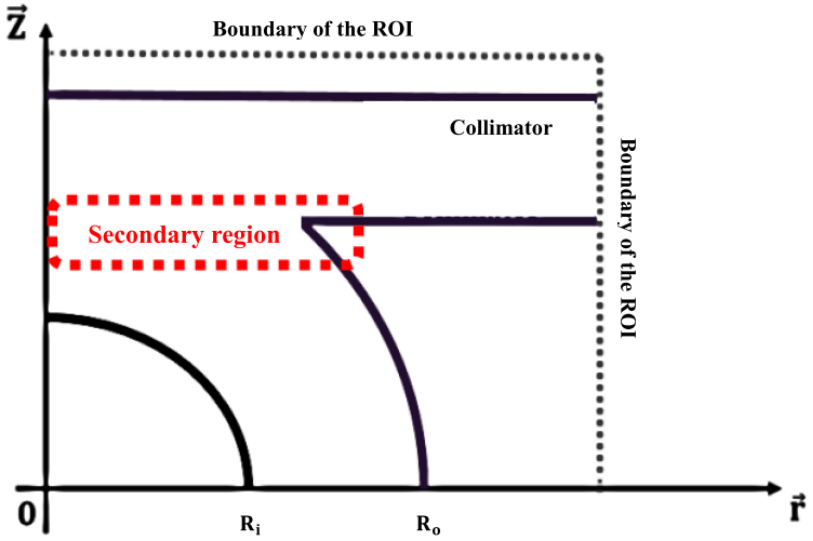

Figure. 27: The special points in the third region are considered when the range of z at $d_2 \leq z \leq d_3$.

Figure. 28: Third region is zoomed in. The thickness of collimator have to consider for the special points at $d_2 \leq z \leq d_3$.

.

(3) The third region for points at $d_3 < z \leq d_3 + dz$ is shown in Fig. 29.

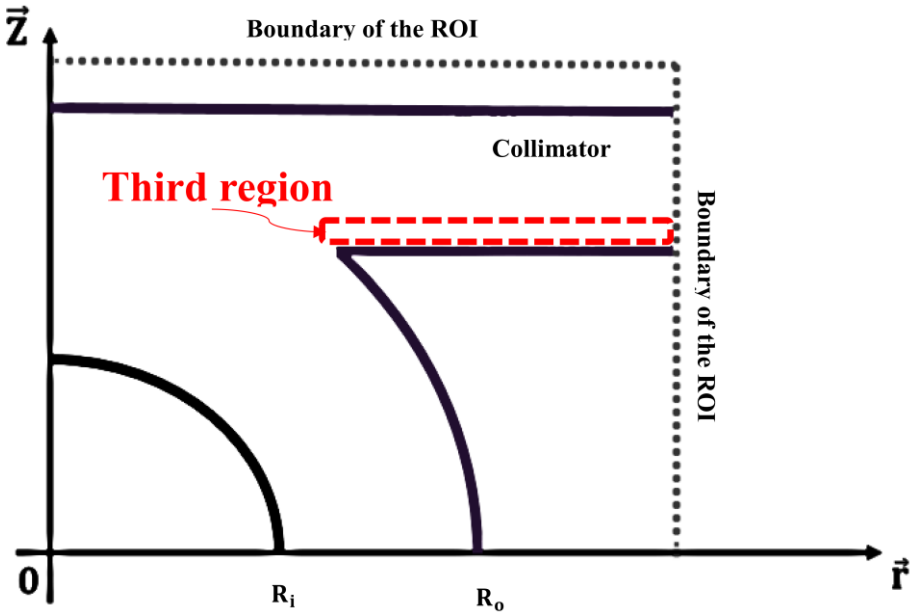

Figure. 29: The special points in the third region are considered at $d_3 < z \leq d_3 + dz$.

(4) The fourth region for points at $z \geq d_4 - dz$ is shown in Fig. 30.

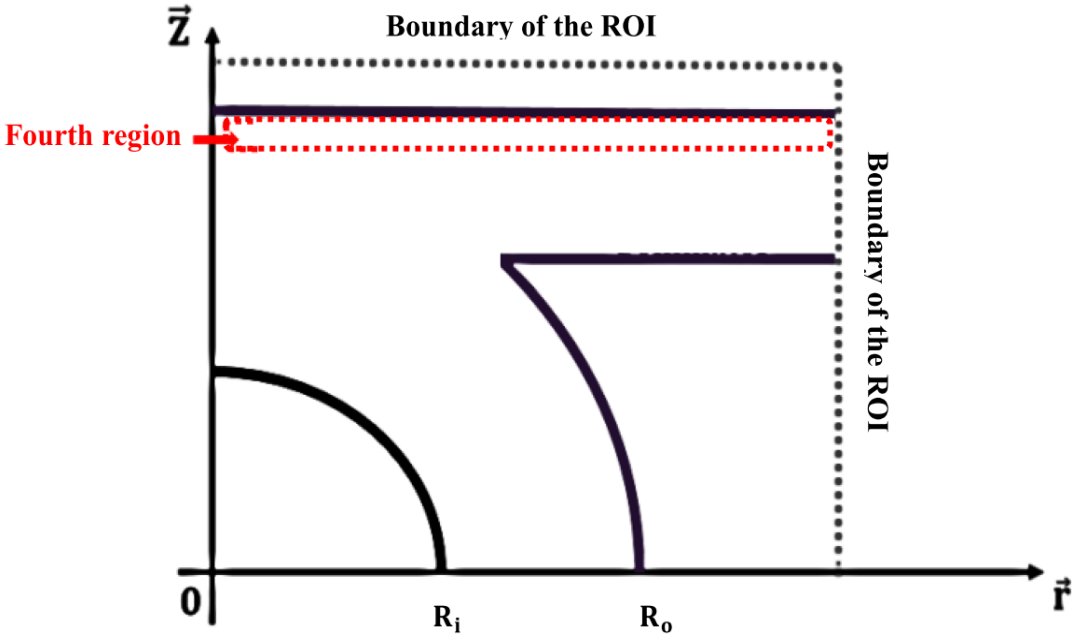

Figure. 30: The special points in the fourth region are considered at $z \geq d_4 - dz$.

The electric potential in an actual THEA with the inner and outer radii and potentials of

0.044 m, 0.045 m, 1 kV, 0 V, respectively, is shown in Fig. 31. Notice that only half of the THEA was simulated due to the symmetry.

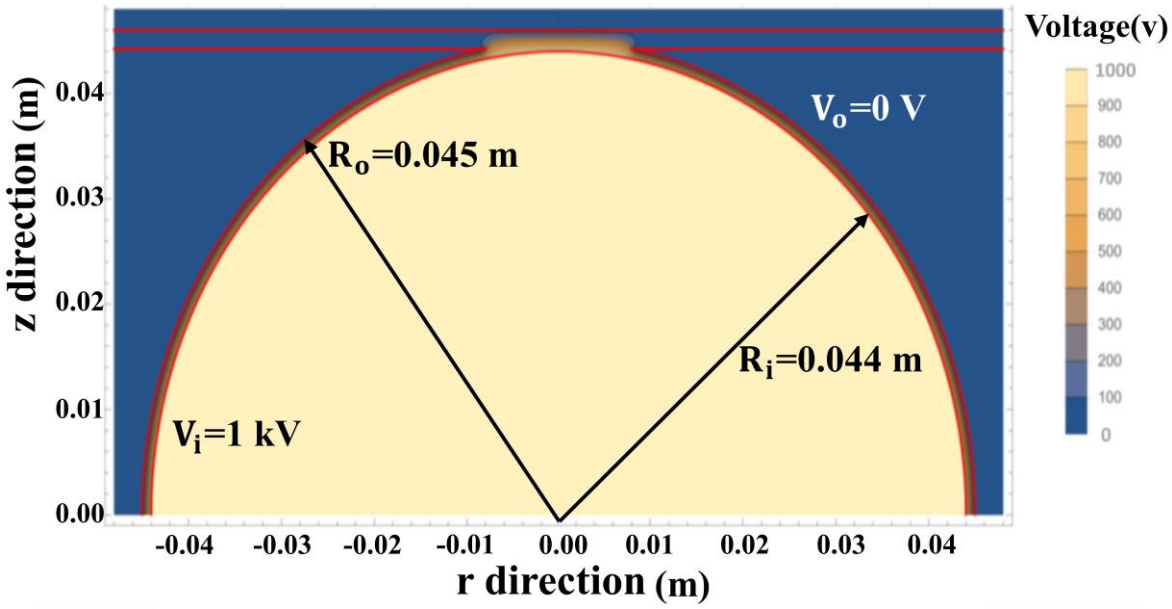

Figure. 31: Shows the calculated electric potential of an actual THEA where the radii and potentials of the inner and the outer are 0.044 m, 0.045 m, 1 kV, 0 V, respectively.

Different from the electric potential in an ideal THEA given in section 4.2, the electric potential is not zero at the intersection of the outer sphere and the collimator. However, we only calculated the electric potential in first quadrant. Additionally, electric potentials in the first quadrant are mapped to the second quadrant because the THEA is a symmetric sphere. Electric fields can be calculated by taking negative of the gradient of the electric potential. Therefore, the distribution of electric fields in a hemisphere of actual THEA is obtained.

5.2 Electron trajectories

Shown in Fig. 32 are trajectories of electrons with different kinetic energy in the THEA. The initial positions of these electrons are at (r,z)=(-0.04 m , 0.04489 m). For a given voltage, only electrons with particular energy can pass through the analyzer. Shown in Fig. 33 are the zoom in view of the trajectories. Only electron with energy equals 21.708 keV can pass through the THEA. For electron with larger energy, the electron collides with the outer sphere while the one with lower energy collides to the inner sphere.

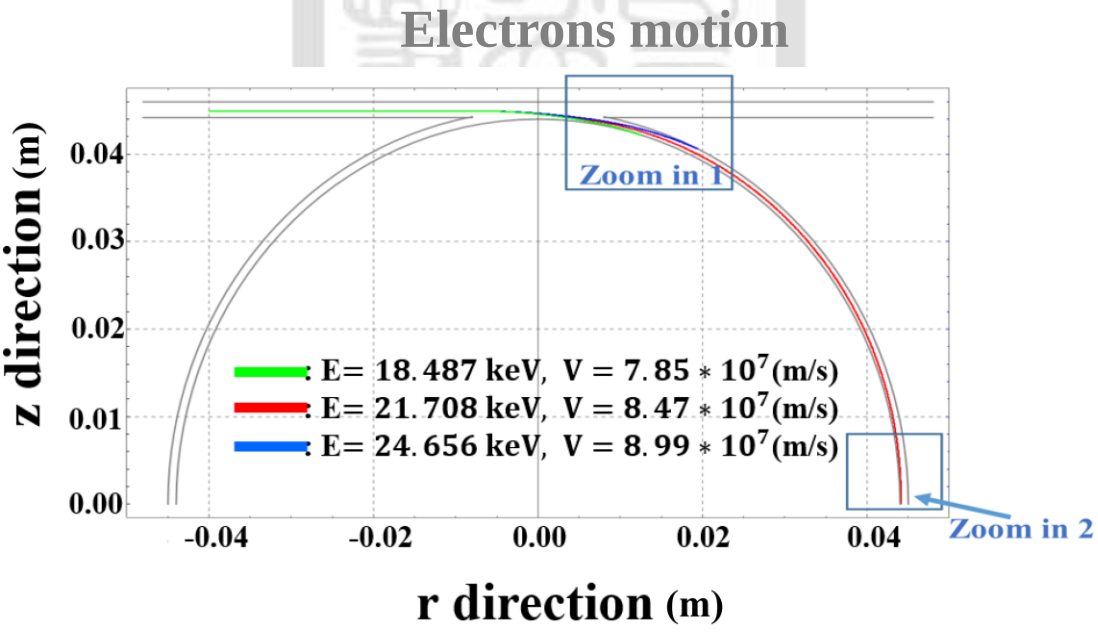

Figure. 32: Electron trajectories with different energies are given where the radii and potentials of the inner and the outer are 44 mm, 45 mm, 1 kV, 0 V, respectively. The initial position of electron is (-0.04 m, 0.0448 m). The green line, red line blue line represent the electron energy with 18.487 keV, 21.708 keV and 24.656 keV, respectively.

Zoom in 1

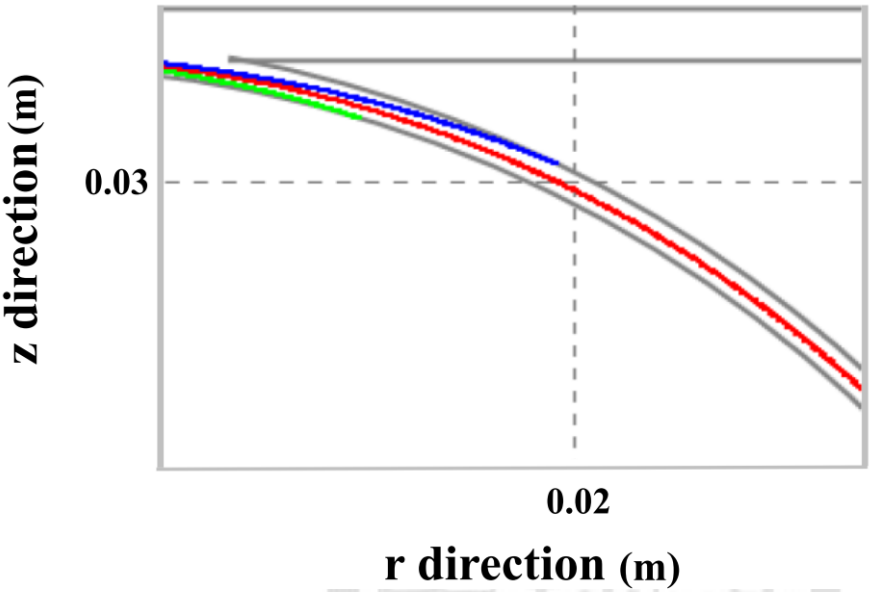

Zoom in 2

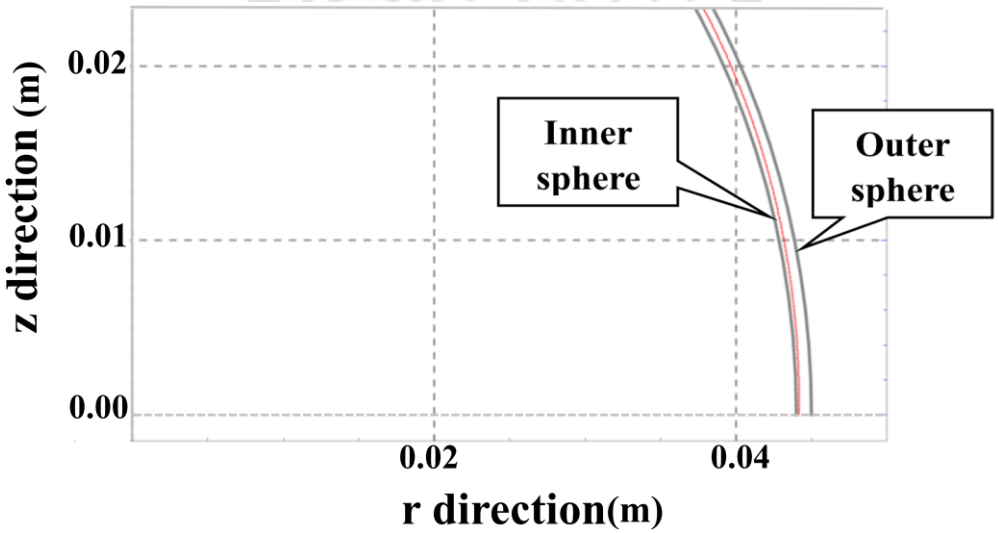

Figure. 33: Only particular energy of electrons can pass through the analyzer.

From the zeroth order estimation, electrons with energy of 22.2 keV can pass through the THEA with R_I, R_o, V_I and V_o equal to 44 mm, 45 mm, 1 kV, and 0 V, respectively. With

more accurate simulation, electrons with energy of 21.71 keV can pass through the THEA.

5.3 G-factor calculation

Geometric-factor (g-factor) is the selectivity of the detector. The formula was given in chapter 3:

$G = \frac{G_E}{\langle k \rangle}$ with

$$G_E \equiv \int T(K, \Omega, \vec{x})(\hat{j} \cdot \hat{n}) dS\, d\Omega dK,$$

$$\langle k \rangle \equiv \frac{\int KT(K, \Omega, \vec{x})(\hat{j} \cdot \hat{n}) dS\, d\Omega dK}{\int T(K, \Omega, \vec{x})(\hat{j} \cdot \hat{n}) dS\, d\Omega dK}.$$

To calculate G_E and $\langle k \rangle$, trajectories of a bunch of electron with different initial energy incident angles, and incident positions are simulated. The initial conditions of those electrons that pass through the THEA are recorded and used to calculate G_E and $\langle k \rangle$ using the following equation :

$$G_E \equiv \int T(K, \Omega, \vec{x})(\hat{j} \cdot \hat{n}) dS\, d\Omega dK$$

$$\Longrightarrow G_E = \int T(K, \theta, \vec{x}) \cos\theta\, 2\pi R \cdot dz \cdot \sin\theta d\theta 2\pi dK$$

$$\Longrightarrow G_E = 4\pi^2 R \int_0^{K_{max}} dk \int_{-\pi/2}^{\pi/2} d\theta \sin\theta\cos\theta \int_{\text{lower collimator}}^{\text{upper collimator}} T(K, \theta, \vec{x}) dz$$

$$\Longrightarrow G_E = \frac{4\pi^2 R\, dk\, d\theta \sum_{\text{electrons passing through THEA}} \sin\theta\cos\theta T(K, \theta)}{\text{Total number of simulation electrons}} \quad (36a)$$

where R is the radius of the collimator. In our simulation, the R is 4.

Similarly,

$$< k >\equiv \frac{\int KT(K,\Omega,\vec{x})(\hat{j}\cdot\hat{n})dS\,d\Omega dK}{\int T(K,\Omega,\vec{x})(\hat{j}\cdot\hat{n})dS\,d\Omega dK} \equiv \frac{\int KT(K,\Omega,\vec{x})(\hat{j}\cdot\hat{n})dS\,d\Omega dK}{G_E} \quad (36b)$$

$$\Rightarrow < k >$$

$$= \frac{4\pi^2 R\int_0^{K_{max}} Kdk\int_{-\pi/2}^{\pi/2} d\theta\sin\theta\cos\theta\int_{\text{lower collimator}}^{\text{upper collimator}} T(K,\theta,\vec{x})dz}{G_E}$$

$$\Rightarrow < k >= \frac{\frac{4\pi^2 R\,dk\,d\theta\sum_{\text{electrons passing through THEA}} K\sin\theta\cos\theta T(K,\theta)}{\text{Total number of electron}}}{G_E}$$

$T(K,\theta)$ represents the total number of electrons that can pass through the bottom of the detector as a function of electron kinetic energy and incident angles. In our simulation for g-factor, a bunch of electrons with the electron kinetic energy from 0 eV to 25 keV, the incident angles from -5° to 5°, and the incident location z from 44.4 mm to 46 mm incident to a THEA with the inner radius, outer radius, inner voltage and outer voltage of 44 mm, 45 mm, 1 kV and 0 V, respectively. The energies, incident angles, and the locations were given using 3 different random numbers.

5.3.1 Initial conditions

In our simulation, the distribution of electron kinetic energies, incident angles and positions in $\hat{z}$ direction for 10^4 electrons are shown in Fig. 34-36, respectively. White noise random numbers were used so that flat distributions are shown in those figures.

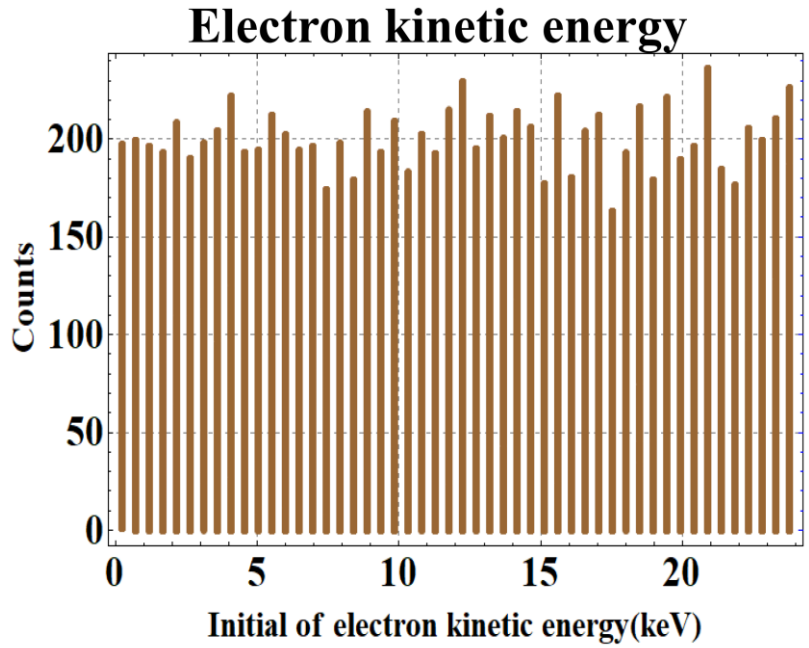

Figure. 34: The distribution of electron kinetic energy for calculating g-factor in our simulation.

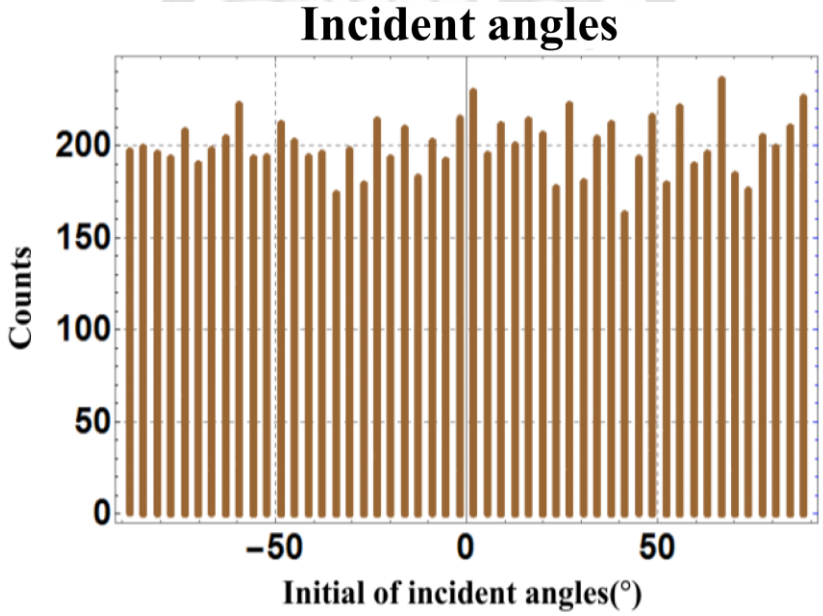

Figure. 35: The distribution of incident angle for calculating g-factor in our simulation.

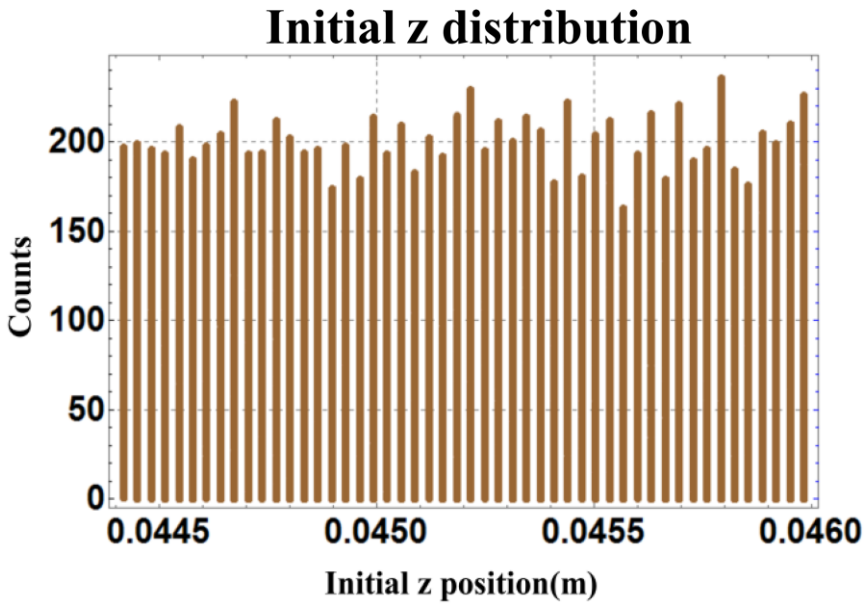

Figure. 36: The distribution of position used to decide the initial position of electron in $\hat{z}$ direction in our simulation.

5.3.2 G-factor calculations

Simulations of different number of incident electrons are shown in Table 5. The second column, third column, fourth column, fifth column, sixth column represent, the g-factor, how many electrons enter the THEA, how many electrons will be detected at the bottom of the detector, energy g-factor and mean energy, respectively. Figure. 37 shows the simulated results of T(K,θ) with different number of electrons used in the simulation. Figure. 37(a) – 37(f) corresponds to Group A-F in Table 5. The G_E and $\langle k \rangle$ were calculated using the T(K,θ) in Fig. 37 and Eq. 37a-37b .

Groups	G $\equiv G_E/\langle k\rangle$ (cm^2srkeV/keV)	Number of electrons on simulation	Number of detected electrons	G_E (cm^2srkeV)	$\langle k\rangle$ (keV)
A	$2.64 * 10^{-4}$	10^9	276580	$5.78 * 10^{-3}$	21.72
B	$2.64 * 10^{-4}$	10^8	27733	$5.73 * 10^{-3}$	21.73
C	$2.58 * 10^{-4}$	10^7	2693	$5.62 * 10^{-3}$	21.72
D	$2.17 * 10^{-4}$	10^6	253	$4.47 * 10^{-3}$	21.84
E	$1.93 * 10^{-4}$	10^5	27	$4.19 * 10^{-3}$	21.70
F	$4.12 * 10^{-4}$	10^4	4	$8.83 * 10^{-3}$	21.40

Table. 5: The electrons with different number are considered.

As shown in Table. 5 , the g-factor converged to $2.64 * 10^{-4}$(cm^2-sr-keV/keV) when the number of electrons became larger and larger. It can also be shown using the statistics error defined as

$$\frac{1}{\sqrt{\text{the number of electrons is detected at the bottom of the detector}}}.$$

The statistics errors of different simulations are listed in Table. 6.

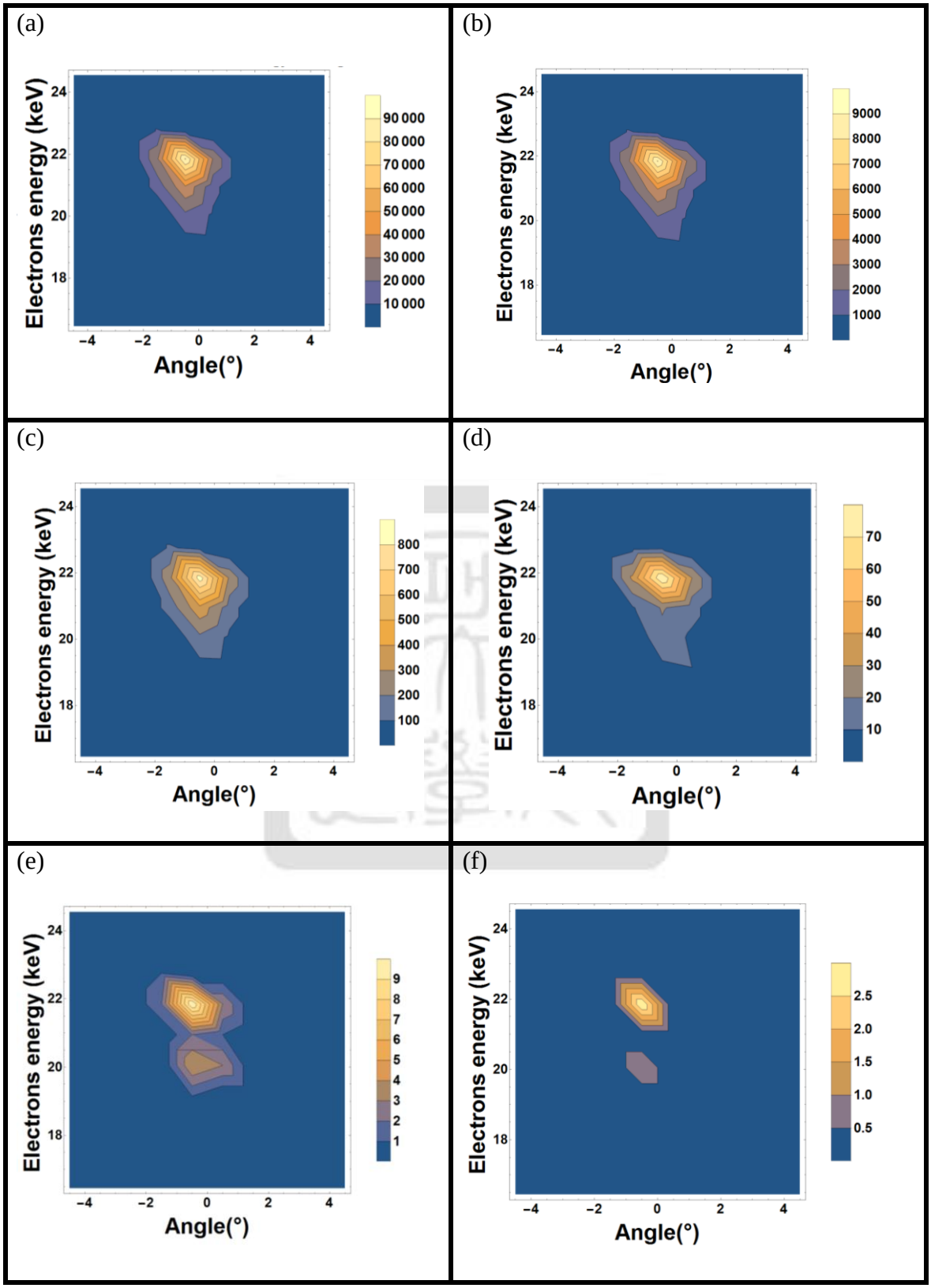

Figure. 37: The different number of electrons for energy-elevation are presented. Figure. 37

means only particular energies of electrons and angles which it is close to zero can pass through analyzer.

Groups	Electrons are detected	Error of statistics
A	276580	0.19%
B	27733	0.6%
C	2693	1.9%
D	253	6.2%
E	27	19.2%
F	4	50.0%

Table. 6: The error of statistics corresponds to each group.

As the result, the g-factor from simulations converge to 2.64 * 10^{-4}(cm^2-sr-keV/keV) with 0.19 % uncertainty.

CHAPTER 6 CONCLUSION AND SUMMARY

In this thesis, a top hat electrostatic analyzer (THEA) that can be fitted in a cubesat for measuring electrons was designed. Cubesat, THEA, and several numerical method were first introduced. The zeroth order approximation showed that building a THEA for cubesats to measure the electron distribution functions up to ~ 22.2 keV is possible. A more accurate calculation using the code developed by ourselves showed that electron with energy of 21.71 keV can be detected using a THEA with R_I, R_o, V_I and V_o equal to 44 mm, 45 mm, 1 kV, and 0 V, respectively. The electric potentials were simulated via solving Laplace equation using Gauss-Seidel method in cylindrical coordinate. A 〝flag technique〞 where only points between two spheres were calculated to speed up the simulation, was used. Trajectories of electrons with Relativistic effect in THEA were calculated using the 4^{th}-order Runge-Kutta method. The code we developed were first benchmarked by using the ideal THEA consisting of two concentric metal spheres. By comparing the simulation results to the analytical models, we confirmed the code that calculate Laplace's equation, the electric fields in any locations within ROI, and the trajectories of electrons with and without relativistic effect were correct. As a result, we showed that the g-factor of the THEA is $2.64 * 10^{-4} \pm 0.19\%$ (cm^2-sr-keV/keV).

CHAPTER 7 FUTURE WORKS

We obtained the g-factor of the THEA that can fit in a cubesat. However, there are more works need to be done to obtain a THEA that can really be used.

- **Three-dimensional calculation**

Electron trajectories and electric potentials have already been calculated for a THEA in 2D. To be closed to reality, electric potentials and electron trajectories need to be calculated in 3D.

- **The THEA will be optimized**

The shape of the THEA will be optimized via getting the highest g-factor with physical constrain. The commodity used THEA, it is a little difference from Fig. 32. In Fig. 32, the offset of the shell center from the symmetric axis is zero. However, the “actual” THEA the offset of the shell center from the symmetric axis is not zero[19][20][21] which is shown in Fig. 38. In Fig. 38, a is the deflection angle of the energy analyzer, b is the offset of the shell center from the symmetric axis, c is the eight of the upper collimator measured from the topmost edge of the outer shell, and d is the thickness of the lower collimator plate[22]. An optimized THEA needs to be obtained via more simulations.

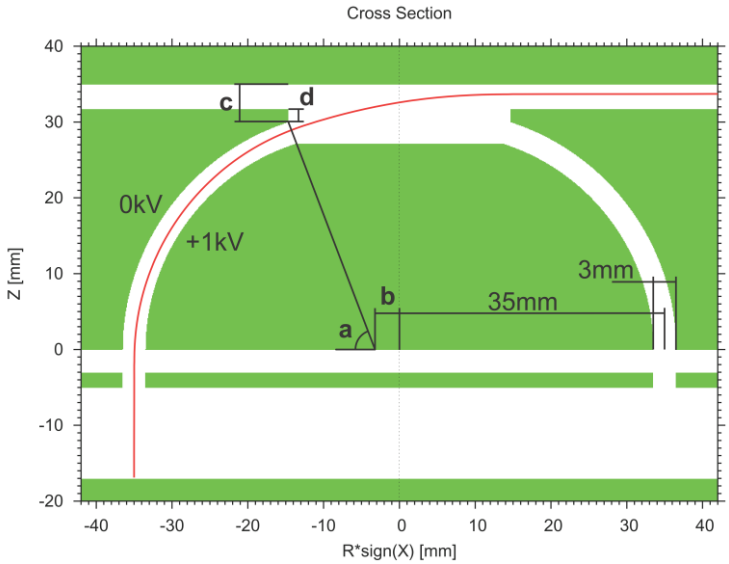

Figure. 38: The structure of an actual THEA are presented. The a, b, c , d represent the deflection angle of the energy analyzer, the offset of the shell center from the symmetric axis the eight of the upper collimator measured from the topmost edge of the outer shell, and the thickness of the lower collimator plate, respectively[13].

- **Physical test**

After optimization, an actual THEA will be built and tested using the optimized parameters. Following are items that need to be tested: weight test, breakdown voltage test, power consumption test, testing platform and UV/radiation considerations. It is important to prevent ultraviolet (UV) photons from reaching the detector causing noise from photon counts since multi-channel plates is sensitive to UV photons. Scattering in the analyzer will further be considered via photon tracing simulations using Geant4[23][24][25] and tested experimentally in the future.

REFERENCE

[1]. http://earthsky.org/earth/what-causes-the-aurora-borealis-or-northern-lights

[2]. Chien-Hsiu Ho, Development of aurora electron spectrometer, 2012

[3]. Berger, M. J., S. M. Seltzer, K. Maeda (1970), Energy deposition by auroral electrons in atmosphere, J Atoms Terr Phys, 32:1015-1045

[4]. https://www.cubesatshop.com/product/cubesat-solar-panels-complete-set/

[5]. K. Shiokawa, K. Seki, Y. Miyoshi, A. Ieda, T. Ono, M. Iizima, T. Nagatsuma, T. Obara, T. Takashima, K. Asamura, Y. Kasaba, A. Matsuoka, Y. Saito, H. Saito, M. Hirahara, Y. Tonegawa, F. Toyama, M. Tanaka, M. Nose, Y. Kasahara, K. Yumoto, H. Kawano, A. Yoshikawa, Y. Ebihara, A. Yukimatsu, N. Sato, and S. Watanabe. Erg - a small-satellite mission to investigate the dynamics of the inner magnetosphere

[6]. http://www.spacex.com/about/capabilities

[7]. 方振洲,發射台灣的立方衛星, 科學發展期刊,517 期,2016 年 1 月

[8]. 莊智清, 庶民衛星天上看, 科學人期刊, 2011 年 4 月.

[9]. http://www.lunarsail.com/what-is-a-cubesat/

[10]. https://gomspace.com/Shop/subsystems/Default.aspx

[11]. https://www.estcube.eu/en/home

[12]. http://www.cubesat.org/

[13]. Y.Kazama, Design a toroidal top-hat energy analyzer for low-energy electron measurement, An Introduction to Space Instrumentation, 181–192, 2013.

[14]. http://www.iiserpune.ac.in/~pgoel

[15]. http://lpsa.swarthmore.edu/NumInt/NumIntFourth.html##section8

[16]. Autar Kaw, Numerical Methods with Applications: Abridged, Autarkaw, US, 2010

[17]. Mathematics & Science Learning Center Computer Laboratory

[18]. http://www.mathematik.uni-dortmund.de

[19]. William H. Press, Numerical Recipes in C: The Art of Scientific Computing, CAMBRIDGE UNIVERSITY PRESS, UK, 707-747, 1992

[20]. Wurz et al. (2007), Calibration techniques, in Calibration of Particle Instruments in Space Physics, ISSI Scientific Report, vol.7

[21].P. Wurz, A. Balogh, V. Coffey, B. K. Dichter, W. T. Kasprzak, A. J. Lazarus, W. Lennartsson, and J. P. McFadden. Calibration techniques. ISSI Scientific Reports Series, 7:117–276, 2007.

[22].K. Oyama and C. Z. Cheng, editors. *An Introduction to Space Instrumentation*. 2013.

[23].S. Agostinelli, J. Allison, K. Amako, J. Apostolakis, H. Araujo, P. Arce, M. Asai, D. Axen, S. Baner- jee, G. Barrand, F. Behner, L. Bellagamba, J. Boudreau, L. Broglia, A. Brunengo, H. Burkhardt, S. Chauvie, J. Chuma, R. Chytracek, G. Cooperman, G. Cosmo, P. Degtyarenko, A. Dell'Acqua, G. Depaola, D. Dietrich, R. Enami, A. Feliciello, C. Ferguson, H. Fesefeldt, G. Folger, F. Foppi- ano, A. Forti, S. Garelli, S. Giani, R. Giannitrapani, D. Gibin, J.J. Gomez Cadenas, I. Gonzalez, G. Gracia Abril, G. Greeniaus, W. Greiner, V. Grichine, A. Grossheim, S. Guatelli, P. Gumplinger, R. Hamatsu, K. Hashimoto, H. Hasui, A. Heikkinen, A. Howard, V. Ivanchenko, A. Johnson, F.W. Jones, J. Kallenbach, N. Kanaya, M. Kawabata, Y. Kawabata, M. Kawaguti, S. Kelner, P. Kent, A. Kimura, T. Kodama, R. Kokoulin, M. Kossov, H. Kurashige, E. Lamanna, T. Lampen, V. Lara, V. Lefebure, F. Lei, M. Liendl, W. Lockman, F. Longo, S. Magni, M. Maire, E. Medernach, K. Mi- namimoto, P. Mora de Freitas, Y. Morita, K. Murakami, M. Nagamatu, R. Nartallo, P. Nieminen, T. Nishimura, K. Ohtsubo, M. Okamura, S. O'Neale, Y. Oohata, K. Paech, J. Perl, A. Pfeiffer, M.G. Pia, F. Ranjard, A. Rybin, S. Sadilov, E. Di Salvo, G. Santin, T. Sasaki, N. Savvas, Y. Sawada, S. Scherer, S. Sei, V. Sirotenko, D. Smith, N. Starkov, H. Stoecker, J. Sulkimo, M. Takahata, S. Tanaka, E. Tcherniaev, E. Safai Tehrani, M. Tropeano, P. Truscott, H. Uno, L. Urban, P. Ur- ban, M. Verderi, A. Walkden, W. Wander, H. Weber, J.P. Wellisch, T. Wenaus, D.C. Williams, D. Wright, T. Yamada, H. Yoshida, and D. Zschiesche. Geant4 - a simulation toolkit. Nuclear Instruments and ftethods in Physics Research Section A: Accelerators, Spectrometers, Detectors and Associated Equipment, 506(3):250 – 303, 2003.

[24].J. Allison, K. Amako, J. Apostolakis, P. Arce, M. Asai, T. Aso, E. Bagli, A. Bagulya, S. Baner- jee, G. Barrand, B.R. Beck, A.G. Bogdanov, D. Brandt, J.M.C. Brown, H. Burkhardt, Ph. Canal, D. Cano-Ott, S. Chauvie, K. Cho, G.A.P. Cirrone, G. Cooperman, M.A. Cortes-Giraldo, G. Cosmo, G. Cuttone, G. Depaola, L. Desorgher, X. Dong, A. Dotti, V.D. Elvira, G. Folger, Z. Francis, A. Ga- loyan, L. Garnier, M. Gayer, K.L. Genser, V.M. Grichine, S. Guatelli, P. Gueye, P. Gumplinger, A.S. Howard, I. Hrivnacova, S. Hwang, S. Incerti, A. Ivanchenko, V.N. Ivanchenko, F.W. Jones, S.Y. Jun, P. Kaitaniemi, N. Karakatsanis, M. Karamitros, M. Kelsey, A. Kimura, T. Koi, H. Kurashige, A. Lechner, S.B. Lee, F. Longo, M. Maire, D. Mancusi, A. Mantero, E.

Mendoza, B. Morgan, K. Murakami, T. Nikitina, L. Pandola, P. Paprocki, J. Perl, I. Petrovic, M.G. Pia, W. Pokorski, J.M. Quesada, M. Raine, M.A. Reis, A. Ribon, A. Ristic Fira, F. Romano, G. Russo, G. Santin, T. Sasaki, D. Sawkey, J.I. Shin, I.I. Strakovsky, A. Taborda, S. Tanaka, B. Tome, T. Toshito, H.N. Tran, P.R. Truscott, L. Urban, V. Uzhinsky, J.M. Verbeke, M. Verderi, B.L. Wendt, H. Wenzel, D.H. Wright, D.M. Wright, T. Yamashita, J. Yarba, and H. Yoshida. Recent developments in geant4. Nuclear Instruments and ftethods in Physics Research Section A: Accelerators, Spectrom- eters, Detectors and Associated Equipment, 835:186 – 225, 2016.

[25].J. Allison, K. Amako, J. Apostolakis, H. Araujo, P. Arce Dubois, M. Asai, G. Barrand, R. Capra, S. Chauvie, R. Chytracek, G. A. P. Cirrone, G. Cooperman, G. Cosmo, G. Cuttone, G. G. Daquino, M. Donszelmann, M. Dressel, G. Folger, F. Foppiano, J. Generowicz, V. Grichine, S. Guatelli, P. Gumplinger, A. Heikkinen, I. Hrivnacova, A. Howard, S. Incerti, V. Ivanchenko, T. Johnson, F. Jones, T. Koi, R. Kokoulin, M. Kossov, H. Kurashige, V. Lara, S. Larsson, F. Lei, O. Link, F. Longo, M. Maire, A. Mantero, B. Mascialino, I. McLaren, P. Mendez Lorenzo, K. Minami- moto, K. Murakami, P. Nieminen, L. Pandola, S. Parlati, L. Peralta, J. Perl, A. Pfeiffer, M. G. Pia, A. Ribon, P. Rodrigues, G. Russo, S. Sadilov, G. Santin, T. Sasaki, D. Smith, N. Starkov, S. Tanaka, E. Tcherniaev, B. Tome, A. Trindade, P. Truscott, L. Urban, M. Verderi, A. Walkden, J. P. Wellisch, D. C. Williams, D. Wright, and H. Yoshida. Geant4 developments and applications. IEEE Transactions on Nuclear Science, 53(1):270–278, Feb 2006.

APPENDIX A

The derivation of finite difference form

The $\frac{\partial V^2(r,z)}{\partial r^2}$ is from below:

$$V(r+dr_2,z) = V(r,z) + V'(r,z)dr_2 + \frac{\frac{\partial V^2(r,z)}{\partial r^2}}{2!} dr_2{}^2 + \cdots \quad ①$$

$$V(r-dr_1,z) = V(r,z) - V'(r,z)dr_1 + \frac{\frac{\partial V^2(r,z)}{\partial r^2}}{2!} dr_1{}^2 + \cdots \quad ②$$

① + ②

$$\Longrightarrow V(r+dr_2,z) + V(r-dr_1,z) - 2V(r,z) - (dr_2 - dr_1)V'(r,z) = \frac{1}{2}\frac{\partial V^2(r,z)}{\partial r^2}\left(dr_1{}^2 + dr_2{}^2\right)$$

$$\Longrightarrow \frac{\partial V^2(r,z)}{\partial r^2} = \frac{2}{dr_1{}^2 + dr_2{}^2}[V(r+dr_2,z) + V(r-dr_1,z) - 2V(r,z) - (dr_2 - dr_1)V'(r,z)]$$

Moreover, $\frac{\partial V(r,z)}{\partial r} = \frac{V(r+dr_2,z) - V(r-dr_1,z)}{dr_1+dr_2}$

$$\Longrightarrow \frac{\partial V^2(r,z)}{\partial r^2} = \frac{2}{dr_1{}^2 + dr_2{}^2}\left[\begin{matrix} V(r+dr_2,z) + V(r-dr_1,z) - 2V(r,z) \\ -(dr_2 - dr_1)\frac{V(r+dr_2,z) - V(r-dr_1,z)}{dr_1 + dr_2} \end{matrix}\right].$$

The $\frac{\partial V^2(r,z)}{\partial z^2}$ is from below:

$$V(r,z+dz_2) = V(r,z) + V'(r,z)dz_2 + \frac{\frac{\partial V^2(r,z)}{\partial z^2}}{2!} dz_2{}^2 + \cdots \quad ③$$

$$V(r,z-dz_1) = V(r,z) - V'(r,z)dz_1 + \frac{\frac{\partial V^2(r,z)}{\partial z^2}}{2!} dz_1{}^2 + \cdots \quad ④$$

③+④

$$\Longrightarrow V(r,z+dz_2) + V(r,z-dz_1) - 2V(r,z) - (dz_2 - dz_1)V'(r,z) = \frac{1}{2}\frac{\partial V^2(r,z)}{\partial z^2}\left(dz_1{}^2 + dz_2{}^2\right)$$

$$\Longrightarrow \frac{\partial V^2(r,z)}{\partial z^2} = \frac{2}{dz_1{}^2 + dz_2{}^2}[V(r,z+dz_2) + V(r,z-dz_1) - 2V(r,z) - (dz_2 - dz_1)V'(r,z)]$$

Moreover, $\frac{\partial V(r,z)}{\partial z} = \frac{V(r,z+dz_2) - V(r,z-dz_1)}{dz_1+dz_2}$

$$\Rightarrow \frac{\partial V^2(r,z)}{\partial z^2} = \frac{2}{{dz_1}^2 + {dz_2}^2}\left[\begin{matrix} V(r,z+dz_2) + V(r,z-dz_1) - 2V(r,z) \\ -(dz_2 - dz_1)\frac{V(r,z+dz_2) - V(r,z-dz_1)}{dz_1 + dz_2}\end{matrix}\right]$$

In Eq.29, the Laplace's equation is $\frac{\partial V^2(r,z)}{\partial r^2} + \frac{1}{r}\frac{\partial V(r,z)}{\partial r} + \frac{\partial V^2(r,z)}{\partial z^2} = 0.$

The previous derivation are used to Eq.29 and the finite difference form is became:

$$\Rightarrow \frac{2}{{dr_1}^2 + {dr_2}^2}\left[\begin{matrix} V(r+dr_2,z) + V(r-dr_1,z) - 2V(r,z) \\ -(dr_2 - dr_1)\frac{V(r+dr_2,z) - V(r-dr_1,z)}{dr_1 + dr_2}\end{matrix}\right]$$

$$+\frac{1}{r}\frac{V(r+dr_2,z) - V(r-dr_1,z)}{dr_1 + dr_2}$$

$$+\frac{2}{{dz_1}^2 + {dz_2}^2}\left[\begin{matrix} V(r,z+dz_2) + V(r,z-dz_1) - 2V(r,z) \\ -(dz_2 - dz_1)\frac{V(r,z+dz_2) - V(r,z-dz_1)}{dz_1 + dz_2}\end{matrix}\right] = 0$$

$$\Rightarrow -V(r,z)\left[\frac{4}{{dr_1}^2 + {dr_2}^2} + \frac{4}{{dz_1}^2 + {dz_2}^2}\right]$$

$$+\frac{2}{{dr_1}^2 + {dr_2}^2}\left[\begin{matrix} V(r+dr_2,z) + V(r-dr_1,z) \\ -(dr_2 - dr_1)\frac{V(r+dr_2,z) - V(r-dr_1,z)}{dr_1 + dr_2}\end{matrix}\right]$$

$$+\frac{2}{{dz_1}^2 + {dz_2}^2}\left[\begin{matrix} V(r,z+dz_2) + V(r,z-dz_1) \\ -(dz_2 - dz_1)\frac{V(r,z+dz_2) - V(r,z-dz_1)}{dz_1 + dz_2}\end{matrix}\right]$$

$$+\frac{1}{r}\frac{V(r+dr_2,z) - V(r-dr_1,z)}{dr_1 + dr_2} = 0$$

Here is the finite difference form which the $r \neq 0$.

$$\Longrightarrow V(r,z) = \left[\frac{4}{{dr_1}^2 + {dr_2}^2} + \frac{4}{{dz_1}^2 + {dz_2}^2}\right]^{-1} *$$

$$\left\{ \frac{2}{{dr_1}^2 + {dr_2}^2}\left[\begin{matrix} V(r+dr_2,z) + V(r-dr_1,z) \\ -(dr_2 - dr_1)\dfrac{V(r+dr_2,z) - V(r-dr_1,z)}{dr_1 + dr_2}\end{matrix}\right] \right.$$

$$\left. + \frac{2}{{dz_1}^2 + {dz_2}^2}\left[\begin{matrix} V(r,z+dz_2) + V(r,z-dz_1) \\ -(dz_2 - dz_1)\dfrac{V(r,z+dz_2) - V(r,z-dz_1)}{dz_1 + dz_2}\end{matrix}\right] + \frac{1}{r}\frac{V(r+dr_2,z) - V(r-dr_1,z)}{dr_1 + dr_2} \right\}$$

APPENDIX B

✧ When the r=0, the derivation of finite difference form is below:

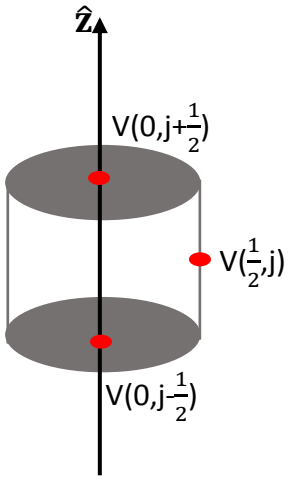

Fig. B-1

Top:

$$\int d\vec{s}\nabla V\Big|_{\frac{dz}{2}} = \frac{\partial V}{\partial z}\Big|_{\frac{dz}{2}} ds = \frac{V(0,j+1)-V(0,j)}{dz}\pi(\frac{dr}{2})^2$$

Bottom:

$$\int d\vec{s}\nabla V\Big|_{\frac{-dz}{2}} = \frac{\partial V}{\partial z}\Big|_{\frac{-dz}{2}} ds = \frac{-(V(0,j)-V(0,j-1))}{dz}\pi(\frac{dr}{2})^2$$

Side:

$$\int d\vec{s}\nabla V\Big|_{\frac{dz}{2}} = \frac{\partial V}{\partial r}\Big|_{\frac{dz}{2}} ds = \frac{V(1,j)-V(0,j)}{dr}2\pi\left(\frac{dr}{2}\right)dz = (V(1,j)-V(0,j))\pi dz$$

Top+Bottom+Side

$$\Rightarrow \text{⑤}\ \frac{V(0,j+1)-V(0,j)}{dz}\pi\left(\frac{dr}{2}\right)^2 - \frac{V(0,j)-V(0,j-1)}{dz}\pi\left(\frac{dr}{2}\right)^2 + \big(V(1,j)-V(0,j)\big)\pi dz$$

$$\Rightarrow V(0,j) = \frac{\frac{dr^2}{4}[V(0,j+1)+V(0,j-1)] + dz^2[V(1,j)-V(0,j)]}{\frac{dr^2}{2}+dz^2}$$

In Eq.⑤, if the dz_2 not equal dz_1, the dz have to divide into dz_1 and dz_2.

$$\Rightarrow \frac{V(0,j+1)-V(0,j)}{dz_2}\pi\left(\frac{dr_2}{2}\right)^2 - \frac{V(0,j)-V(0,j-1)}{dz_1}\pi\left(\frac{dr_2}{2}\right)^2$$

$$+\big(V(1,j)-V(0,j)\big)\pi(\frac{dz_2+dz_1}{2}) = 0$$

$$\Rightarrow dz_1(dr_2)^2\big(V(0,j+1)-V(0,j)\big) - dz_2(dr_2)^2\big(V(0,j)-V(0,j-1)\big)$$

$$+[2dz_1dz_2(dz_1+dz_2)(V(1,j)-V(0,j))] = 0$$

$$\Rightarrow (dr_2)^2[dz_1V(0,j+1)+dz_2V(0,j-1)] + 2dz_1dz_2(dz_1+dz_2)V(1,j)$$

$$= V(0,j)[dz_1(dr_2)^2 + dz_2(dr_2)^2 + 2dz_1dz_2(dz_1+dz_2)]$$

$$\Longrightarrow V(0,j) = \frac{(dr_2)^2[dz_1 V(0,j+1) + dz_2 V(0,j-1)] + 2dz_1 dz_2 (dz_1 + dz_2) V(1,j)}{dz_1 (dr_2)^2 + dz_2 (dr_2)^2 + 2dz_1 dz_2 (dz_1 + dz_2)}$$

APPENDIX C

一階泰勒展開: $f(x+u, y+v) = f(x_i, y_i) + u \cdot \frac{\partial f}{\partial x} + v \cdot \frac{\partial f}{\partial y}$

二階泰勒展開: $f(x+u, y+v) = f(x_i, y_i) + (u \cdot \frac{\partial f}{\partial x} + v \cdot \frac{\partial f}{\partial y}) + \frac{1}{2!}(u^2 \cdot \frac{\partial^2 f}{\partial x^2} + 2uv \cdot \frac{\partial^2 f}{\partial x \partial y} + v^2 \cdot \frac{\partial^2 \partial}{\partial y^2})$

$$k_1 = f(x_i, y_i)$$

$$k_2 = f(x_i + p_1 h,\ y_i + q_{11} k_1 h)$$

$$= f(x_i, y_i) + \left[p_1 h \frac{\partial f}{\partial x} + (q_{11} k_1 h) \frac{\partial f}{\partial y}\right] + \frac{1}{2!}\left[(p_1 h)^2 \frac{\partial^2 f}{\partial x^2} + 2(p_1 h) * (q_{11} k_1 h) \frac{\partial^2 f}{\partial x \partial y} + (q_{11} k_1 h)^2 \frac{\partial^2 f}{\partial y^2}\right]$$

$$k_3 = f(x_i + p_2 h,\ y_i + q_{21} k_1 h + q_{22} k_2 h)$$

$$= f(x_i, y_i) + \left[p_2 h \frac{\partial f}{\partial x} + (q_{21} k_1 h + q_{22} k_2 h) \frac{\partial f}{\partial y}\right] + \frac{1}{2!}\left[{p_2}^2 h^2 \frac{\partial^2 f}{\partial x^2} + 2(q_{21} k_1 h + q_{22} k_2 h) p_2 h \frac{\partial^2 f}{\partial x \partial y} + (q_{21} k_1 h + q_{22} k_2 h)^2 \frac{\partial^2 f}{\partial y^2}\right]$$

$$y_{i+1} = y_i + (a_1 k_1 + a_2 k_2 + a_3 k_3 + \cdots + a_n k_n) \cdot h$$

the Second order Runge-Kutta Methods

$$y_{i+1} = y_i + (a_1 k_1 + a_2 k_2) \cdot h$$

$$\Longrightarrow y_i + a_1 k_1 h + a_2 h\left[f(x_i, y_i) + p_1 h \frac{\partial f}{\partial x} + q_{11} k_1 h \frac{\partial f}{\partial y}\right]$$

$$\Longrightarrow y_i + (a_1 + a_2) f(x_i, y_i) h + (a_2 p_1 \frac{\partial f}{\partial x} + a_2 q_{11} k_1 \frac{\partial f}{\partial y}) h^2$$

$$y_{i+1} = y_i + (a_1 k_1 + a_2 k_2 + a_3 k_3) \cdot h$$

$$\Longrightarrow y_i + a_1 k_1 h + a_2 h\left[f(x_i, y_i) + \left[p_1 h \frac{\partial f}{\partial x} + (q_{11} k_1 h) \frac{\partial f}{\partial y}\right] + \frac{1}{2!}\left[(p_1 h)^2 \frac{\partial^2 f}{\partial x^2} + 2(p_1 h) *\right.\right.$$

$$(q_{11}k_1h)\frac{\partial^2 f}{\partial x\,\partial y}+(q_{11}k_1h)^2\frac{\partial^2 f}{\partial y^2}\Big]+a_3h\Big[f(x_i,y_i)+\Big[p_2h\frac{\partial f}{\partial x}+(q_{21}k_1h+q_{22}k_2h)\frac{\partial f}{\partial y}\Big]+\frac{1}{2!}\Big[{p_2}^2h^2\frac{\partial^2 f}{\partial x^2}+2(p_2h)(q_{21}k_1h+q_{22}k_2h)\frac{\partial^2 f}{\partial x\,\partial y}+(q_{21}k_1h+q_{22}k_2h)^2\frac{\partial^2 f}{\partial y^2}\Big]\Big]$$ **(Eq.2)**

針對這k_3項展開: $\mathbf{f(x_i,y_i)+\Big[p_2h\frac{\partial f}{\partial x}+(q_{21}k_1h+q_{22}k_2h)\frac{\partial f}{\partial y}\Big]+\frac{1}{2!}\Big[{p_2}^2h^2\frac{\partial^2 f}{\partial x^2}+2(p_2h)(q_{21}k_1h+q_{22}k_2h)\frac{\partial^2 f}{\partial x\partial y}+(q_{21}k_1h+q_{22}k_2h)^2\frac{\partial^2 f}{\partial y^2}\Big]}$，並對紅色字體項去整理。

$$\Rightarrow {p_2}^2h^2\frac{\partial^2 f}{\partial x^2}+2(p_2h)(q_{21}k_1h+q_{22}k_2h)\frac{\partial^2 f}{\partial x\,\partial y}+(q_{21}k_1h+q_{22}k_2h)^2\frac{\partial^2 f}{\partial y^2}$$

$$\Rightarrow {p_2}^2h^2\frac{\partial^2 f}{\partial x^2}+2(p_2h)(q_{21}k_1h+q_{22}k_2h)\frac{\partial^2 f}{\partial x\,\partial y}+[(q_{21}k_1h)^2+2q_{21}k_1q_{22}k_2h^2+(q_{22}k_2h)^2]\frac{\partial^2 f}{\partial y^2}$$

$$\Rightarrow {p_2}^2h^2\frac{\partial^2 f}{\partial x^2}+2p_2q_{21}k_1h^2\frac{\partial^2 f}{\partial x\,\partial y}+2p_2q_{21}k_2h^2\frac{\partial^2 f}{\partial x\,\partial y}+[(q_{21}k_1h)^2+2q_{21}k_1q_{22}k_2h^2+(q_{22}k_2h)^2]\frac{\partial^2 f}{\partial y^2}$$

$$\Rightarrow {p_2}^2h^2\frac{\partial^2 f}{\partial x^2}+2p_2q_{21}k_1h^2\frac{\partial^2 f}{\partial x\,\partial y}+2p_2q_{21}\Big\{f(x_i,y_i)+\Big[p_1h\frac{\partial f}{\partial x}+(q_{11}k_1h)\frac{\partial f}{\partial y}\Big]+\frac{1}{2!}\Big[(p_1h)^2\frac{\partial^2 f}{\partial x^2}+2(p_1h)*(q_{11}k_1h)\frac{\partial^2 f}{\partial x\,\partial y}+(q_{11}k_1h)^2\frac{\partial^2 f}{\partial y^2}\Big]\Big\}h^2\frac{\partial^2 f}{\partial x\,\partial y}+[(q_{21}k_1h)^2+2q_{21}k_1q_{22}k_2h^2+(q_{22}k_2h)^2]\frac{\partial^2 f}{\partial y^2}$$

$$\Rightarrow h^2\Big({p_2}^2\frac{\partial^2 f}{\partial x^2}+2p_2q_{21}k_1\frac{\partial^2 f}{\partial x\,\partial y}+2p_2q_{22}k_1\frac{\partial^2 f}{\partial x\,\partial y}\Big)+h^3\Big[\Big(2p_2q_{21}\frac{\partial^2 f}{\partial x\,\partial y}\Big)*\Big(p_1\frac{\partial f}{\partial x}+q_{11}k_1\frac{\partial f}{\partial y}\Big)\Big]+h^4\Big[\Big(p_2q_{21}\frac{\partial^2 f}{\partial x\,\partial y}\Big)*\Big({p_1}^2\frac{\partial^2 f}{\partial x^2}+2p_1q_{11}k_1\frac{\partial^2 f}{\partial x\,\partial y}+(q_{11}k_1)^2\frac{\partial^2 f}{\partial y^2}\Big)\Big]+[(q_{21}k_1h)^2+2q_{21}k_1q_{22}k_2h^2+(q_{22}k_2h)^2]\frac{\partial^2 f}{\partial y^2}$$

$$\Rightarrow h^2\Big({p_2}^2\frac{\partial^2 f}{\partial x^2}+2p_2q_{21}k_1\frac{\partial^2 f}{\partial x\,\partial y}+2p_2q_{22}k_1\frac{\partial^2 f}{\partial x\,\partial y}\Big)+h^3\Big[\Big(2p_2q_{21}\frac{\partial^2 f}{\partial x\,\partial y}\Big)*$$

$$\left(p_1\frac{\partial f}{\partial x}+q_{11}k_1\frac{\partial f}{\partial y}\right)\Big]+h^4\left[\left(p_2q_{21}\frac{\partial^2 f}{\partial x\,\partial y}\right)*\left({p_1}^2\frac{\partial^2 f}{\partial x^2}+2p_1q_{11}k_1\frac{\partial^2 f}{\partial x\,\partial y}+(q_{11}k_1)^2\frac{\partial^2 f}{\partial y^2}\right)\right]+$$

$$\left[(q_{21}k_1h)^2+2q_{21}k_1q_{22}h^2\left\{f(x_i,y_i)+\left[p_1h\frac{\partial f}{\partial x}+(q_{11}k_1h)\frac{\partial f}{\partial y}\right]+\frac{1}{2!}\left[(p_1h)^2\frac{\partial^2 f}{\partial x^2}+\right.\right.\right.$$

$$\left.\left.\left.2(p_1h)*(q_{11}k_1h)\frac{\partial^2 f}{\partial x\,\partial y}+(q_{11}k_1h)^2\frac{\partial^2 f}{\partial y^2}\right]\right\}+(q_{22}k_2h)^2\right]\frac{\partial^2 f}{\partial y^2}$$

$$\Longrightarrow h^2\left({p_2}^2\frac{\partial^2 f}{\partial x^2}+2p_2q_{21}k_1\frac{\partial^2 f}{\partial x\,\partial y}+2p_2q_{22}k_1\frac{\partial^2 f}{\partial x\,\partial y}\right)+h^3\left[\left(2p_2q_{21}\frac{\partial^2 f}{\partial x\,\partial y}\right)*\right.$$

$$\left.\left(p_1\frac{\partial f}{\partial x}+q_{11}k_1\frac{\partial f}{\partial y}\right)\right]+h^4\left[\left(p_2q_{21}\frac{\partial^2 f}{\partial x\,\partial y}\right)*\left({p^2}_1\frac{\partial^2 f}{\partial x^2}+2p_1q_{11}k_1\frac{\partial^2 f}{\partial x\,\partial y}+(q_{11}k_1)^2\frac{\partial^2 f}{\partial y^2}\right)\right]+$$

$$\mathbf{h^2\left[(q_{21}k_1)^2\frac{\partial^2 f}{\partial y^2}+2q_{21}k_1q_{22}*f(x_i,y_i)\frac{\partial^2 f}{\partial y^2}\right]+h^3\left[(2q_{21}k_1q_{22})*\left(p_1\frac{\partial f}{\partial x}+\right.\right.}$$

$$\mathbf{\left.\left.(q_{11}k_1)\frac{\partial f}{\partial y}\right)*\frac{\partial^2 f}{\partial y^2}\right]+h^4\left[(q_{21}k_1q_{22})*\left({p_1}^2\frac{\partial^2 f}{\partial x^2}+2p_1q_{11}k_1\frac{\partial^2 f}{\partial x\partial y}+\ (q_{11}k_1)^2\frac{\partial^2 f}{\partial y^2}\right)*\right.}$$

$$\mathbf{\left.\frac{\partial^2 f}{\partial y^2}\right]}+(q_{22}k_2h)^2\frac{\partial^2 f}{\partial y^2}$$

$$\Longrightarrow h^2\left({p_2}^2\frac{\partial^2 f}{\partial x^2}+2p_2k_1\frac{\partial^2 f}{\partial x\,\partial y}(q_{21}+q_{22})+(q_{21}k_1)^2\frac{\partial^2 f}{\partial y^2}+2q_{21}q_{22}{k_1}^2\frac{\partial^2 f}{\partial y^2}\right)+$$

$$h^3\left[\left(p_1\frac{\partial f}{\partial x}+q_{11}k_1\frac{\partial f}{\partial y}\right)*\left(2p_2q_{22}\frac{\partial^2 f}{\partial x\,\partial y}+2q_{21}k_1q_{21}\frac{\partial^2 f}{\partial y^2}\right)\right]$$

$$h^4\left[\left({p_1}^2\frac{\partial^2 f}{\partial x^2}+2p_1q_{11}k_1\frac{\partial^2 f}{\partial x\,\partial y}+\ (q_{11}k_1)^2\frac{\partial^2 f}{\partial y^2}\right)*\left(p_2q_{21}\frac{\partial^2 f}{\partial x\,\partial y}+q_{21}k_1q_{22}\frac{\partial^2 f}{\partial y^2}\right)\right]$$

$$+(q_{22}k_2h)^2\frac{\partial^2 f}{\partial y^2}$$

其中$(q_{22}k_2h)^2\frac{\partial^2 f}{\partial y^2}$**等於**

$$\Longrightarrow (q_{22}h)^2\frac{\partial^2 f}{\partial y^2}\cdot\left\{f(x_i,y_i)+\left[p_1h\frac{\partial f}{\partial x}+(q_{11}k_1h)\frac{\partial f}{\partial y}\right]+\frac{1}{2!}\left[(p_1h)^2\frac{\partial^2 f}{\partial x^2}+\ 2(p_1h)*\right.\right.$$

$$\left.\left.(q_{11}k_1h)\frac{\partial^2 f}{\partial x\,\partial y}+(q_{11}k_1h)^2\frac{\partial^2 f}{\partial y^2}\right]\right\}\cdot\left\{f(x_i,y_i)+\left[p_1h\frac{\partial f}{\partial x}+(q_{11}k_1h)\frac{\partial f}{\partial y}\right]+\frac{1}{2!}\left[(p_1h)^2\frac{\partial^2 f}{\partial x^2}+\right.\right.$$

$$\left.\left.2(p_1h)*(q_{11}k_1h)\frac{\partial^2 f}{\partial x\,\partial y}+(q_{11}k_1h)^2\frac{\partial^2 f}{\partial y^2}\right]\right\}$$

$$\Longrightarrow h^2\left\{({q_{22}}^2\frac{\partial^2 f}{\partial y^2}){k_1}^2\right\}+h^4\left\{\begin{array}{c}({q_{22}}^2\frac{\partial^2 f}{\partial y^2})\left(p_1\frac{\partial f}{\partial x}\right)^2+({q_{22}}^2\frac{\partial^2 f}{\partial y^2})2p_1q_{11}k_1\left(\frac{\partial f}{\partial x}\right)\left(\frac{\partial f}{\partial y}\right)\\+({q_{22}}^2\frac{\partial^2 f}{\partial y^2})\left(q_{11}k_1\frac{\partial f}{\partial y}\right)^2\end{array}\right\}$$

$$+h^6\left[(q_{22}{}^2\frac{\partial^2 f}{\partial y^2})\right]\left\{\begin{array}{c}\frac{1}{4}p_1{}^4\left(\frac{\partial^2 f}{\partial x^2}\right)^2+(p_1q_{11}k_1)^2\left(\frac{\partial^2 f}{\partial x\,\partial y}\right)^2+\frac{1}{4}(q_{11}k_1)^4\left(\frac{\partial^2 f}{\partial y^2}\right)^2\\ +p_1{}^3q_{11}k_1\frac{\partial^2 f}{\partial x^2}\frac{\partial^2 f}{\partial x\,\partial y}+p_1(q_{11}k_1)^3\frac{\partial^2 f}{\partial x\,\partial y}\left(\frac{\partial^2 f}{\partial y^2}\right)^2+\frac{1}{2}(p_1q_{11}k_1)^2\frac{\partial^2 f}{\partial x^2}\frac{\partial^2 f}{\partial y^2}\end{array}\right\}$$

$$+h^3\left\{2k_1\left[p_1\frac{\partial f}{\partial x}+(q_{11}k_1)\frac{\partial f}{\partial y}\right]q_{22}{}^2\frac{\partial^2 f}{\partial y^2}\right\}$$

$$+h^5\left\{\begin{array}{c}p_1{}^3\frac{\partial^2 f}{\partial x^2}\frac{\partial f}{\partial x}+2p_1{}^2q_{11}k_1\frac{\partial^2 f}{\partial x\,\partial y}\frac{\partial f}{\partial x}+p_1(q_{11}k_1)^2\frac{\partial^2 f}{\partial y^2}\frac{\partial f}{\partial y}+p_1{}^2q_{11}k_1\frac{\partial f}{\partial y}\frac{\partial^2 f}{\partial x^2}\\ +4p_1(q_{11}k_1)^2\frac{\partial^2 f}{\partial x\,\partial y}\frac{\partial f}{\partial y}+(q_{11}k_1)^3\frac{\partial^2 f}{\partial y^2}\frac{\partial f}{\partial y}\end{array}\right\}q_{22}{}^2\frac{\partial^2 f}{\partial y^2}$$

$$+h^4\left\{p_1{}^2\frac{\partial^2 f}{\partial x^2}+\ 2p_1q_{11}k_1\frac{\partial^2 f}{\partial x\,\partial y}+q_{11}{}^2k_1{}^3\frac{\partial^2 f}{\partial y^2}\right\}q_{22}{}^2\frac{\partial^2 f}{\partial y^2}$$

則整理後等於:

$$\Longrightarrow h^2\left(p_2{}^2\frac{\partial^2 f}{\partial x^2}+2p_2k_1\frac{\partial^2 f}{\partial x\,\partial y}(q_{21}+q_{22})+[(q_{21}k_1)^2+(k_1q_{22})^2]\frac{\partial^2 f}{\partial y^2}+\right.$$

$$\left.2q_{21}q_{22}k_1{}^2\frac{\partial^2 f}{\partial y^2}\right)$$

$$+h^3\left[\left(p_1\frac{\partial f}{\partial x}+q_{11}k_1\frac{\partial f}{\partial y}\right)*(2p_2q_{22}\frac{\partial^2 f}{\partial x\,\partial y}+2q_{21}k_1q_{21}\frac{\partial^2 f}{\partial y^2}+2k_1q_{22}{}^2\frac{\partial^2 f}{\partial y^2})\right]$$

$$+h^4\left[\begin{array}{c}\left(p_1{}^2\frac{\partial^2 f}{\partial x^2}+2p_1q_{11}k_1\frac{\partial^2 f}{\partial x\,\partial y}+\ (q_{11}k_1)^2\frac{\partial^2 f}{\partial y^2}\right)*\left(p_2q_{21}\frac{\partial^2 f}{\partial x\,\partial y}+q_{21}k_1q_{22}\frac{\partial^2 f}{\partial y^2}\right)\\ +(q_{22}{}^2\frac{\partial^2 f}{\partial y^2})\left(p_1\frac{\partial f}{\partial x}\right)^2+(q_{22}{}^2\frac{\partial^2 f}{\partial y^2})2p_1q_{11}k_1\left(\frac{\partial f}{\partial x}\right)\left(\frac{\partial f}{\partial y}\right)+(q_{22}{}^2\frac{\partial^2 f}{\partial y^2})\left(q_{11}k_1\frac{\partial f}{\partial y}\right)^2\\ +p_1{}^2q_{22}{}^2\frac{\partial^2 f}{\partial x^2}\frac{\partial^2 f}{\partial y^2}+2p_1q_{11}k_1q_{22}{}^2\frac{\partial^2 f}{\partial x\,\partial y}\frac{\partial^2 f}{\partial y^2}+q_{11}{}^2k_1{}^3q_{22}{}^2\frac{\partial^2 f}{\partial y^2}\frac{\partial^2 f}{\partial y^2}\end{array}\right]$$

$$+h^5\left[\begin{array}{c}p_1{}^3\frac{\partial^2 f}{\partial x^2}\frac{\partial f}{\partial x}+2p_1{}^2q_{11}k_1\frac{\partial^2 f}{\partial x\,\partial y}\frac{\partial f}{\partial x}+p_1(q_{11}k_1)^2\frac{\partial^2 f}{\partial y^2}\frac{\partial f}{\partial y}+p_1{}^2q_{11}k_1\frac{\partial f}{\partial y}\frac{\partial^2 f}{\partial x^2}\\ +4p_1(q_{11}k_1)^2\frac{\partial^2 f}{\partial x\,\partial y}\frac{\partial f}{\partial y}+(q_{11}k_1)^3\frac{\partial^2 f}{\partial y^2}\frac{\partial f}{\partial y}\end{array}\right]q_{22}{}^2\frac{\partial^2 f}{\partial y^2}$$

$$+h^6\left[\begin{array}{c}\frac{1}{4}p_1{}^4\left(\frac{\partial^2 f}{\partial x^2}\right)^2+(p_1q_{11}k_1)^2\left(\frac{\partial^2 f}{\partial x\,\partial y}\right)^2+\frac{1}{4}(q_{11}k_1)^4\left(\frac{\partial^2 f}{\partial y^2}\right)^2+p_1{}^3q_{11}k_1\frac{\partial^2 f}{\partial x^2}\frac{\partial^2 f}{\partial x\,\partial y}\\ +p_1(q_{11}k_1)^3\frac{\partial^2 f}{\partial x\,\partial y}(\frac{\partial^2 f}{\partial y^2})^2+\frac{1}{2}(p_1q_{11}k_1)^2\frac{\partial^2 f}{\partial x^2}\frac{\partial^2 f}{\partial y^2}\end{array}\right](q_{22}{}^2\frac{\partial^2 f}{\partial y^2})$$

$$\Longrightarrow k_3 = f(x_i, y_i) + \left[p_2 h \frac{\partial f}{\partial x} + (q_{21}k_1 h + q_{22}\mathbf{k_2} h)\frac{\partial f}{\partial y}\right] + \frac{\mathbf{1}}{\mathbf{2!}}\left[\mathbf{p_2{}^2 h^2 \frac{\partial^2 f}{\partial x^2}} + \right.$$

$$\left.\mathbf{2(p_2 h)(q_{21}k_1 h + q_{22}k_2 h)\frac{\partial^2 f}{\partial x \partial y}} + \mathbf{(q_{21}k_1 h + q_{22}k_2 h)^2 \frac{\partial^2 f}{\partial y^2}}\right]$$

$\Longrightarrow k_3$ 等於

$$f(x_i, y_i)$$

$$+\left[p_2 h \frac{\partial f}{\partial x}\right.$$

$$+\left(+q_{22}\left\{f(x_i, y_i) + \left[p_1 h \frac{\partial f}{\partial x} + (q_{11}k_1 h)\frac{\partial f}{\partial y}\right] + \frac{1}{2!}\left[(p_1 h)^2 \frac{\partial^2 f}{\partial x^2} + 2(p_1 h) * (q_{11}k_1 h)\frac{\partial^2 f}{\partial x \partial y}\right.\right.\right.$$

$$\left.\left.\left. + (q_{11}k_1 h)^2 \frac{\partial^2 f}{\partial y^2}\right]\right\} h\right)\left.\frac{\partial f}{\partial y}\right]$$

$$+h^2\left(\frac{1}{2}p_2{}^2 \frac{\partial^2 f}{\partial x^2} + p_2 k_1 \frac{\partial^2 f}{\partial x \partial y}(q_{21} + q_{22}) + \frac{1}{2}[(q_{21}k_1)^2 + (k_1 q_{22})^2]\frac{\partial^2 f}{\partial y^2}\right.$$

$$\left. + q_{21}q_{22}k_1{}^2 \frac{\partial^2 f}{\partial y^2}\right)$$

$$+h^3\left[\left(p_1 \frac{\partial f}{\partial x} + q_{11}k_1 \frac{\partial f}{\partial y}\right) * (p_2 q_{22}\frac{\partial^2 f}{\partial x \partial y} + q_{21}k_1 q_{21}\frac{\partial^2 f}{\partial y^2} + k_1 q_{22}{}^2 \frac{\partial^2 f}{\partial y^2})\right]$$

$$+h^4\left[\frac{1}{2}\left(p_1{}^2 \frac{\partial^2 f}{\partial x^2} + 2p_1 q_{11}k_1 \frac{\partial^2 f}{\partial x \partial y} + (q_{11}k_1)^2 \frac{\partial^2 f}{\partial y^2}\right) * \left(p_2 q_{21}\frac{\partial^2 f}{\partial x \partial y} + \right.\right.$$

$$\left.\left. q_{21}k_1 q_{22}\frac{\partial^2 f}{\partial y^2}\right) + \frac{1}{2}(q_{22}{}^2 \frac{\partial^2 f}{\partial y^2})\left(p_1 \frac{\partial f}{\partial x}\right)^2 + (q_{22}{}^2 \frac{\partial^2 f}{\partial y^2})p_1 q_{11}k_1 \left(\frac{\partial f}{\partial x}\right)\left(\frac{\partial f}{\partial y}\right) + \right.$$

$$\frac{1}{2}(q_{22}{}^2 \frac{\partial^2 f}{\partial y^2})\left(q_{11}k_1 \frac{\partial f}{\partial y}\right)^2 + \frac{1}{2}p_1{}^2 q_{22}{}^2 \frac{\partial^2 f}{\partial x^2}\frac{\partial^2 f}{\partial y^2} + p_1 q_{11}k_1 q_{22}{}^2 \frac{\partial^2 f}{\partial x \partial y}\frac{\partial^2 f}{\partial y^2} + $$

$$\left.\frac{1}{2}q_{11}{}^2 k_1{}^3 q_{22}{}^2 \frac{\partial^2 f}{\partial y^2}\frac{\partial^2 f}{\partial y^2}\right]$$

$$+h^5\left[\begin{array}{l}\frac{1}{2}p_1{}^3 \frac{\partial^2 f}{\partial x^2}\frac{\partial f}{\partial x} + p_1{}^2 q_{11}k_1 \frac{\partial^2 f}{\partial x \partial y}\frac{\partial f}{\partial x} + \frac{1}{2}p_1(q_{11}k_1)^2 \frac{\partial^2 f}{\partial y^2}\frac{\partial f}{\partial y} \\ + \frac{1}{2}p_1{}^2 q_{11}k_1 \frac{\partial f}{\partial y}\frac{\partial^2 f}{\partial x^2} + 2p_1(q_{11}k_1)^2 \frac{\partial^2 f}{\partial x \partial y}\frac{\partial f}{\partial y} + \frac{1}{2}(q_{11}k_1)^3 \frac{\partial^2 f}{\partial y^2}\frac{\partial f}{\partial y}\end{array}\right] q_{22}{}^2 \frac{\partial^2 f}{\partial y^2}$$

$$+h^6\begin{bmatrix}\frac{1}{8}p_1{}^4\left(\frac{\partial^2 f}{\partial x^2}\right)^2+\frac{1}{2}(p_1q_{11}k_1)^2\left(\frac{\partial^2 f}{\partial x\,\partial y}\right)^2+\frac{1}{8}(q_{11}k_1)^4\left(\frac{\partial^2 f}{\partial y^2}\right)^2\\ +\frac{1}{2}p_1{}^3q_{11}k_1\frac{\partial^2 f}{\partial x^2}\frac{\partial^2 f}{\partial x\,\partial y}+\frac{1}{2}p_1(q_{11}k_1)^3\frac{\partial^2 f}{\partial x\,\partial y}\left(\frac{\partial^2 f}{\partial y^2}\right)^2+\frac{1}{4}(p_1q_{11}k_1)^2\frac{\partial^2 f}{\partial x^2}\frac{\partial^2 f}{\partial y^2}\end{bmatrix}\left(q_{22}{}^2\frac{\partial^2 f}{\partial y^2}\right)$$

$$\Longrightarrow f(x_i,y_i)+h\left[p_2\frac{\partial f}{\partial x}+q_{21}k_1\frac{\partial f}{\partial y}+q_{22}k_1\frac{\partial f}{\partial y}\right]+h^2\left[\left(q_{22}\frac{\partial f}{\partial y}\right)*p_1\frac{\partial f}{\partial x}+\left(q_{22}\frac{\partial f}{\partial y}\right)*\right.$$

$$\left.\left(q_{11}k_1\frac{\partial f}{\partial y}\right)\right]+h^3\left[\frac{1}{2}\left(q_{22}\frac{\partial f}{\partial y}\right)*p_1{}^2\frac{\partial^2 f}{\partial x^2}+\left(q_{22}\frac{\partial f}{\partial y}\right)*\left(p_1q_{11}k_1\right)\frac{\partial^2 f}{\partial x\partial y}+\frac{1}{2}\left(q_{22}\frac{\partial f}{\partial y}\right)*(q_{11}k_1)^2\frac{\partial^2 f}{\partial y^2}\right]$$

$$+h^2\left(\frac{1}{2}p_2{}^2\frac{\partial^2 f}{\partial x^2}+p_2k_1\frac{\partial^2 f}{\partial x\partial y}(q_{21}+q_{22})+\frac{1}{2}[(q_{21}k_1)^2+(k_1q_{22})^2]\frac{\partial^2 f}{\partial y^2}\right.$$

$$\left.+q_{21}q_{22}k_1{}^2\frac{\partial^2 f}{\partial y^2}\right)$$

$$+h^3\left[\left(p_1\frac{\partial f}{\partial x}+q_{11}k_1\frac{\partial f}{\partial y}\right)*\left(p_2q_{22}\frac{\partial^2 f}{\partial x\partial y}+q_{21}k_1q_{21}\frac{\partial^2 f}{\partial y^2}+k_1q_{22}{}^2\frac{\partial^2 f}{\partial y^2}\right)\right]$$

$$+h^4\begin{bmatrix}\frac{1}{2}\left(p_1{}^2\frac{\partial^2 f}{\partial x^2}+2p_1q_{11}k_1\frac{\partial^2 f}{\partial x\partial y}+(q_{11}k_1)^2\frac{\partial^2 f}{\partial y^2}\right)*\left(p_2q_{21}\frac{\partial^2 f}{\partial x\partial y}+q_{21}k_1q_{22}\frac{\partial^2 f}{\partial y^2}\right)\\ +\frac{1}{2}(q_{22}{}^2\frac{\partial^2 f}{\partial y^2})\left(p_1\frac{\partial f}{\partial x}\right)^2+(q_{22}{}^2\frac{\partial^2 f}{\partial y^2})p_1q_{11}k_1\left(\frac{\partial f}{\partial x}\right)\left(\frac{\partial f}{\partial y}\right)\\ +\frac{1}{2}(q_{22}{}^2\frac{\partial^2 f}{\partial y^2})\left(q_{11}k_1\frac{\partial f}{\partial y}\right)^2+\frac{1}{2}p_1{}^2q_{22}{}^2\frac{\partial^2 f}{\partial x^2}\frac{\partial^2 f}{\partial y^2}+p_1q_{11}k_1q_{22}{}^2\frac{\partial^2 f}{\partial x\partial y}\frac{\partial^2 f}{\partial y^2}+\frac{1}{2}q_{11}{}^2k_1{}^3q_{22}{}^2\frac{\partial^2 f}{\partial y^2}\frac{\partial^2 f}{\partial y^2}\end{bmatrix}$$

$$+h^5\begin{bmatrix}\frac{1}{2}p_1{}^3\frac{\partial^2 f}{\partial x^2}\frac{\partial f}{\partial x}+p_1{}^2q_{11}k_1\frac{\partial^2 f}{\partial x\partial y}\frac{\partial f}{\partial x}+\frac{1}{2}p_1(q_{11}k_1)^2\frac{\partial^2 f}{\partial y^2}\frac{\partial f}{\partial y}\\ +\frac{1}{2}p_1{}^2q_{11}k_1\frac{\partial f}{\partial y}\frac{\partial^2 f}{\partial x^2}+2p_1(q_{11}k_1)^2\frac{\partial^2 f}{\partial x\partial y}\frac{\partial f}{\partial y}+\frac{1}{2}(q_{11}k_1)^3\frac{\partial^2 f}{\partial y^2}\frac{\partial f}{\partial y}\end{bmatrix}q_{22}{}^2\frac{\partial^2 f}{\partial y^2}$$

$$+h^6\begin{bmatrix}\frac{1}{8}p_1{}^4\left(\frac{\partial^2 f}{\partial x^2}\right)^2+\frac{1}{2}(p_1q_{11}k_1)^2\left(\frac{\partial^2 f}{\partial x\partial y}\right)^2+\frac{1}{8}(q_{11}k_1)^4\left(\frac{\partial^2 f}{\partial y^2}\right)^2\\ +\frac{1}{2}p_1{}^3q_{11}k_1\frac{\partial^2 f}{\partial x^2}\frac{\partial^2 f}{\partial x\partial y}+\frac{1}{2}p_1(q_{11}k_1)^3\frac{\partial^2 f}{\partial x\partial y}\left(\frac{\partial^2 f}{\partial y^2}\right)^2+\frac{1}{4}(p_1q_{11}k_1)^2\frac{\partial^2 f}{\partial x^2}\frac{\partial^2 f}{\partial y^2}\end{bmatrix}\left(q_{22}{}^2\frac{\partial^2 f}{\partial y^2}\right)$$

$$\Longrightarrow \boldsymbol{k_3} = f(x_i, y_i) + h\left[p_2\frac{\partial f}{\partial x} + q_{21}k_1\frac{\partial f}{\partial y} + q_{22}k_1\frac{\partial f}{\partial y}\right]$$

$$+h^2\left(\begin{array}{c}\frac{1}{2}{p_2}^2\frac{\partial^2 f}{\partial x^2} + p_2k_1\frac{\partial^2 f}{\partial x\partial y}(q_{21}+q_{22}) \\ +\frac{1}{2}[(q_{21}k_1)^2 + (k_1q_{22})^2]\frac{\partial^2 f}{\partial y^2} + q_{21}q_{22}{k_1}^2\frac{\partial^2 f}{\partial y^2} + (q_{22}\frac{\partial f}{\partial y}) * p_1\frac{\partial f}{\partial x} + (q_{22}\frac{\partial f}{\partial y}) * (q_{11}k_1\frac{\partial f}{\partial y})\end{array}\right)$$

$$+h^3\left[\begin{array}{c}\left(p_1\frac{\partial f}{\partial x} + q_{11}k_1\frac{\partial f}{\partial y}\right) * \left(p_2q_{22}\frac{\partial^2 f}{\partial x\partial y} + q_{21}k_1q_{21}\frac{\partial^2 f}{\partial y^2} + k_1{q_{22}}^2\frac{\partial^2 f}{\partial y^2}\right) \\ +\frac{1}{2}\left(q_{22}\frac{\partial f}{\partial y}\right) * {p_1}^2\frac{\partial^2 f}{\partial x^2} + \left(q_{22}\frac{\partial f}{\partial y}\right) * (p_1q_{11}k_1)\frac{\partial^2 f}{\partial x\partial y} + \frac{1}{2}\left(q_{22}\frac{\partial f}{\partial y}\right)(q_{11}k_1)^2\frac{\partial^2 f}{\partial y^2}\end{array}\right]$$

$$+h^4\left[\begin{array}{c}\frac{1}{2}\left({p_1}^2\frac{\partial^2 f}{\partial x^2} + 2p_1q_{11}k_1\frac{\partial^2 f}{\partial x\partial y} + (q_{11}k_1)^2\frac{\partial^2 f}{\partial y^2}\right) * \left(p_2q_{21}\frac{\partial^2 f}{\partial x\partial y} + q_{21}k_1q_{22}\frac{\partial^2 f}{\partial y^2}\right) \\ +\frac{1}{2}({q_{22}}^2\frac{\partial^2 f}{\partial y^2})\left(p_1\frac{\partial f}{\partial x}\right)^2 + ({q_{22}}^2\frac{\partial^2 f}{\partial y^2})p_1q_{11}k_1\left(\frac{\partial f}{\partial x}\right)\left(\frac{\partial f}{\partial y}\right) + \frac{1}{2}({q_{22}}^2\frac{\partial^2 f}{\partial y^2})\left(q_{11}k_1\frac{\partial f}{\partial y}\right)^2 \\ +\frac{1}{2}{p_1}^2{q_{22}}^2\frac{\partial^2 f}{\partial x^2}\frac{\partial^2 f}{\partial y^2} + p_1q_{11}k_1{q_{22}}^2\frac{\partial^2 f}{\partial x\partial y}\frac{\partial^2 f}{\partial y^2} + \frac{1}{2}{q_{11}}^2{k_1}^3{q_{22}}^2\frac{\partial^2 f}{\partial y^2}\frac{\partial^2 f}{\partial y^2}\end{array}\right]$$

$$+h^5\left[\begin{array}{c}\frac{1}{2}{p_1}^3\frac{\partial^2 f}{\partial x^2}\frac{\partial f}{\partial x} + {p_1}^2q_{11}k_1\frac{\partial^2 f}{\partial x\partial y}\frac{\partial f}{\partial x} + \frac{1}{2}p_1(q_{11}k_1)^2\frac{\partial^2 f}{\partial y^2}\frac{\partial f}{\partial y} \\ +\frac{1}{2}{p_1}^2q_{11}k_1\frac{\partial f}{\partial y}\frac{\partial^2 f}{\partial x^2} + 2p_1(q_{11}k_1)^2\frac{\partial^2 f}{\partial x\partial y}\frac{\partial f}{\partial y} + \frac{1}{2}(q_{11}k_1)^3\frac{\partial^2 f}{\partial^2}\frac{\partial f}{\partial y}\end{array}\right]{q_{22}}^2\frac{\partial^2 f}{\partial y^2}$$

$$+h^6\left[\begin{array}{c}\frac{1}{8}{p_1}^4\left(\frac{\partial^2 f}{\partial x^2}\right)^2 + \frac{1}{2}(p_1q_{11}k_1)^2\left(\frac{\partial^2 f}{\partial x\partial y}\right)^2 + \frac{1}{8}(q_{11}k_1)^4\left(\frac{\partial^2 f}{\partial y^2}\right)^2 \\ +\frac{1}{2}{p_1}^3q_{11}\mathrm{k}_1\frac{\partial^2 f}{\partial x^2}\frac{\partial^2 f}{\partial x\partial y} + \frac{1}{2}p_1(q_{11}k_1)^3\frac{\partial^2 f}{\partial x\partial y}(\frac{\partial^2 f}{\partial y^2})^2 + \frac{1}{4}(p_1q_{11}k_1)^2\frac{\partial^2 f}{\partial x^2}\frac{\partial^2 f}{\partial y^2}\end{array}\right](q_{22}{}^2\frac{\partial^2 f}{\partial y^2})$$

$$\Longrightarrow \text{且}\boldsymbol{k_2} = f(x_i, y_i) + \left[p_1h\frac{\partial f}{\partial x} + (q_{11}k_1h)\frac{\partial f}{\partial y}\right] + \frac{1}{2!}\left[(p_1h)^2\frac{\partial^2 f}{\partial x^2} + 2(p_1h) * (q_{11}k_1h)\frac{\partial^2 f}{\partial x\partial y} + (q_{11}k_1h)^2\frac{\partial^2 f}{\partial y^2}\right]$$

$$\Longrightarrow y_{i+1} = y_i + (a_1k_1 + a_2k_2 + a_3k_3)\cdot h$$

$$\Rightarrow y_{i+1} = y_i + a_1 k_1 h$$

$$+ a_2 h \begin{bmatrix} f(x_i, y_i) + \left[p_1 h \frac{\partial f}{\partial x} + (q_{11} k_1 h) \frac{\partial f}{\partial y}\right] \\ + \frac{1}{2!}\left[(p_1 h)^2 \frac{\partial^2 f}{\partial x^2} + 2(p_1 h) * (q_{11} k_1 h) \frac{\partial^2 f}{\partial x \partial y} + (q_{11} k_1 h)^2 \frac{\partial^2 f}{\partial y^2}\right] \end{bmatrix}$$

$$+ a_3 h \begin{Bmatrix} f(x_i, y_i) + h\left[p_2 \frac{\partial f}{\partial x} + q_{21} k_1 \frac{\partial f}{\partial y} + q_{22} k_1 \frac{\partial f}{\partial y}\right] \\ + h^2 \begin{pmatrix} \frac{1}{2} {p_2}^2 \frac{\partial^2 f}{\partial x^2} + p_2 k_1 \frac{\partial^2 f}{\partial x \partial y}(q_{21} + q_{22}) + \frac{1}{2}\left[(q_{21} k_1)^2 + (k_1 q_{22})^2\right] \frac{\partial^2 f}{\partial y^2} \\ + q_{21} q_{22} {k_1}^2 \frac{\partial^2 f}{\partial y^2} + (q_{22} \frac{\partial f}{\partial y}) * p_1 \frac{\partial f}{\partial x} + (q_{22} \frac{\partial f}{\partial y}) * (q_{11} k_1 \frac{\partial f}{\partial y}) \end{pmatrix} \\ + h^3 \begin{bmatrix} \left(p_1 \frac{\partial f}{\partial x} + q_{11} k_1 \frac{\partial f}{\partial y}\right) * \left(p_2 q_{22} \frac{\partial^2 f}{\partial x \partial y} + q_{21} k_1 q_{21} \frac{\partial^2 f}{\partial y^2} + k_1 {q_{22}}^2 \frac{\partial^2 f}{\partial y^2}\right) \\ + \frac{1}{2}\left(q_{22} \frac{\partial f}{\partial y}\right) * {p_1}^2 \frac{\partial^2 f}{\partial x^2} + \left(q_{22} \frac{\partial f}{\partial y}\right) * (p_1 q_{11} k_1) \frac{\partial^2 f}{\partial x \partial y} + \frac{1}{2}\left(q_{22} \frac{\partial f}{\partial y}\right)(q_{11} k_1)^2 \frac{\partial^2 f}{\partial y^2} \end{bmatrix} \\ + h^4 \begin{bmatrix} \frac{1}{2}\left({p_1}^2 \frac{\partial^2 f}{\partial x^2} + 2 p_1 q_{11} k_1 \frac{\partial^2 f}{\partial x \partial y} + (q_{11} k_1)^2 \frac{\partial^2 f}{\partial y^2}\right) * \left(p_2 q_{21} \frac{\partial^2 f}{\partial x \partial y} + q_{21} k_1 q_{22} \frac{\partial^2 f}{\partial y^2}\right) \\ + \frac{1}{2}({q_{22}}^2 \frac{\partial^2 f}{\partial y^2})\left(p_1 \frac{\partial f}{\partial x}\right)^2 + ({q_{22}}^2 \frac{\partial^2 f}{\partial y^2}) p_1 q_{11} k_1 \left(\frac{\partial f}{\partial x}\right)\left(\frac{\partial f}{\partial y}\right) + \frac{1}{2}({q_{22}}^2 \frac{\partial^2 f}{\partial y^2})\left(q_{11} k_1 \frac{\partial f}{\partial y}\right)^2 \\ + \frac{1}{2} {p_1}^2 {q_{22}}^2 \frac{\partial^2 f}{\partial x^2}\frac{\partial^2 f}{\partial y^2} + p_1 q_{11} k_1 {q_{22}}^2 \frac{\partial^2 f}{\partial x \partial y}\frac{\partial^2 f}{\partial y^2} + \frac{1}{2} {q_{11}}^2 {k_1}^3 {q_{22}}^2 \frac{\partial^2 f}{\partial y^2}\frac{\partial^2 f}{\partial y^2} \end{bmatrix} \\ + h^5 \begin{bmatrix} \frac{1}{2} {p_1}^3 \frac{\partial^2 f}{\partial x^2}\frac{\partial f}{\partial x} + {p_1}^2 q_{11} k_1 \frac{\partial^2 f}{\partial x \partial y}\frac{\partial f}{\partial x} + \frac{1}{2} p_1 (q_{11} k_1)^2 \frac{\partial^2 f}{\partial y^2}\frac{\partial f}{\partial y} \\ + \frac{1}{2} {p_1}^2 q_{11} k_1 \frac{\partial f}{\partial y}\frac{\partial^2 f}{\partial x^2} + 2 p_1 (q_{11} k_1)^2 \frac{\partial^2 f}{\partial x \partial y}\frac{\partial f}{\partial y} + \frac{1}{2}(q_{11} k_1)^3 \frac{\partial^2 f}{\partial y^2}\frac{\partial f}{\partial y} \end{bmatrix} {q_{22}}^2 \frac{\partial^2 f}{\partial y^2} \\ + h^6 \begin{bmatrix} \frac{1}{8} {p_1}^4 \left(\frac{\partial^2 f}{\partial x^2}\right)^2 + \frac{1}{2}(p_1 q_{11} k_1)^2 \left(\frac{\partial^2 f}{\partial x \partial y}\right)^2 + \frac{1}{8}(q_{11} k_1)^4 \left(\frac{\partial^2 f}{\partial y^2}\right)^2 + \frac{1}{2} {p_1}^3 q_{11} k_1 \frac{\partial^2 f}{\partial x^2}\frac{\partial^2 f}{\partial x \partial y} \\ + \frac{1}{2} p_1 (q_{11} k_1)^3 \frac{\partial^2 f}{\partial x \partial y}\left(\frac{\partial^2 f}{\partial y^2}\right)^2 + \frac{1}{4}(p_1 q_{11} k_1)^2 \frac{\partial^2 f}{\partial x^2}\frac{\partial^2 f}{\partial y^2} \end{bmatrix} ({q_{22}}^2 \frac{\partial^2 f}{\partial y^2}) \end{Bmatrix}$$

$$\Longrightarrow y_{i+1} = y_i + (a_1 + a_2 + a_3)k_1\boldsymbol{h}$$

$$+\boldsymbol{h^2}\left\{a_3\left[p_2\frac{\partial f}{\partial x} + q_{21}k_1\frac{\partial f}{\partial y} + q_{22}k_1\frac{\partial f}{\partial y}\right] + a_2\left[p_1\frac{\partial f}{\partial x} + (q_{11}k_1)\frac{\partial f}{\partial y}\right]\right\}$$

$$+\boldsymbol{h^3}\left\{\begin{array}{l} a_3\left(\begin{array}{c}\frac{1}{2}{p_2}^2\frac{\partial^2 f}{\partial x^2} + p_2k_1\frac{\partial^2 f}{\partial x\partial y}(q_{21}+q_{22}) + \frac{1}{2}[(q_{21}k_1)^2 + (k_1q_{22})^2]\frac{\partial^2 f}{\partial y^2} \\ +q_{21}q_{22}{k_1}^2\frac{\partial^2 f}{\partial y^2} + (q_{22}\frac{\partial f}{\partial y}) * p_1\frac{\partial f}{\partial x} + (q_{22}\frac{\partial f}{\partial y}) * (q_{11}k_1\frac{\partial f}{\partial y})\end{array}\right) \\ +\frac{a_2}{2!}\left[(p_1)^2\frac{\partial^2 f}{\partial x^2} + 2(p_1q_{11}k_1)\frac{\partial^2 f}{\partial x\partial y} + (q_{11}k_1)^2\frac{\partial^2 f}{\partial y^2}\right]\end{array}\right\}$$

$$+\boldsymbol{h^4}\left\{a_3\left[\begin{array}{c}\left(p_1\frac{\partial f}{\partial x} + q_{11}k_1\frac{\partial f}{\partial y}\right) * \left(p_2q_{22}\frac{\partial^2 f}{\partial x\partial y} + q_{21}k_1q_{21}\frac{\partial^2 f}{\partial y^2} + k_1{q_{22}}^2\frac{\partial^2 f}{\partial y^2}\right) \\ +\frac{1}{2}\left(q_{22}\frac{\partial f}{\partial y}\right) * {p_1}^2\frac{\partial^2 f}{\partial x^2} + \left(q_{22}\frac{\partial f}{\partial y}\right) * (p_1q_{11}k_1)\frac{\partial^2 f}{\partial x\partial y} + \frac{1}{2}\left(q_{22}\frac{\partial f}{\partial y}\right)(q_{11}k_1)^2\frac{\partial^2 f}{\partial y^2}\end{array}\right]\right\}$$

$$+\boldsymbol{h^5}\left\{a_3\left[\begin{array}{c}\frac{1}{2}\left({p_1}^2\frac{\partial^2 f}{\partial x^2} + 2p_1q_{11}k_1\frac{\partial^2 f}{\partial x\partial y} + (q_{11}k_1)^2\frac{\partial^2 f}{\partial y^2}\right) * \left(p_2q_{21}\frac{\partial^2 f}{\partial x\partial y} + q_{21}k_1q_{22}\frac{\partial^2 f}{\partial y^2}\right) \\ +\frac{1}{2}({q_{22}}^2\frac{\partial^2 f}{\partial y^2})\left(p_1\frac{\partial f}{\partial x}\right)^2 + ({q_{22}}^2\frac{\partial^2 f}{\partial y^2})p_1q_{11}k_1\left(\frac{\partial f}{\partial x}\right)\left(\frac{\partial f}{\partial y}\right) + \frac{1}{2}({q_{22}}^2\frac{\partial^2 f}{\partial y^2})\left(q_{11}k_1\frac{\partial f}{\partial y}\right)^2 \\ +\frac{1}{2}{p_1}^2{q_{22}}^2\frac{\partial^2 f}{\partial x^2}\frac{\partial^2 f}{\partial y^2} + p_1q_{11}k_1{q_{22}}^2\frac{\partial^2 f}{\partial x\partial y}\frac{\partial^2 f}{\partial y^2} + \frac{1}{2}{q_{11}}^2{k_1}^3{q_{22}}^2\frac{\partial^2 f}{\partial y^2}\frac{\partial^2 f}{\partial y^2}\end{array}\right]\right\}$$

$$+\boldsymbol{h^6}\left\{a_3\left[\begin{array}{c}\frac{1}{2}{p_1}^3\frac{\partial^2 f}{\partial x^2}\frac{\partial f}{\partial x} + {p_1}^2q_{11}k_1\frac{\partial^2 f}{\partial x\partial y}\frac{\partial f}{\partial x} + \frac{1}{2}p_1(q_{11}k_1)^2\frac{\partial^2 f}{\partial y^2}\frac{\partial f}{\partial y} + \frac{1}{2}{p_1}^2q_{11}k_1\frac{\partial f}{\partial y}\frac{\partial^2 f}{\partial x^2} \\ +2p_1(q_{11}k_1)^2\frac{\partial^2 f}{\partial x\partial y}\frac{\partial f}{\partial y} + \frac{1}{2}(q_{11}k_1)^3\frac{\partial^2 f}{\partial y^2}\frac{\partial f}{\partial y} \\ {q_{22}}^2\frac{\partial^2 f}{\partial y^2}\end{array}\right]\right\}$$

$$+\boldsymbol{h^7}\left\{a_3\left[\begin{array}{c}\frac{1}{8}{p_1}^4\left(\frac{\partial^2 f}{\partial x^2}\right)^2 + \frac{1}{2}(p_1q_{11}k_1)^2\left(\frac{\partial^2 f}{\partial x\partial y}\right)^2 + \frac{1}{8}(q_{11}k_1)^4\left(\frac{\partial^2 f}{\partial y^2}\right)^2 + \frac{1}{2}{p_1}^3q_{11}k_1\frac{\partial^2 f}{\partial x^2}\frac{\partial^2 f}{\partial x\partial y} \\ +\frac{1}{2}p_1(q_{11}k_1)^3\frac{\partial^2 f}{\partial x\partial y}\left(\frac{\partial^2 f}{\partial y^2}\right)^2 + \frac{1}{4}(p_1q_{11}k_1)^2\frac{\partial^2 f}{\partial x^2}\frac{\partial^2 f}{\partial y^2} \\ ({q_{22}}^2\frac{\partial^2 f}{\partial y^2})\end{array}\right]\right\}$$